WEIGHT MINIMIZATION OF SOUND PACKAGES BY BALANCING ABSORPTION AND TRANSMISSION PERFORMANCE

by

Hyunjun Shin

A Dissertation

Submitted to the Faculty of Purdue University

In Partial Fulfillment of the Requirements for the degree of

Doctor of Philosophy

School of Mechanical Engineering

West Lafayette, Indiana

May 2019

THE PURDUE UNIVERSITY GRADUATE SCHOOL
STATEMENT OF COMMITTEE APPROVAL

Dr. J. Stuart Bolton, Chair
School of Mechanical Engineering
Dr. Charles M. Krousgrill
School of Mechanical Engineering
Dr. Jeffrey F. Rhoads
School of Mechanical Engineering
Dr. Gregory A. Blaisdell
School of Aeronautics and Astronautics

Approved by:

Dr. Jay Gore
Head of the Graduate Program

Thesis work is dedicated to my family, Taenam Shin, Yeasook Chung, and Hyunho Shin. I am sincerely thankful to my family for their love, support, and sacrifices. I also dedicate this thesis to the memory of my grandfather, Inbong Shin, whose role in my life was, and remains, immense.

ACKNOWLEDGMENTS

I would like to first say a big thank you to my supervisor, mentor, and true teacher, Dr. J. Stuart Bolton for all the support and encouragement he gave me. Without his guidance this PhD would not have been achievable. Besides my advisor, I also thank the rest of my thesis committee: Dr. Charles M. Krousgrill, Dr. Jeffrey Rhoads, and Dr. Gregory A. Blaisdell, for their insightful comments.

I would also like to say a heartfelt thank you to Ray W. Herrick colleagues, Seungkyu Lee, Nicholas Kim, Janghyun Kim, Wonhong Choi, Weonchan Sung, Yangfan Liu, Rui Cao, Tongyang Shi, Yutong Xue, and Weimin Thor for helping in whatever way they could during this challenging period.

TABLE OF CONTENTS

LIST OF TABLES

LIST OF FIGURES

ABSTRACT

Author: Shin, Hyunjun. PhD
Institution: Purdue University
Degree Received: May 2019
Title: Weight Minimization of Sound Packages by Balancing Absorption and Transmission Performance
Committee Chair: J. Stuart Bolton, School of Mechanical Engineering.

Generally, heavier noise control treatments are favored over lighter ones since heavier acoustical materials tend to insulate (block) noise sources more effectively than do lighter materials. In automotive applications, however, heavier materials cannot always be adopted because of concerns over the total weight of the vehicle. Thus, it would be useful to identify lightweight acoustical treatments that can mitigate vehicle interior noise. Automotive sound packages have both absorption and barrier characteristics, and there is inevitably a trade-off between these two. Therefore, it is important to study the exchange between the absorption and transmission of acoustical materials particularly as it pertains to weight. Here, a procedure based on plane wave analysis is described that can be used to identify weight reduction opportunities by adjusting the acoustical properties of a generic sound package, consisting of a fibrous layer and a flexible microperforated panel surface treatment, so that it meets a target sound pressure level in a downstream interior space. It has been found, for the configuration studied here, that there are lightweight sound package configurations that can maintain acoustical performance equivalent to that of heavier noise treatments, and further, it has been found that the lightest treatments tend to favor barrier performance rather than absorption. Further, the impact of acoustical leaks has been considered, and it has been found that even very small leaks can result in a very substantial weight penalty if a specified level of acoustical performance is to be ensured. Further, the impact of changing the underlying panel mass and altering the frequency weighting used in the optimization process has also been considered.

The optimizer used in the proposed procedure requires considerable calculation time; hence, the acoustic pressure calculation time needs to be minimized to enhance the efficiency of the solution process. Thus, the transfer matrix method (TMM) for a two-dimensional case was used to calculate the interior acoustic pressure for a simple geometry as a starting point in the process of identifying the minimum-weight sound packages. The TMM is a widely used analytical

approach to predicting the sound pressure (and particle velocity) for a system that can be represented as a series of subsystems. Although the TMM can offer fast and simple calculations for the acoustic system, its application is limited to a plane-wave-based model. Thus, the TMM is not the best option for the acoustic pressure prediction in a complex geometry such as a vehicle interior, that involves non-planar wave propagation. Therefore, a hybrid TMM-FEA method is proposed in this research to evaluate the acoustical performance of the sound package in more complex geometries (here, a vehicle-like cavity). So, in this research, the TMM was introduced to obtain the initial solutions that can be used in conjunction with the FEA tool to calculate the sound pressure field in the complex geometry case. The correlation between the results of these two approaches was then analyzed to develop a space-averaged pressure prediction model for various absorptive cases in the interior space. Finally, this SAP prediction model was used to generate an acoustic map that can be used to graphically estimate the SAPs in the complex geometry case.

In order to validate the usage of the developed equation for different sets of boundary conditions, several case studies were performed to study the effects of the surface impedance arrangements, geometrical shapes, and, lastly, the presence of extra features in the interior space. Finally, the SAP difference between the area near the driver's right ear and the total interior cavity was studied to show that the SAP of the total cavity can be adjusted to evaluate the acoustic performance of the sound packages along the lines of conventional industry practice.

CHAPTER 1. INTRODUCTION

1.1 Impact of Sound Package Optimization in the Automotive Industry

One of the main issues that affects the fuel economy of an automobile is the vehicle weight, and so a large total vehicle weight limits the driving range of the automobile. To improve fuel mileage and battery mileage beyond current levels, the total weight of the vehicle must be reduced. Since the total weight of the conventional sound package for a luxury vehicle is around 120 lbs, efforts to minimize sound package weight are currently being actively pursued. However, the reduction of the sound package weight and the maintenance or improvement of acoustic performance are often mutually contradictory objectives, because, generally, a heavier material delivers better acoustic performance. In this research, a procedure for selecting sound package design parameters is introduced to demonstrate that the weight of the sound package can be minimized while its acoustic performance is preserved. In that case, the fuel economy can be improved and the passengers can still drive a quiet vehicle.

1.2 Trade Off Between Absorption and Transmission Loss

In general, acoustic materials serve dual roles: absorption and barrier performance. Barrier performance is required to prevent exterior sound from entering the vehicle interior, while absorptive performance is required to absorb sound after it has entered the vehicle interior. Here, absorption refers to the process of energy being dissipated within the material. In contrast, barrier performance, or transmission loss, refers to energy being blocked by the material. For example, good sound absorbing materials such as deep layers of glass fiber usually absorb most of the incoming sound energy, while, in the case of good barriers, like impermeable layers having a large mass/unit area, incoming sound is prevented from transmitting to the other side of the barrier because the barrier reflects most of the incoming sound energy. Therefore, it appears that there is an unavoidable contrast between these two different measures of acoustic performance. For example, highly absorptive acoustic materials generally have poor transmission performance since the energy coming toward the materials is generally not totally dissipated within the material, thus allowing some energy to transmit through the material. The balance of these two acoustic properties therefore controls the performance of the sound package. It follows that the compromise

between absorption and transmission performance, at some level, controls the weight of the sound package since highly absorptive materials tend to be lightweight, while effective barrier materials tend to have large masses per unit area. In the first part of this work, the absorption and transmission performance of optimized sound package are compared to establish the nature of this trade-off behavior.

1.3 Description of Sound Package Concept

As previously mentioned, sound packages serve both absorption and barrier roles. To perform these dual roles, the sound package consists of layers of different types of materials and each material serves a different function in the sound package. The generic sound package being analyzed here consists of only two layers for the sake of simplicity. The layout of the sound package is shown in Figure 1.1. A 30 mm thick, limp porous layer, which mainly serves to provide the absorption performance, is placed in series with a 0.2 mm thick, flexible microperforated panel (MPP) which can serve as either a barrier or an absorbing material depending on its open area and flow resistance. The sound package is then placed against a 1 mm thick aluminum panel which emulates the body part that isolates the vehicle cabin from the engine compartment. Thus, this treatment is a simplified representation of a dash panel sound package in which the perforated panel faces the vehicle interior.

1.4 Approach to Optimization

To optimize the weight of the sound package while maintaining its acoustic performance, the material properties of both the limp porous layer and flexible microperforated panel can be varied. Amongst the many different properties that define the materials, the flow resistance and the surface density were selected as the parameters to be varied because these two properties have the largest impact on the acoustic performance of a sound package. To quantify the acoustic performance of the sound packages, the space-averaged pressure in an air cavity placed behind the layered treatment (to represent the vehicle interior space) was calculated in the 500 Hz to 4000 Hz range, which is the speech interference band. To find the optimized properties of both materials, the surface densities and flow resistances for both the limp porous layer and the flexible MPP were systematically varied until the space-averaged pressure calculated after each iteration matched a

target value. Since there are many different combinations which can yield the same space-averaged pressure, 50 different combinations were considered as candidate starting positions. The details of the optimization method are introduced later in this thesis. Having obtained optimized sound packages for a very simple interior geometry, i.e., a duct, it was of interest to establish whether these same packages would perform as well in more realistic circumstances. So, a finite element model of a realistic vehicle geometry was developed that incorporated the sound package. That model was used to develop a mapping procedure that allows a target space-averaged pressure in one geometry to be translated to the corresponding level in a different geometry. As a result, the relatively simple and fast plane wave analysis can be used to find treatments that meet specific target in more complicated geometries.

1.5 Organization

There are a total of nine chapters in this thesis. The background and the objective of the research have been summarized in the first chapter. In the second chapter, literature related to this research is described: there are five sub-sections to the literature review and each sub-section summarizes information used in different parts of this research. In the third chapter, the modeling of a microperforated panel and a porous layer as an equivalent fluid is introduced for both rigid and flexible (limp) panel cases. Details of the transfer matrix method used to calculate the space-averaged pressure in the air cavity are discussed and also the optimization method and process are elaborated. A discussion of the balance between the absorption and transmission performance of a sound package is presented in Chapter 4. Then, several different case studies (impact of leakage, termination impedance, metal panel type, A-weighted and Octave frequency-band-based calculation) are presented in Chapter 5. The extension of the method to include a finite element analysis of the sound package is presented in Chapter 6, and a finite element approach to model a realistic vehicle interior cavity and the corresponding space-averaged pressure calculation method are demonstrated in Chapter 7. In Chapter 8, the procedure used to develop the empirical equation that can estimate the SAPs in the complex geometry cavity is described in detail. Finally, conclusions and suggested future work that needs to be performed to carry the research a step further are presented in Chapter 9.

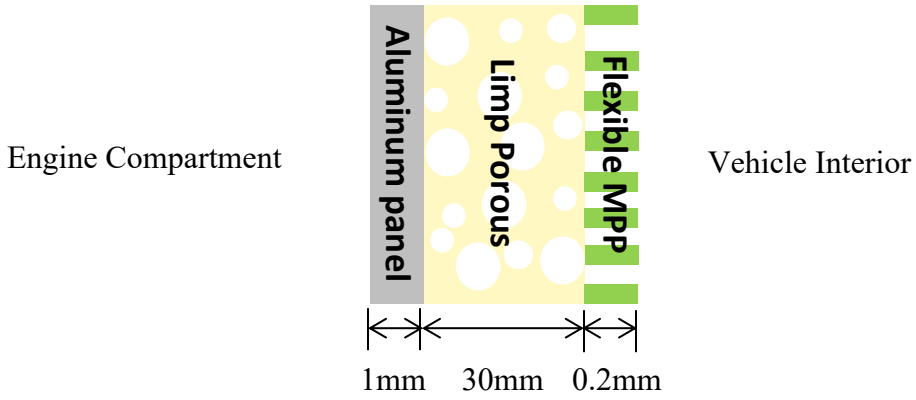

Figure 1.1: *A sound package layout.*

CHAPTER 2. LITERATURE REVIEW

In this chapter, the primary literature related to the sound package model components and the procedures used to find its optimized parameters is reviewed briefly. Recall that the sound package considered consist of a layer of limp fibrous media covered by a flexible MPP layer. Here, “limp” means that the in-vacuo bulk modulus of the solid phase of the fibrous layer is small compared to that of air. As a result, only a single compressional wave propagates within the material, with the result that it can be modeled as a fluid having complex properties: i.e., the density and bulk modulus.

2.1 Limp Porous Layer

Efforts to characterize limp porous media have been pursued by many acoustic researchers. Olny et al. introduced a way of calculating the complex density and bulk modulus of limp porous media by using the Johnson-Champoux-Allard (JCA) equivalent fluid model, in which the important physical properties are the flow resistivity, porosity, tortuosity, thermal/viscous characteristic lengths and, bulk density of the solid phase [1]. Panneton further investigated the low and high frequency limits of the limp porous media model [2]. The theory of Olny was used in the present work.

2.2 Flexible Microperforated Panel

There are many papers that describe the acoustic performance of rigid perforated panels; i.e., panels in which the solid component is not allowed to move. Here however, it was wished to model very lightweight perforated panels, say less than a few hundred grams per square meter. In that case the motion of the solid part of the panels in response to the sound field can have a significant impact on the performance of the panel and the material to which it is attached. There are only few acoustic researchers who have focused on characterizing such flexible perforated panels. Yoo and Bolton introduced an analytical approach to quantify the acoustic performance of flexible microperforated panels and compared the results with the measurements [3]. More recently, Herdtle and Bolton demonstrated that, to a good approximation, the surface density of the perforated panel can be added in parallel with the transfer impedance of the rigid microperforated

panel to derive the transfer impedance of the flexible microperforated panel [4]. The latter approach has been followed here.

2.3 Lightweight Sound Packages

Minimization of the weight of automotive sound packages, which can weigh as much as 120 pounds, has recently been emphasized in the automotive industry as a step towards improving fuel economy and reducing CO_2 emissions. Already, there have been several efforts directed at optimizing noise control treatments in order to minimize the weight of a vehicle. For example, Duval et al. introduced the Generalized Light-Weight Concept as an approach to reducing the weight of acoustic insulators, typically in dash panel applications [5]. Their concept emphasized the importance of balancing barrier and absorption properties to reduce the weight of treatments while giving targeted vehicle interior acoustic performance. In order to visualize the tradeoffs between absorption and transmission performance of acoustic materials, the Acoustic Galvanometer concept was introduced. To improve the accuracy of the optimization, a 3D approach was used [5-7] in combination with a 2D transfer matrix method (TMM) to find the optimized weight of noise treatments by balancing the absorption and transmission performance. In addition, Parrett et al. discussed the incorporation of microperforated materials in a vehicle dash mat (along with a fibrous layer). It was emphasized that the microperforated film composite offered comparable acoustic performance to conventional dual-density porous materials widely used in the automotive industry, and it also offered the possibility of balancing barrier and absorption performance by controlling the porosity of the microperforated material [8]. Zhang et al. have also illustrated a feasible scheme to reduce the weight of a sound package by using combinations of high and low density insulators [9]. Note also that the barrier performance of an automotive dashpanel is often limited by “leaks’ created by “pass throughs” i.e., holes formed in the dashpanel to allow controls, pipes, electrical wiring, HVAC systems, etc., to pass from the engine compartment to the vehicle interior. It is important to model the effect of those leaks if an accurate optimization of vehicle noise levels is to be performed. In terms of the leakage through acoustic materials, Verdiere et al. presented a method of simulating the air leaks by using a parallel assembly of air and the acoustic material [10].

In the present work, a general procedure for optimizing the weight of noise treatments is presented. The proposed method for finding the minimized weight of a sound package is illustrated

by considering a very simple sound package consisting of: a metal panel representing the panel separating the engine compartment from the vehicle interior, a relatively deep layer of limp porous media representing a layer of fibrous absorbent, and a surface treatment consisting of a flexible microperforated film whose porosity can be altered to control its absorption, barrier and dissipative properties. Also, In order to see the impact of air leakage on the sound package, air leakage was added to the model used for the optimization. A sound source was assumed to operate on the external side of the metal panel, and the acoustic output variable to be optimized was the space-averaged pressure in an interior acoustic space downstream of the sound package. To control the acoustic performance of the sound package, the flow resistance and surface density of the porous and microperforated layers were adjusted by an optimization routine that was started from many different random positions, with the objective of identifying the common characteristics of the lightest optimal solutions.

2.4 Optimization

In order to find the optimized weight of the sound package, the Genetic Algorithm (GA) was used in this research. The optimization process of the Genetic Algorithm is based on natural selection that emulates biological evolution. Kim and Bolton recently demonstrated the application of the GA to the optimization of the acoustic properties of the multi-layer microperforated panels [11].

2.5 Optimization of the Sound Package

Many researchers have directed their efforts towards optimizing the weight of sound packages in order to develop alternative treatments to replace conventional sound packages. Xie [12] et al. studied the lightweight design for a fibrous floor carpet by balancing sound insulation and sound absorption. Zhang et al. used a numerical Automatically Matched Layer (AML) approach to optimize a composite dash panel in order to achieve the desired interior sound pressure response [13]. Wu et al. used a Statistical Energy Analysis (SEA) model to optimize the vehicle dash sound package [14]. Gur et al. have also demonstrated sound package development of dash and floor subsystems by using statistical energy analysis (SEA) [15].

2.6 Summary

In this chapter, background research regarding the modeling of materials used in sound packages was first reviewed. For instance, the way that microperforated materials and porous media can be modeled as an equivalent fluid was described. Moreover, previous studies of lightweight sound packages were revisited. Finally, literature related to the weight optimization methods was recalled for future reference. Based on these preceding studies, an equivalent fluid model for both a flexible microperforated panel and a limp porous layer will be incorporated in the procedure for weight optimization of a sound package.

CHAPTER 3. MODELING OF A SOUND PACAKGE

As mentioned in the preceding chapters, a flexible microperforated panel provides the surface layer of the generic sound package considered here. Specifically, the interest lies in lightweight layers, and so the MPP, at least in principle can be forced into motion by the sound field, and so it is necessary to make the MPP layer "flexible". In this chapter, the approach to modeling a rigid (i.e., immovable) MPP as an equivalent fluid is described first, followed by a description of the original procedures that have been developed here to allow for the motion of the MPP.

3.1 Microperforated Panel Modeling

3.1.1 Rigid Microperforated Panel (JCA Model)

A microperforated panel is an acoustical material that consists of small holes, usually around 100μ in diameter, created in a thin panel; the holes create a surface porosity of typically around 1 percent. The combination of hole size and surface porosity (i.e., the number of holes per unit area) controls the static flow resistance of the panel. In response to sound, these sub-millimeter holes are filled by oscillatory viscous boundary layers, and the shearing of fluid that results provides controllable acoustic resistance: i.e., energy is dissipated within the holes. A microperforated panel is normally used in combination with an acoustic cavity behind it since a combination of the acoustic mass in the holes and the stiffness of the air backing creates a Helmholtz-type single degree of freedom resonator. Further, it has recently been shown that a microperforated panel can be acoustically characterized as a porous medium, which makes it possible to model an MPP as an equivalent fluid with complex density and bulk modulus [16].

As a result, both the limp porous layer and flexible MPP could be modeled as equivalent fluids by using the Johnson-Champoux-Allard (JCA) model [16-18]. The first step in that case is to obtain the complex density, $\tilde{\rho}_{eq}$, and bulk modulus, $\widetilde{K}_{eq}$, of the corresponding rigid porous material (i.e., a porous material in which there is no motion of the solid phase). The equivalent complex density of a rigid porous material is [19]

$$\tilde{\rho}_{eq} = \frac{\alpha_\infty \rho_0}{\phi}\left[1 + \frac{\sigma\phi}{j\omega\alpha_\infty\rho_0}\sqrt{1 + \frac{4j\eta\rho_0\omega\alpha_\infty^2}{\sigma^2\Lambda^2\phi^2}}\right] \tag{1}$$

and the complex bulk modulus of a rigid porous material is [18]

$$\widetilde{\mathrm{K}}_{eq}(\omega) = \frac{\gamma\, P_0/\phi}{\gamma - (\gamma-1)\left[1 - j\frac{8k}{\Lambda'^2 C_p \rho_0 \omega}\sqrt{\left(1 + j\frac{\Lambda'^2 C_p \rho_0 \omega}{16k}\right)}\right]^{-1}} \tag{2}$$

where,

$$\alpha_\infty = 1 + 2\frac{\varepsilon}{h} \tag{3}$$

$$\varepsilon = (1 - 1.13\xi - 0.09\xi^2 + 0.27\xi^3)\frac{8r}{3\pi} \tag{4}$$

$$\xi = 2\sqrt{\frac{\Phi}{\pi}} \tag{5}$$

$$\sigma = \frac{8\eta}{\Phi r^2}. \tag{6}$$

In these equations, α_∞ denotes the tortuosity, ε denotes the end correction length, η denotes the kinematic viscosity, ϕ is the open porosity, ρ_o is the ambient air density, k is the thermal conductivity, σ is the static air flow resistivity, γ is the ratio of specific heats, C_p is the specific heat at a constant pressure, Λ denotes the viscous chracteristic length and Λ' denotes the thermal characteristic length. For the rigid MPP case, both the viscous and thermal characteristic lengths are the same as the radius of the hole in the microperforated panel: i.e., $\Lambda' = \Lambda = r$.

In the next step, a transfer matrix is formed that relates the sound pressure and particle velocity on one side of the MPP to the sound pressure and particle velocity on the other side of the panel. Once the transfer matrix of the MPP is obtained, it can be combined with the transfer matrices of the other elements in the sound package to create a system transfer matrix that can, in turn, be used to calculate the system transmission loss and absorption properties.

When the complex density and bulk modulus of the rigid microperforated panel have been obtained, as above, the corresponding transfer matrix for the rigid MPP can be written as [20]

$$\begin{bmatrix} T_{11} & T_{12} \\ T_{21} & T_{22} \end{bmatrix} = \begin{bmatrix} \cos(k_{eq\_MPP}h) & jZ_{eq\_MPP}\sin(k_{eq\_MPP}h) \\ \dfrac{j\sin(k_{eq\_MPP}h)}{Z_{eq\_MPP}} & \cos(k_{eq\_MPP}h) \end{bmatrix} \tag{7}$$

where, $Z_{eq\_MPP} = \sqrt{\tilde{\rho}_{eq}\tilde{K}_{eq}}$ is the characteristic impedance and $k_{eq\_MPP} = \omega\sqrt{\tilde{\rho}_{eq}/\tilde{K}_{eq}}$ is the complex wave number of the equivalent fluid medium that is here representing the MPP, and where h is the MPP thickness. The next step is to obtain the transfer impedance of the rigid MPP, starting with a calculation of the reflection coefficient of a rigid MPP with an anechoic backing [20],

$$R_a = \frac{T_{11} + \left(\frac{T_{12}}{\rho_o c}\right) - \rho_o c\, T_{21} - T_{22}}{T_{11} + \left(\frac{T_{12}}{\rho_o c}\right) + \rho_o c\, T_{21} + T_{22}}. \tag{8}$$

Once R_a has been calculated, the surface impedance of a rigid microperforated layer can be calculated: i.e.,

$$Z_{s\_Rigid} = \rho_o c\left(\frac{1 + R_a}{1 - R_a}\right). \tag{9}$$

The transfer impedance of the rigid microperforated layer can then be calculated by subtracting the characteristic impedance of air from the surface impedance of the rigid microperforated layer with an anechoic backing: i.e.,

$$Z_{t\_Rigid} = \rho_o c\left(\frac{1 + R_a}{1 - R_a}\right) - \rho_o c = \frac{2\rho_o c R_a}{1 - R_a}. \tag{10}$$

The latter transfer impedance will then be used in the calculation of the transfer impedance of a flexible MPP.

3.1.2 Flexible Microperforated Panel

To calculate the transfer impedance of a flexible, microperforated panel, the impedance of a flexible, impermeable panel having mass per unit area, m_{MPP}, was added in parallel to the impedance of the rigid MPP [4]: i.e.,

$$Z_{t\_Flexible} = \frac{j\omega m_{MPP} Z_{t\_Rigid}}{Z_{t\_Rigid} + j\omega m_{MPP}}. \tag{11}$$

Once the transfer impedance of the flexible MPP was obtained in this way, the corresponding transfer matrix for the flexible MPP can be written as [21],

$$\begin{bmatrix} 1 & Z_{t\_Flexible} \\ 0 & 1 \end{bmatrix}. \tag{12}$$

3.2 Porous Layer as an Equivalent Fluid

The fibrous layer in the sound package system has been modeled here as a limp porous layer. That is, the solid phase of the porous material is considered to have a negligible stiffness compared to that of air. In that case, there is no independent free wave propagation through the structure, and so the material may be considered to be a fluid having complex properties that allows for a single longitudinal wave. In this case, the porous material is first modeled as being rigid, and then modifications are applied to allow for the motion of the solid part, which is simply "dragged along" by viscous effects when sound propagates through the fibrous layer.

3.2.1 Rigid Porous Layer (JCA Model)

First, according to the JCA model, and just as in the MPP case, the complex density of a rigid porous material is given by Equation (1), and the bulk modulus is given by Equation (2). The latter equation also applies to the limp porous material, but the complex density must be modified to allow for the solid phase motion.

3.2.2 Limp Porous Layer (JCA Limp Model)

Therefore, to complete the transformation from the rigid to the limp porous case, the complex density is calculated as [1,2]

$$\tilde{\rho}_{eq}^{limp} = \frac{A\tilde{\rho}_{eq}^{rigid} + B}{\tilde{\rho}_{eq}^{rigid} + C} \tag{13}$$

where $= \rho_{mat}$, $B = -\rho_o^2$, $C = \rho_{mat} - 2\rho_o$ and $\rho_{mat} = \rho_s + \phi\rho_o$, where ρ_s indicates the apparent density of the solid material. Once both the complex density and bulk modulus of the limp porous material have been calculated, the characteristic impedance and complex wave number for the limp porous material can be calculated as,

$$Z_{eq\_limp} = \sqrt{\tilde{\rho}_{eq}^{limp}\tilde{K}_{eq}} \tag{14}$$

$$k_{eq\_limp} = \omega\sqrt{\tilde{\rho}_{eq}^{limp}/\tilde{K}_{eq}} \tag{15}$$

and so the transfer matrix for a limp porous layer of thickness *h* can be written as,

$$\begin{bmatrix} \cos(k_{eq\_limp}h) & jZ_{eq\_limp}\sin(k_{eq\_limp}h) \\ \frac{j\sin(k_{eq\_limp}h)}{Z_{eq\_limp}} & \cos(k_{eq\_limp}h) \end{bmatrix}. \quad (16)$$

3.3 Acoustical Model

The next topic to be discussed in the assembly of the various components discussed above into a complete system that includes a noise source, the sound package, and an interior space where the sound level is to be controlled.

3.3.1 System Layout (Inlet + Sound Package + Air Interior Space + Termination)

The complete acoustical model is shown in Figure 3.1, and it features a very simple representation of an interior space in which the sound field is controlled by both the barrier and absorption properties of the acoustic treatment at the same time. The air cavity between the flexible microperforated panel and the termination was 500 mm long. The termination impedance was set to $11.25\rho c$, which yields an absorption coefficient of 0.3, typical of automotive interiors [22-24]. To quantify the acoustic performance of the noise treatment, the space-averaged pressure in the space between the noise treatment and the termination was calculated.

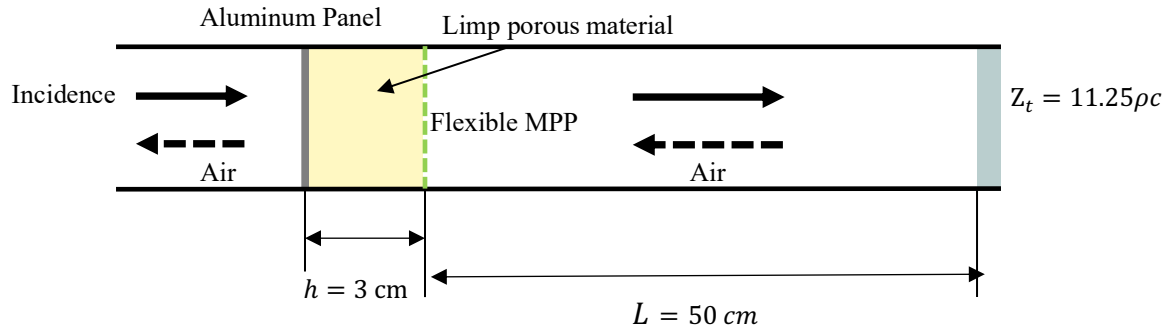

Figure 3.1: *Acoustic model used to predict the space-averaged mean square pressure in the air cavity.*

3.3.2 Sound Package Modeling (Rigid Plate + Elastic Porous + Flexible MPP)

The sound package considered here consisted of an aluminum plate lined with a layer of limp porous material and with a flexible microperforated panel attached to the surface of the porous

layer. The thicknesses of the aluminum plate, limp porous layer and flexible microperforated panel were 1 mm, 30 mm and 0.2 mm, respectively. An expanded view of the layout of this treatment is shown in Figure 3.2, although the figure is not scaled proportionally.

Figure 3.2: *Layout of the acoustic package.*

The properties of each of the materials are listed in Table 3.1. Since the flow resistance and surface density of both the limp porous layer and flexible MPP were varied in the optimization process, their values are intentionally left blank in the table. The values of viscous and thermal characteristic lengths are taken from reference [18] and are appropriate for fibrous media.

Table 3.1: Material properties of the sound package.

Material	**Surface Density (kg/m^2)**	**Thickness (mm)**	**Young's Modulus (Pa)**	**Poisson's Ratio**
Aluminum Plate	2.7	1	$69x10^9$	0.33
Limp Porous		30		
Flexible MPP		0.2		
Material	**Porosity**	**Thermal characteristic Length (m)**	**Viscous characteristic Length (m)**	**Tortuosity**
Limp Porous	0.995	$105x10^{-6}$		
Material	**Hole diameter (m)**			
Flexible MPP	$100x10^{-6}$			

3.4 Summary

In Chapter 3, the method of modeling the microperforated panels as an equivalent fluid by using the JCA model was demonstrated. Both rigid and flexible microperforated panels were modeled as equivalent fluids and the equations needed for the conversion were given explicitly. For the flexible microperforated panel, a parallel addition method was used to calculate its transfer impedance. Finally, the transfer matrix for the flexible microperforated panel was calculated based on the transfer impedance of the flexible microperforated panel.

The method of modeling the porous media as an equivalent fluid was also illustrated, step-by-step. The limp porous layer was modeled as an equivalent fluid by using a modified JCA model. Finally, the transfer matrix for a limp porous layer was also constructed so that it can be included in the assembly of the total transfer matrix for the sound package.

Finally, the acoustic model used to simulate the car interior air space was described. The purpose of this simple acoustic model was to allow the calculation of the sound pressure and the acoustic particle velocity in an interior space by using the transfer matrix method. The method used to build the transfer matrix of the sound package will be described in the next chapter.

CHAPTER 4. OPTIMIZATION PROCESS

4.1 Calculation Method

4.1.1 Transfer Matrix Modeling of the Sound Package

To calculate the space-averaged pressure in the air cavity space, the transfer matrix method (TMM) was used [17], and the detailed configuration of the model is shown in Figure 4.1.

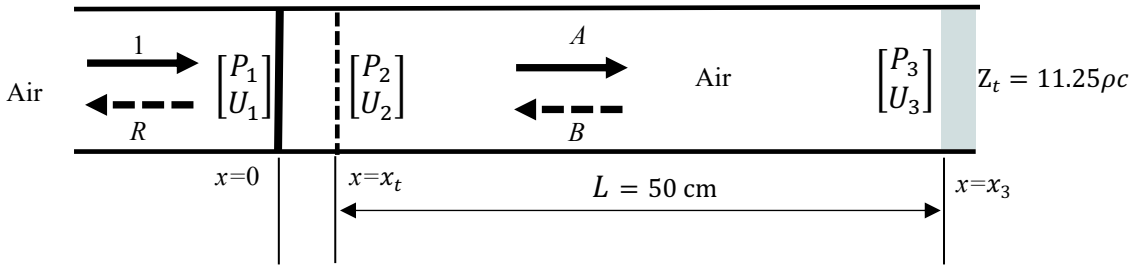

Figure 4.1: *TMM configuration.*

The transfer matrix [*N*] will be used to model the combination of the metal panel, porous layer and the microperforated surface treatment: i.e.,

$$\begin{bmatrix} P_1 \\ U_1 \end{bmatrix} = \begin{bmatrix} N_{11} & N_{12} \\ N_{21} & N_{22} \end{bmatrix} \begin{bmatrix} P_2 \\ U_2 \end{bmatrix} \tag{17}$$

while the [*L*] matrix is a transfer matrix accounting for the air space between the sound package and the termination: i.e.,

$$\begin{bmatrix} P_2 \\ U_2 \end{bmatrix} = \begin{bmatrix} L_{11} & L_{12} \\ L_{21} & L_{22} \end{bmatrix} \begin{bmatrix} P_3 \\ U_3 \end{bmatrix}. \tag{18}$$

To calculate the space-averaged pressure in the downstream, it is first necessary to solve for *A* and *B*, the complex amplitude of the downstream and upstream going waves, repeatedly. To obtain the values of *A* and *B*, it is first necessary to solve for P_2 and P_3.

To begin that process, Equation (17) can be rewritten as,

$$\begin{bmatrix} 1+R \\ \dfrac{1-R}{\rho c} \end{bmatrix} = \begin{bmatrix} N_{11} & N_{12} \\ N_{21} & N_{22} \end{bmatrix} \begin{bmatrix} P_2 \\ U_2 \end{bmatrix}. \tag{19}$$

from which *R,* the plane wave reflection coefficient, can be expressed in terms of P_2 and U_2: i.e.,

$$R = N_{11}P_2 + N_{12}U_2 - 1. \tag{20}$$

Then, by using the second row of Equation (19), R can be eliminated to give a relation between P_2 and U_2 : i.e.,

$$P_2 = \frac{2 - (\rho c N_{22} + N_{12})U_2}{\rho c N_{21} + N_{11}}. \tag{21}$$

Next, note that the impedance boundary condition at $x = x_3$ is $Z_t = \frac{P_3}{U_3}$. Thus, Equation (18) can be rewritten as,

$$\begin{bmatrix} P_2 \\ U_2 \end{bmatrix} = \begin{bmatrix} L_{11} & L_{12} \\ L_{21} & L_{22} \end{bmatrix} \begin{bmatrix} P_3 \\ \frac{P_3}{Z_t} \end{bmatrix} \tag{22}$$

from which, in combination with Equation (21), an expression for P_3 can be obtained:

$$P_3 = \frac{2}{(\rho c L_{11}N_{21} + L_{11}N_{11} + L_{12}N_{21}\frac{\rho c}{Z_t} + L_{12}N_{11}\frac{1}{Z_t} + \rho c L_{21}N_{22} + L_{21}N_{12} + L_{22}N_{22}\frac{\rho c}{Z_t} + L_{12}N_{12}\frac{1}{Z_t})}. \tag{23}$$

Then from Equation (22), P_2 can be expressed as

$$P_2 = (L_{11} + \frac{L_{12}}{Z_t})P_3. \tag{24}$$

Finally, P_2 and P_3 may be substituted into the expressions

$$P_2 = Ae^{-ikx_t} + Be^{ikx_t} \tag{25}$$

$$P_3 = Ae^{-ikx_3} + Be^{ikx_3} \tag{26}$$

in order to solve for A and B, at which point the sound field in the air space is fully determined. Note that a unit amplitude incident wave has been assumed, so that the sound field is, in effect, normalized by the strength of the incident sound field.

To find the total transfer matrix [*N*] which accounts for the metal panel, the limp porous layer and the flexible MPP, the transfer matrix of each of these materials was multiplied together to obtain,

$$\begin{bmatrix} N_{11} & N_{12} \\ N_{21} & N_{22} \end{bmatrix} = \begin{bmatrix} 1 & j\omega m \\ 0 & 1 \end{bmatrix} \begin{bmatrix} \cos(k_{eq\_limp}h) & jZ_{eq\_limp}\sin(k_{eq\_limp}h) \\ \frac{j\sin(k_{eq\_limp}h)}{Z_{eq\_limp}} & \cos(k_{eq\_limp}h) \end{bmatrix} \begin{bmatrix} 1 & Z_{t\_Flexible} \\ 0 & 1 \end{bmatrix} \tag{27}$$

where *m* is the mass per unit area of the metal panel. The matrix [L] is the transfer matrix for the air space between the noise treatment and the termination; and therefore takes the form

$$\begin{bmatrix} L_{11} & L_{11} \\ L_{21} & L_{22} \end{bmatrix} = \begin{bmatrix} \cos(k_{air}(x_3 - x_t)) & jZ_{air}\sin(k_{air}(x_3 - x_t)) \\ \frac{j\sin(k_{air}(x_3 - x_t))}{Z_{air}} & \cos(k_{air}(x_3 - x_t)) \end{bmatrix}. \tag{28}$$

Once the [L] and [N] matrices have been defined as above, then appropriate elements can be substituted into Equations (23) and (24) to obtain P_2 and P_3. Then, from Equations (25) and (26), A and B may be calculated as,

$$A = \frac{P_3 - P_2 e^{-ikx_t}}{e^{-ikx_3}(1 - e^{-2ikx_t})} \tag{29}$$

$$B = \frac{P_2(e^{-ik(x_t+x_3)} - e^{-ik(3x_t+x_3)} + e^{-2ikx_t}) - P_3 e^{-ikx_t}}{e^{-ikx_3}(1 - e^{-2ikx_t})}. \tag{30}$$

4.1.2 Space-Averaged Pressure Calculation

To calculate the space-averaged pressure, the air space behind the noise treatment was divided into 50 equally spaced sections. Then, the complex acoustic pressure at each node was obtained, as described in the last sub-section.

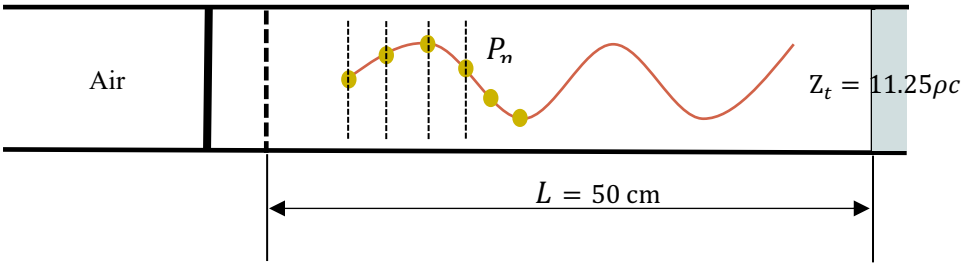

Figure 4.2: *Space-averaged pressure calculation.*

The pressure values at each point were then substituted into the expression

$$\frac{\sum_{n=1}^{51} \sqrt{\text{Re}\,(P_n)^2 + \text{Im}\,(P_n)^2}}{Total\ \#\ of\ Points} \tag{31}$$

to calculate the space-averaged sound pressure magnitude in the space.

4.2 Optimization

4.2.1 Genetic Algorithm

In order to search for the minimum surface density of the sound package given a certain space - averaged pressure in the air cavity, an optimization was performed by using a genetic algorithm: that procedure is described in this section. The main reason for choosing the genetic algorithm from amongst the many other optimization methods available was that the method provides

solutions that can be nearly optimal in non-convex cases, although a large computational effort is required. An embedded genetic algorithm function in the commercial software, MATLAB, was used for the calculation: the function used was GA.

The genetic algorithm optimization starts from initial populations which are the group of randomly chosen possible solution candidates. Here, randomly selected flow resistances and surface densities formed the initial populations. Then, the initial populations were evaluated and the algorithm scored each member of the population by calculating the fitness value. Members in the current population with lower fitness values were chosen as "elite" and the next generations were created based on these elites. These elites then went through the mutation stage, changing the previous values, the so called parents, and a cross-over stage, a combining of a pair of parents, which then formed the new generation. These processes were repeated until the solutions met the stopping criteria [25]. The Genetic Algorithm determines when to stop by using the following stopping conditions: the number of generations reaches the value of 100 times the number of variables; the algorithm reaches an amount of time in seconds that the user specified; the values of the fitness function for the best point in the current population is less than or equal to a Fitness limit; the average relative change in the fitness function value over the Stall generation is less than Function tolerance (The Stall generation was set to 50). That is, the algorithm stops when there is no improvement in the objective function during an interval of time in seconds equal to Stall time. Also, the algorithm stops if the average relative change in the fitness function value over the Stall generation is less than the Function tolerance, in this case, $1 \text{ X } 10^{-5}$. In this research, the randomly selected flow resistances and surface densities of the limp porous and the flexible MPP were transformed by going through the various genetic algorithm states until the outputs met the stopping criteria. In summary, the steps that the genetic algorithm performed to create optimized solution are illustrated in Figure 4.3.

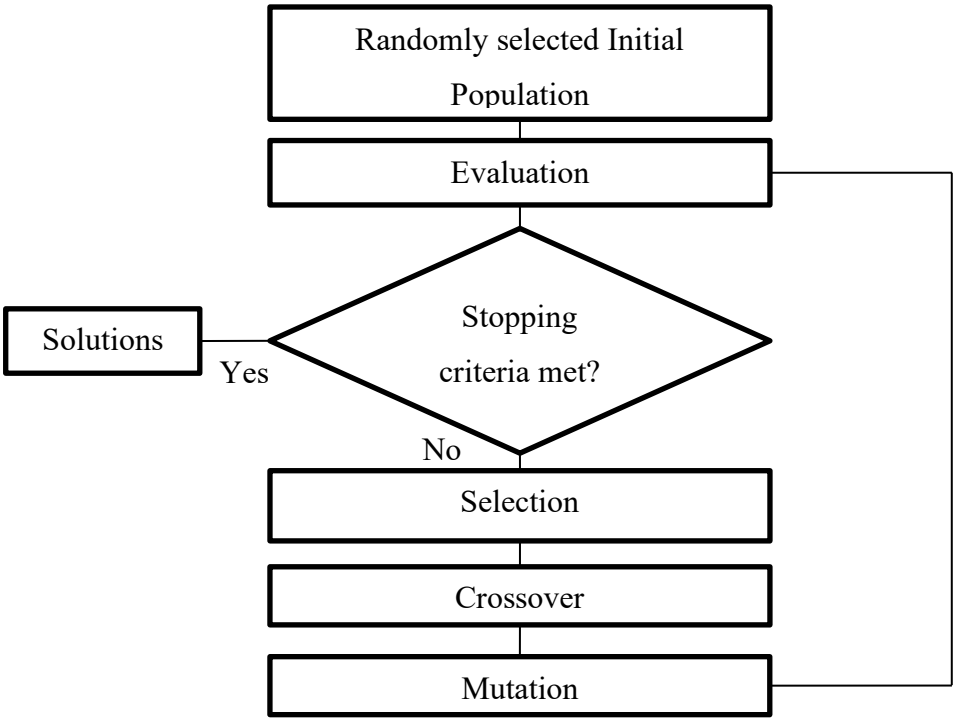

Figure 4.3: *Flow chart of the genetic algorithm.*

4.2.2 Optimization Process

Recall that the main goal of this study was to find the minimum surface density of the sound package required to meet a certain target space-averaged sound pressure (SAP) in the air cavity over the frequency range of 500 Hz to 4000 Hz, the speech interference range. The genetic algorithm (GA) was used to find a set of sound package surface densities and flow resistances that satisfied the specified SAP. The fitness function used in the optimization was therefore

$$\min\left(1-\frac{\mathrm{SAP}_{Current}}{\mathrm{SAP}_{Target}}\right), \tag{32}$$

which drives the solution as close to SAP_{Target} as possible. That is, in each iteration, the flow resistance and surface density of both the limp porous and flexible MPP were identified that gave the space-averaged pressure between 500 Hz and 4000 Hz ($SAP_{Current}$) that matched the targeted space-averaged pressure (SAP_{Target}). Here, the target space-averaged pressure magnitude in the interior space was initially defined as being within the range 60-63 dB, which lies within the

normal conversation range [26]. In particular, the target space-averaged sound pressure magnitude was chosen to be 0.019 Pa (59.6 dB) in the first calculations.

The upper and lower limits allowed for the various unknowns are listed in Table 4.1. Here, both flow resistances and surface densities were calculated by multiplying the thickness of the material by its flow resistivity and the volumetric mass density, respectively. Note that since the thickness of the limp porous layer was 3 cm, the volumetric densities were allowed to range from 1 kg/m^3 to 15 kg/m^3, and the flow resistivity from 3300 to 50000 MKS Rayls/m. These values span the range of feasible noise control materials.

Table 4.1: Upper and lower boundary for unknowns.

Material	**Surface Density (kg/m^2)**	**Flow Resistance (MKS Rayls)**
Limp Porous	[LB] 0.03 to 0.45 [UB]	[LB] 100 to 1500 [UB]
Flexible MPP	[LB] 0.1 to 3 [UB]	[LB] 100 to 1500 [UB]

The starting inputs for the optimization were randomly selected flow resistances and surface densities for both the limp porous layer and the flexible MPP. In particular, the GA was run 50 times to find 50 possible solutions.

The randomly selected initial values for both the limp porous layer and the flexible MPP were provided to the optimizer, which in each case yielded a different set of parameters that made it possible to meet the targeted space-averaged pressure magnitude. Since weight minimization was the objective here, the resulting surface densities of the limp porous layer and the flexible MPP were then added to give the total mass per unit area of the treatment. All of the resulting combinations that gave the targeted space-averaged pressure magnitude of 0.019 Pa are shown in Figure 4.4.

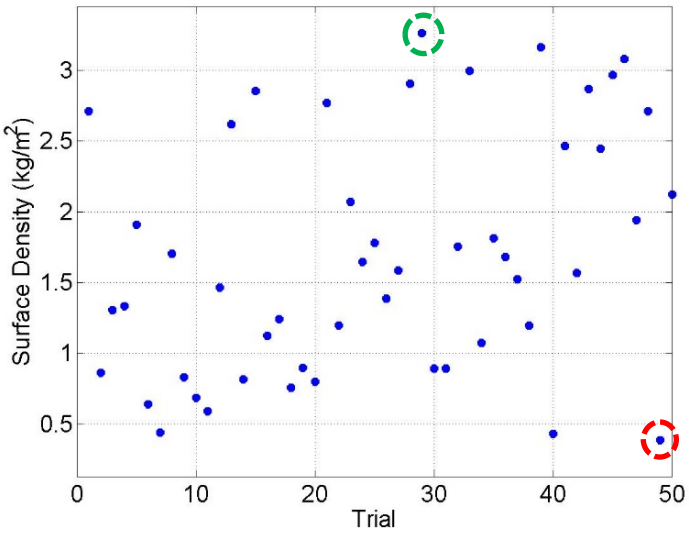

Figure 4.4: *Plots of various total surface densities that gave the targeted space-averaged pressure of 0.019 Pa.*

The results in Figure 4.4 indicate that there are many different combinations that can yield the same space-averaged pressure, and it is particularly notable that the surface densities span almost an order of magnitude. The dotted red circle indicates the smallest surface density, while the green dotted circle indicates the largest surface density. The surface density of the lightest combination obtained from these calculations was only 11 percent of that of heaviest weight combination. Table 4.2 indicates the total mass per unit area obtained from the optimization process for the heaviest and lightest results, and Table 4.3 gives the parameters for all solutions having a surface density less than 0.8 kg/m^2 that resulted in a space-averaged pressure of 0.019 Pa. It can be seen, very generally, that the majority of the mass was given to the MPP, while, with three exceptions, the flow resistance of the MPP was higher than that of the porous layer. Thus, it seems that a relatively massive and resistive MPP facing layer in combination with a relatively light and low flow resistance fibrous layer is the preferred solution for this sound package configuration and space average pressure.

Table 4.2: Lightest and heaviest total mass per unit area for both a limp porous and flexible MPP.

Material	Total mass per unit area (kg/m^2)	
Limp Porous + Flexible MPP	[Lightest Surface Density]	0.386
	[Heaviest Surface Density]	3.262

Table 4.3: The range of surface densities below 0.8 kg/m^2.

MPP		Limp Porous		Total
Flow Resistance (MKS Rayls)	**Surface Density (kg/m^2)**	**Flow Resistance (MKS Rayls)**	**Surface Density (kg/m^2)**	**Surface Density (kg/m^2)**
864.2	0.31	102.6	0.08	0.39
722.4	0.33	1026.6	0.11	0.44
1060.6	0.16	995.1	0.28	0.44
653.3	0.46	480.8	0.13	0.59
573.1	0.39	510.3	0.25	0.64
667.7	0.62	1286.4	0.07	0.69
665.3	0.71	995.1	0.05	0.76
606.5	0.62	305.2	0.18	0.80

4.2.3 Acoustic Performance Comparisons

After identifying the lightest and the heaviest surface density combinations, the absorption and transmission performance of the two results were compared to demonstrate that the lighter noise treatment could give a result comparable to the heavier noise treatment.

To calculate the absorption coefficient of the sound package, the reflection coefficient facing the flexible MPP with an anechoic termination was calculated using a matrix $[Q]$, where the $[Q]$ matrix is defined as,

$$\begin{bmatrix} Q_{11} & Q_{11} \\ Q_{21} & Q_{22} \end{bmatrix} = \begin{bmatrix} 1 & Z_{t\_Flexible} \\ 0 & 1 \end{bmatrix} \begin{bmatrix} \cos(k_{eq\_limp}h) & jZ_{eq\_limp}\sin(k_{eq\_limp}h) \\ \dfrac{j\sin(k_{eq\_limp}h)}{Z_{eq\_limp}} & \cos(k_{eq\_limp}h) \end{bmatrix} \begin{bmatrix} 1 & j\omega m \\ 0 & 1 \end{bmatrix}. \quad (33)$$

Then, the anechoic reflection coefficient is

$$R_a = \frac{Q_{11} + \left(\frac{Q_{12}}{\rho_o c}\right) - \rho_o c\, Q_{21} - Q_{22}}{Q_{11} + \left(\frac{Q_{12}}{\rho_o c}\right) + \rho_o c\, Q_{21} + Q_{22}} \tag{34}$$

and the absorption coefficient can then be calculated as,

$$\alpha_a = 1 - |R_a|^2. \tag{35}$$

Then the transmission loss of the anechoically-terminated sound package was also calculated. For the transmission loss calculation, the transfer matrix [N] was used and that result is

$$TL = 10 \log_{10}\left(\frac{1}{4}\left|N_{11} + \frac{N_{12}}{\rho_o c} + \rho_o c\, N_{21} + N_{22}\right|^2\right). \tag{36}$$

Figure 4.5 shows the absorption coefficient and transmission loss for the heaviest and lightest surface density combinations. The lightweight solution yielded the higher flow resistance and lower surface density for the flexible MPP, which resulted in the lower absorption performance than that of the heavier surface density case; however, the lighter solution actually provided better barrier performance than that of the heavier solution. Thus, it this particular case, it appears that barrier performance is favored over absorption performance. To summarize, the optimized parameters of both the lightest and heaviest noise treatments are given in Table 4.4.

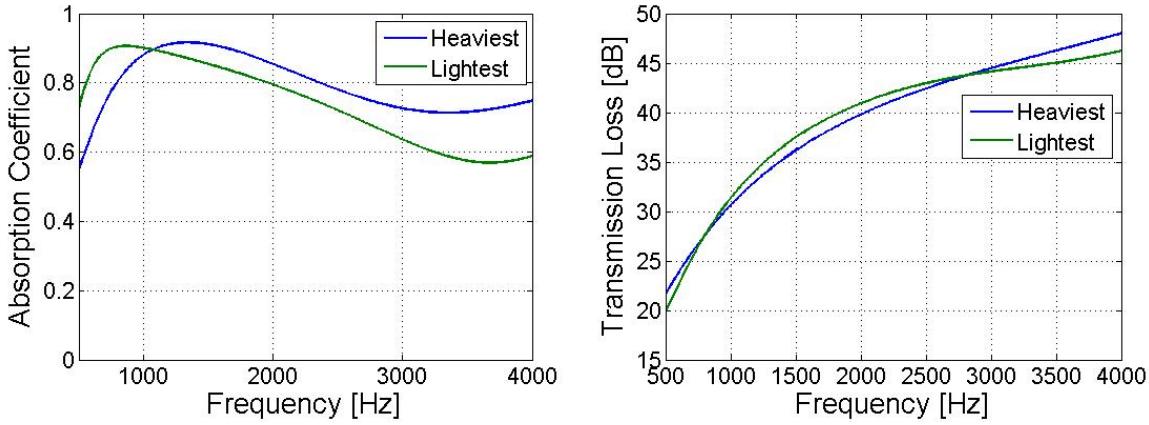

Figure 4.5: *Plots of lightest and heaviest surface density combinations (a) Absorption coefficient (b) Transmission Loss.*

Table 4.4: The parameters of both lightest and heaviest noise treatment.

Material	Flexible MPP	Limp Porous Layer	Total
Lightest Combination	Flow Resistance [MKS Rayls] 864.2	Flow Resistance [MKS Rayls] 102.6	
	Surface Density [kg/m^2] 0.31	Surface Density [kg/m^2] 0.08	Surface Density [kg/m^2] 0.39
Heaviest Combination	Flow Resistance [MKS Rayls] 503.7	Flow Resistance [MKS Rayls] 310.9	
	Surface Density [kg/m^2] 2.92	Surface Density [kg/m^2] 0.34	Surface Density [kg/m^2] 3.26

The space-averaged pressure magnitude in the air space for the two different cases is shown in Figure 4.6. The sound package with the lightest surface density yields a space-averaged pressure of 0.019 Pa while the heaviest treatment yields a pressure of 0.0191 Pa. Thus, the lighter noise treatment is comparable in performance to the heavier treatment in the frequency range between 500 Hz to 4000 Hz.

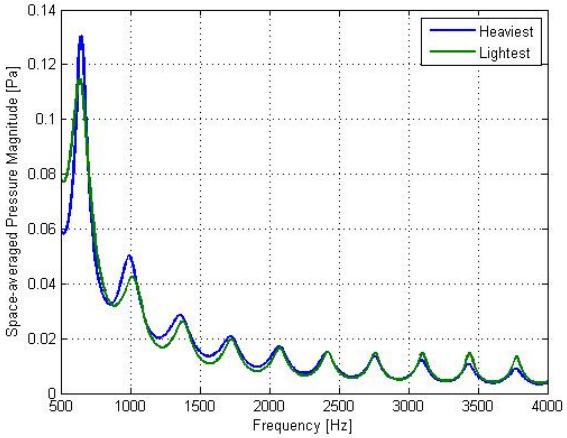

Figure 4.6: *Space-averaged pressure magnitude for both lightest and heaviest surface density combinations.*

To extend the results to a wider range of space-averaged pressure magnitudes in the cavity, target space-averaged pressure magnitudes ranging from 0.012 Pa to 0.04 Pa were selected, and the corresponding flow resistances and surface densities for both the limp porous layer and flexible MPP were obtained in the same manner as before. The results for the various targeted space-averaged pressures are shown in Figure 4.7, where both the lightest and heaviest solutions are plotted. From the "light" results, it can be seen that the amount of mass required to meet the performance target generally decreases as the target space-averaged pressure magnitude increases. Note that when the targeted space-averaged pressure was either below 0.01 Pa or above 0.034 Pa, the final values of the surface density tended to meet either the upper or lower boundary limits. Nevertheless, the difference between the red and blue lines indicates the possible weight reduction that can be achieved while maintaining good acoustical performance.

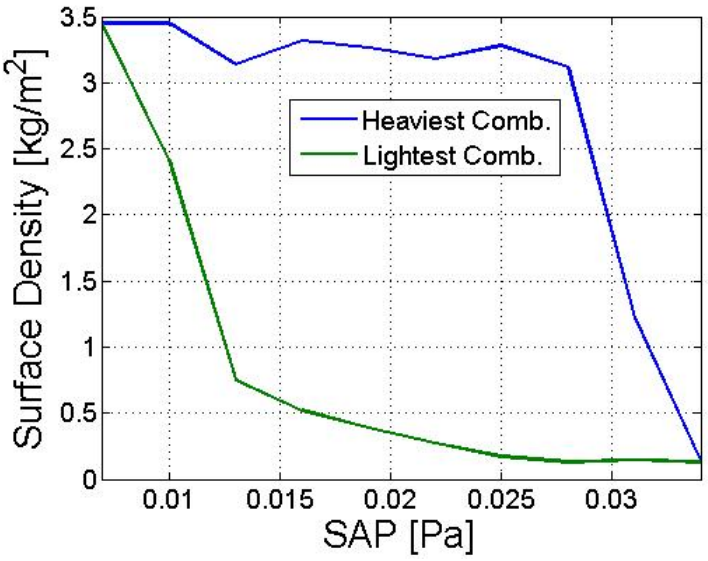

Figure 4.7: *Total surface density for various space averaged pressure.*

The results shown in Figure 4.8 indicate that many different combinations can yield the same solution for the various space-averaged pressure magnitudes between 0.01 Pa and 0.034 Pa in the air space. As noted, it is generally observed that surface densities tend to go up to either the upper bound which is 3.45 kg/m^2 at 0.01 Pa (a) or the lower bound which is 0.13 kg/m^2 at 0.034 Pa (i).

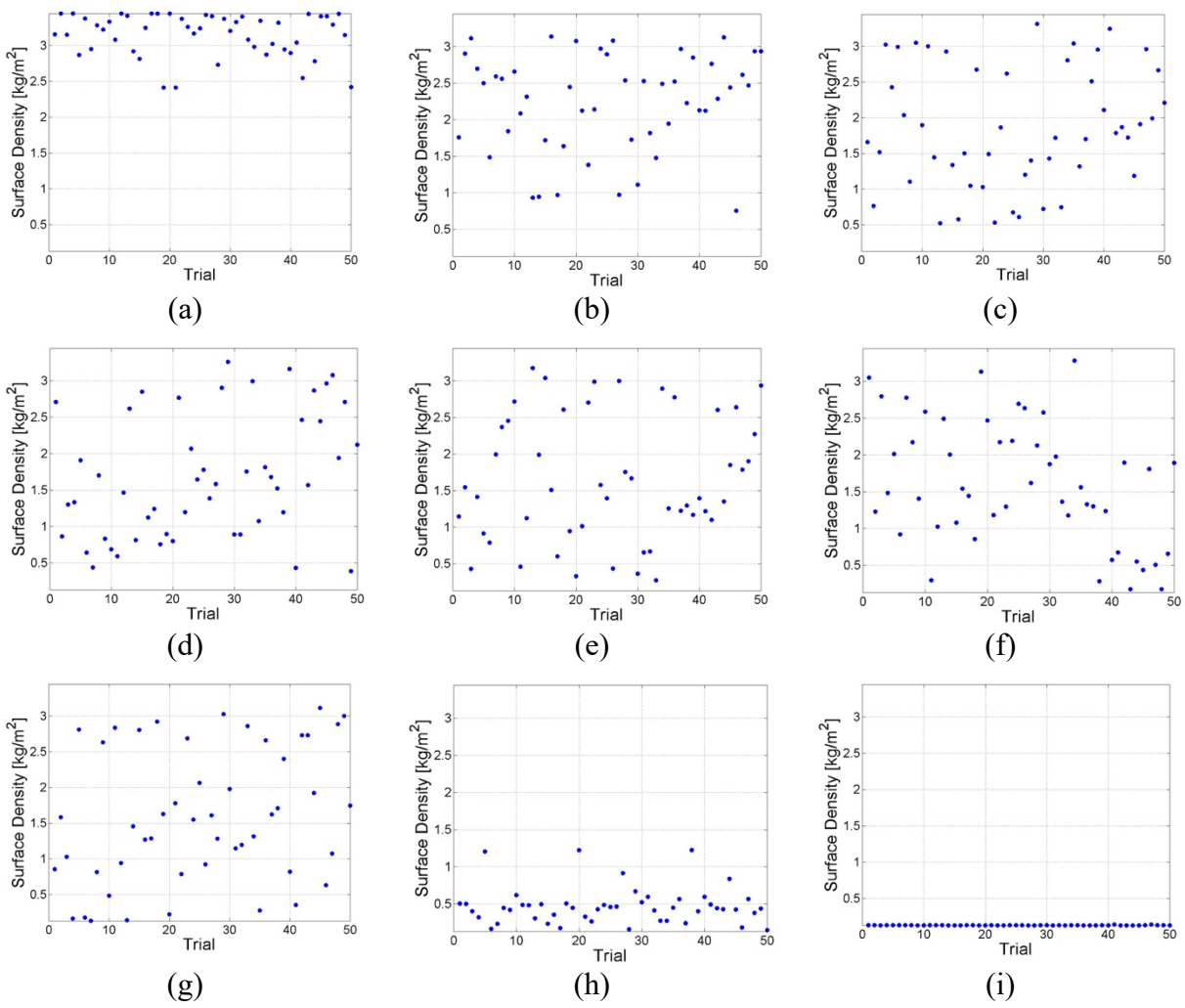

Figure 4.8: *Plots of various total surface densities that gave the targeted space-averaged pressure magnitude of (a) 0.01 Pa (b) 0.013 Pa (c) 0.016 Pa (d) 0.019 Pa (e) 0.022 Pa (f) 0.025 Pa (g) 0.028 Pa (h) 0.031 Pa (i) 0.034 Pa.*

In Table 4.5, both the lightest and heaviest surface densities for various space-averaged pressure magnitudes are shown. It can be seen that as the target SAP decreases, the surface density of the lightest combinations increases monotonically, while the surface density of the heaviest combinations remains approximately constant. Note also that a reduction of SAP by a factor of two, i.e., from 0.025 Pa to 0.013 Pa requires a fivefold increase in surface density. Thus, as the target SAP decreases, the weight penalty increases very rapidly. The results for the heaviest and lightest cases for the intermediate sound pressure, 0.013 Pa to 0.028 Pa are collected in Table 4.6 where again, with one exception, it can be seen that the optimal, lightweight, solutions feature relatively massive, and resistive MPP's compared to the fibrous layer.

Table 4.5: The total surface densities for various space-averaged pressure magnitudes.

	Total Surface Density	
SAP (Pa)	**Lightest Combination (kg/m^2)**	**Heaviest Combination (kg/m^2)**
0.013	0.755	3.141
0.016	0.523	3.317
0.019	0.386	3.262
0.022	0.271	3.179
0.025	0.174	3.282
0.028	0.132	3.116

Table 4.6: The material properties for various space-averaged pressure magnitudes.

SAP [Pa]	**MPP**		**Limp Porous**		**Total**
	Surface Density (kg/m^2)	**Flow Resistance (MKS Rayls)**	**Surface Density (kg/m^2)**	**Flow Resistance (MKS Rayls)**	**Surface Density (kg/m^2)**
0.013	0.446	1397.3	0.2889	1178.1	0.755 (Lightest)
	2.907	1179.0	0.2337	829.5	3.141 (Heaviest)
0.016	0.3299	1420.2	0.1927	373.1	0.523 (Lightest)
	2.924	780.7	0.3924	258.3	3.317 (Heaviest)
0.019	0.311	864.2	0.0752	102.6	0.386 (Lightest)
	2.923	503.7	0.339	310.9	3.262 (Heaviest)
0.022	0.133	1040.1	0.139	1004.2	0.272 (Lightest)
	2.995	317.9	0.185	590.4	3.180 (Heaviest)
0.025	0.104	730.1	0.071	343.7	0.175 (Lightest)
	2.960	137.4	0.322	474.0	3.282 (Heaviest)
0.028	0.100	261.5	0.032	100.0	0.132 (Lightest)
	2.961	124.4	0.155	124.6	3.116 (Heaviest)

4.3 Acoustical Performance Analysis of Optimization Results

4.3.1 Trade Off Between Absorption and Transmission Performance

Earlier in this document, it was suggested that there is a tradeoff between absorption and transmission performance that operates in the optimization process of reducing the weight of sound packages. To study this tradeoff behavior more deeply, both the absorption coefficients and transmission losses for the sound packages that yielded various target space-averaged pressure magnitudes have been plotted in Figure 4.9. It is clear from the absorption results, that the absorption generally increases (and its peak shifts to higher frequencies) as the target SAP increases, and this behavior is true for both the lighter and heavier treatments.

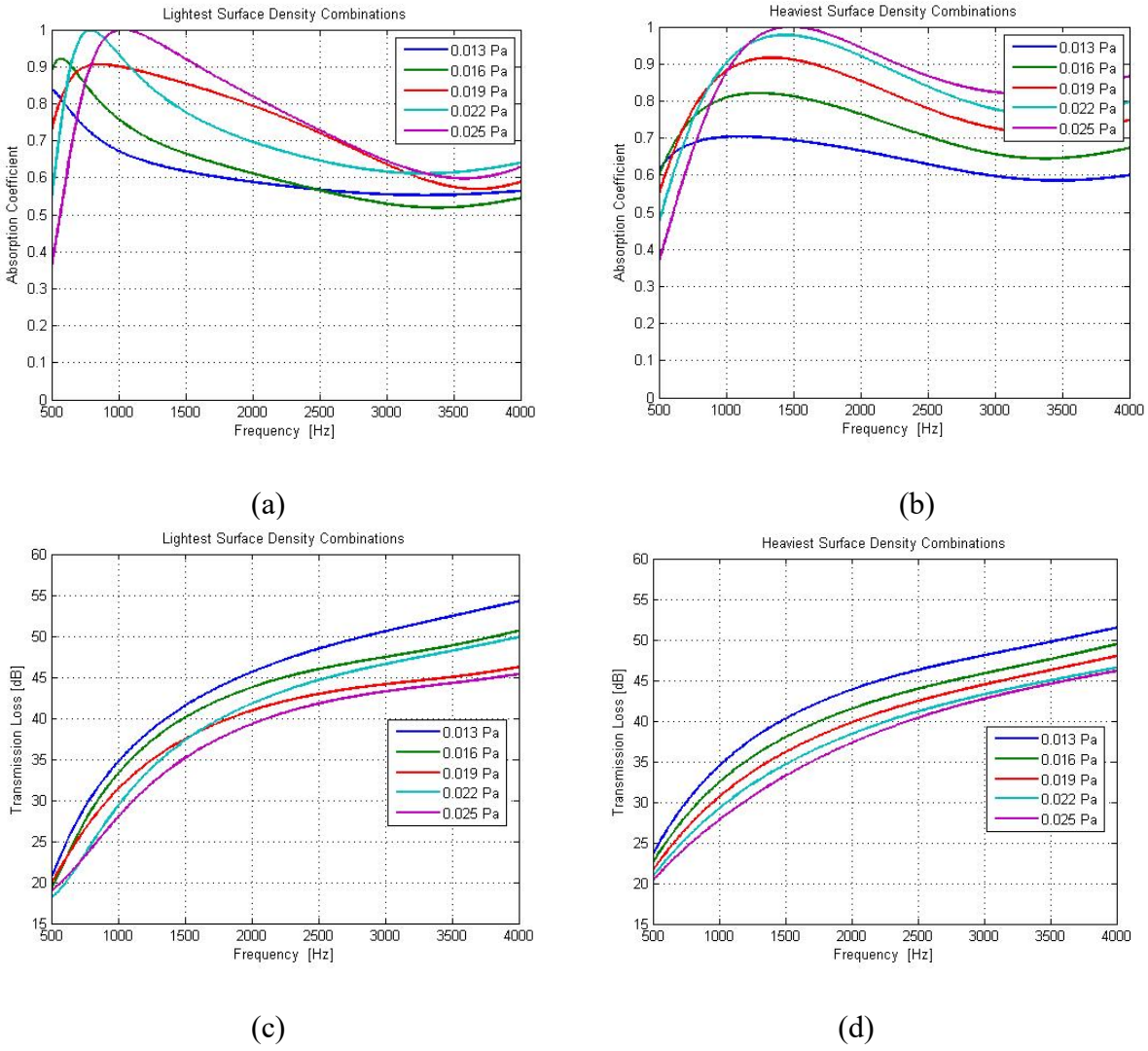

Figure 4.9: *Plots of acoustic performances for various space-averaged pressure magnitudes for an aluminum panel. Absorption coefficient of (a) lightest (b) Heaviest weight combinations. Transmission loss of (c) lightest (d) Heaviest weight combinations.*

From the transmission loss results, it can be seen that the transmission loss increases steadily as the target SAP decreases. That trend is true without exception in the heavy results, but is not quite so clear in the light results. Together, these results suggest that a combination of relatively high barrier performance and relatively low absorption are required to achieve the lowest SAP's at the lowest surface densities.

To demonstrate the tradeoff behavior between absorption and transmission performance, sound packages with different surface densities that yielded a space-averaged pressure magnitude of 0.022 Pa (light blue solid line) were selected and are compared in Figure 4.10.

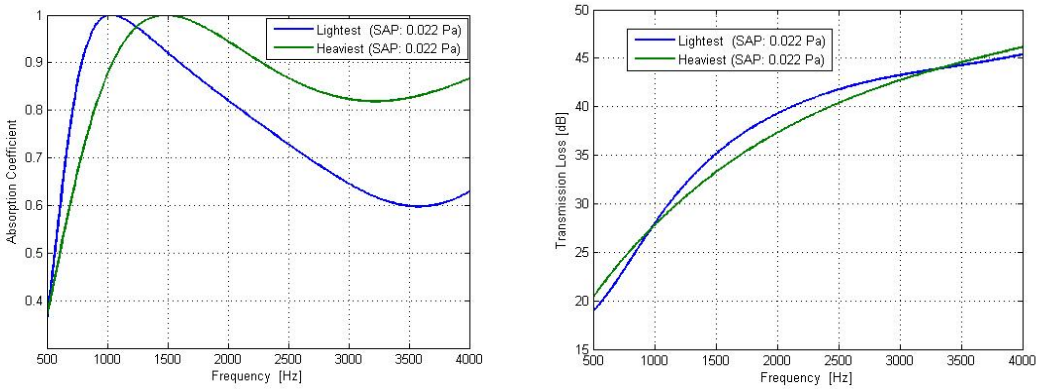

(a) (b)

Figure 4.10: *Plots of (a) Absorption coefficient which yields the space-averaged pressure of 0.022Pa (b) Transmission loss which yields the space-averaged pressure of 0.022 Pa.*

In Figure 4.10 (a), it can be seen that the sound package with the lowest surface density (Blue solid line) gives lower absorption performance than that of the highest surface density (Green solid line). Further, the sound package with the lightest surface density (Blue solid line) yielded a higher transmission loss (Figure 4.10 (b)) at the same space-averaged pressure in the air cavity between 500 Hz to 4000 Hz. These results serve to illustrate that two quite different solutions can give the same SAP: see Figure 4.11. And note that, as shown in Table 4.6, the "light" solution weighed less than 10 percent of the "heavy" solutions.

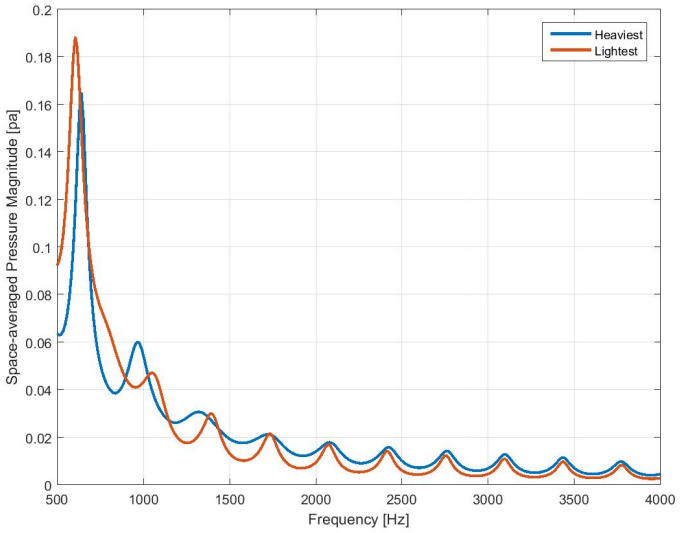

Figure 4.11: *The space-averaged pressure of 0.022Pa for both the lowest and the highest surface density.*

4.4 Summary

In this chapter, the transfer matrix method that was used to calculate the sound pressure and the particle velocity at certain locations in the interior air space was formulated. To quantify the acoustic performance of the sound package, the space-averaged pressure was introduced. The space-averaged pressure was used in the sound package optimization process described here.

The process of optimizing the weight of the sound package was described, as were the results. The optimization process gave many different flow resistivity and surface density combinations that yielded the same space-averaged pressures. From these optimization results, the possible weight reduction range was identified. Generally, it was found that a combination of a relatively heavy, high flow resistance MPP with a relatively light fibrous layer gave the lowest weight solutions at a given SAP for this particular sound package configuration.

The tradeoff between absorption and transmission of the acoustical material was also demonstrated. In particular, it was demonstrated that the space-averaged pressure in the air cavity depends on both the absorption and transmission performance of the sound package, and it was shown that in the lightest sound packages, barrier performance was favored over absorption performance, for the particular case considered here.

CHAPTER 5. CASE STUDIES

As mentioned earlier, the performance of dashpanel sound package treatments can be limited by the existence of air-leaks caused by the pass-throughs that allow cabling, controls, pipework, and ducts to enter the passenger compartment from the engine compartment. The disproportionate impact of leaks comes from the fact that an opening has a transmission loss of approximately zero. As a result, an open area of 1cm^2 can transmit as much acoustical energy as a 1000 cm^2 area having a transmission loss of 30 dB. In this chapter, the incorporation of acoustic leaks into the optimization process is described, and their effect on the outcome is demonstrated.

In addition, additional case studies are described: the first demonstrating the effect of replacing the aluminum panel with a steel panel, a second illustrating of the effect of increasing the termination impedance in the model, i.e., reducing the interior absorption coefficient, and finally, the effect of objective functions having different frequency weightings is considered.

5.1 Leakage Case

It is hard to manage and completely eliminate leaks (i.e., areas of low transmission loss) when a sound package is installed on the dash panel and generally, leaks have a larger impact on the transmission performance than the absorption. Therefore, the contribution of leaks to the acoustic performance of the sound package should be examined closely, and thus, here, leakage through the sound package is considered in the weight minimization process. To account for the leakage in the sound package, a parallel assembly of transfer matrices was used to model the heterogeneous material [10, 27]. Figure 5.1 shows a schematic of the sound package layout with a leak. For convenience, the leakage is modeled here as a small open area (and note that a two-component barrier having a transmission loss of 30 dB over 90 percent of its area and a transmission loss of 10 dB over 10 percent of its area, is approximately equivalent to a two-component barrier having a transmission loss of 30 dB over 99 percent of its area and a transmission loss of 0 dB over 1 percent of its area, as in the first example below).

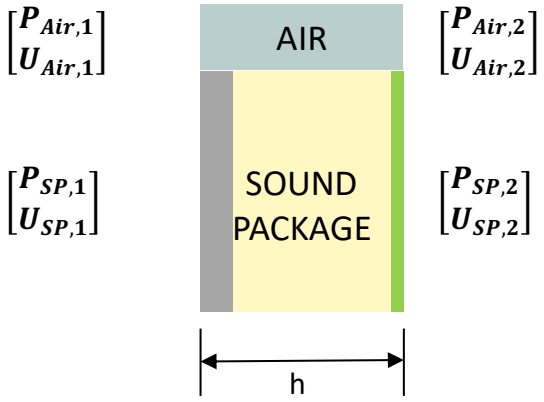

Figure 5.1: *Layout of the sound package with air leaks.*

To construct the transfer matrix of the sound package with air leaks, admittance matrices for both the air leaks and the sound package need to be constructed, starting from the transfer matrix of an air space, which is

$$\begin{bmatrix} P_{Air,1} \\ U_{Air,1} \end{bmatrix} = \begin{bmatrix} \cos kh & jZ \sin kh \\ j/Z \sin kh & \cos kh \end{bmatrix} \begin{bmatrix} P_{Air,2} \\ U_{Air,2} \end{bmatrix} \tag{37}$$

where, Z is the characteristic impedance of air, k is the wave number, and h is the thickness of the air space. The latter matrix may be manipulated to yield the admittance transfer matrix which is constructed as follows

$$\begin{bmatrix} U_{Air,1} \\ U_{Air,2} \end{bmatrix} = \frac{1}{jZ \sin kh} \begin{bmatrix} \cos kh & -1 \\ 1 & -\cos kh \end{bmatrix} \begin{bmatrix} P_{Air,1} \\ P_{Air,2} \end{bmatrix} = \begin{bmatrix} Y_{1,11} & Y_{1,12} \\ Y_{1,21} & Y_{1,22} \end{bmatrix} \begin{bmatrix} P_{Air,1} \\ P_{Air,2} \end{bmatrix}. \tag{38}$$

In addition, the transfer matrix for the sound package without air leakage is

$$\begin{bmatrix} P_{SP,1} \\ U_{SP,1} \end{bmatrix} = \begin{bmatrix} N_{11} & N_{12} \\ N_{21} & N_{22} \end{bmatrix} \begin{bmatrix} P_{SP,2} \\ U_{SP,2} \end{bmatrix} \tag{39}$$

where $[N]$ is the transfer matrix of the sound package used in Chapter 4. The latter may be transformed to give the admittance transfer matrix,

$$\begin{bmatrix} U_{SP,1} \\ U_{SP,2} \end{bmatrix} = \frac{1}{N_{12}} \begin{bmatrix} N_{22} & N_{21}N_{12} - N_{22}N_{11} \\ 1 & -N_{11} \end{bmatrix} \begin{bmatrix} P_{SP,1} \\ P_{SP,2} \end{bmatrix} = \begin{bmatrix} Y_{2,11} & Y_{2,12} \\ Y_{2,21} & Y_{2,22} \end{bmatrix} \begin{bmatrix} P_{SP,1} \\ P_{SP,2} \end{bmatrix}. \tag{40}$$

To solve for the unknown pressure and velocities at the front and back surfaces of the composite treatment, acoustic pressure and velocity continuity boundary conditions need to be applied. The pressure continuity boundary conditions can be written as

$$\begin{bmatrix} P_{Air,1} \\ P_{Air,2} \end{bmatrix} = \begin{bmatrix} P_1 \\ P_2 \end{bmatrix} \text{ and } \begin{bmatrix} P_{SP,1} \\ P_{SP,2} \end{bmatrix} = \begin{bmatrix} P_1 \\ P_2 \end{bmatrix}. \tag{41}$$

Similarly, the velocity continuity boundary conditions can be written as

$$\begin{bmatrix} U_1 \\ U_2 \end{bmatrix} = \sum r_i \begin{bmatrix} U_{Air,1} \\ U_{Air,2} \end{bmatrix} \text{ and } \begin{bmatrix} U_1 \\ U_2 \end{bmatrix} = \sum r_i \begin{bmatrix} U_{SP,1} \\ U_{SP,2} \end{bmatrix} \tag{42}$$

where r_i is the surface area ratio which indicates the ratio between the surface area of air-leaks and that of the sound package. That ratio was calculated as

$$r_i = S_i / S_{total} \tag{43}$$

where, S_i is the cross-sectional surface area of element i and S_{total} is the total cross-sectional surface area. Then, Equations (38) and (40) can be combined to form

$$\begin{bmatrix} U_1 \\ U_2 \end{bmatrix} = \sum r_i \begin{bmatrix} Y_{i,11} & Y_{i,12} \\ Y_{i,21} & Y_{i,22} \end{bmatrix} \begin{bmatrix} P_1 \\ P_2 \end{bmatrix}. \tag{44}$$

Next, the latter matrix needs to be converted to a form that can be used in the transfer matrix method approach, i.e., to the form

$$\begin{bmatrix} P_1 \\ U_1 \end{bmatrix} = \begin{bmatrix} T_{11} & T_{12} \\ T_{21} & T_{22} \end{bmatrix} \begin{bmatrix} P_2 \\ U_2 \end{bmatrix} \tag{45}$$

where the $[T]$ matrix is now

$$\begin{bmatrix} T_{11} & T_{12} \\ T_{21} & T_{22} \end{bmatrix} = \frac{-1}{\sum r_i Y_{i,21}} \begin{bmatrix} \sum r_i Y_{i,22} & -1 \\ \sum r_i Y_{i,22} \sum r_i Y_{i,11} - \sum r_i Y_{i,12} \sum r_i Y_{i,21} & -\sum r_i Y_{i,11} \end{bmatrix}. \tag{46}$$

In Equation (46), Y_i is the admittance transfer matrix of the ith element.

Once the total transfer matrix for the sound package with air-leaks has been constructed, the space-averaged mean square pressure in the interior space can be calculated in the same manner as in the no-leakage case. To demonstrate the effect of the air leakage on the acoustic performance, the absorption coefficients and transmission losses of a sound package with either no leakage or 1.0 percent leakage are plotted in the Figure 5.2. The material values used in these calculations are listed in Table 5.1.

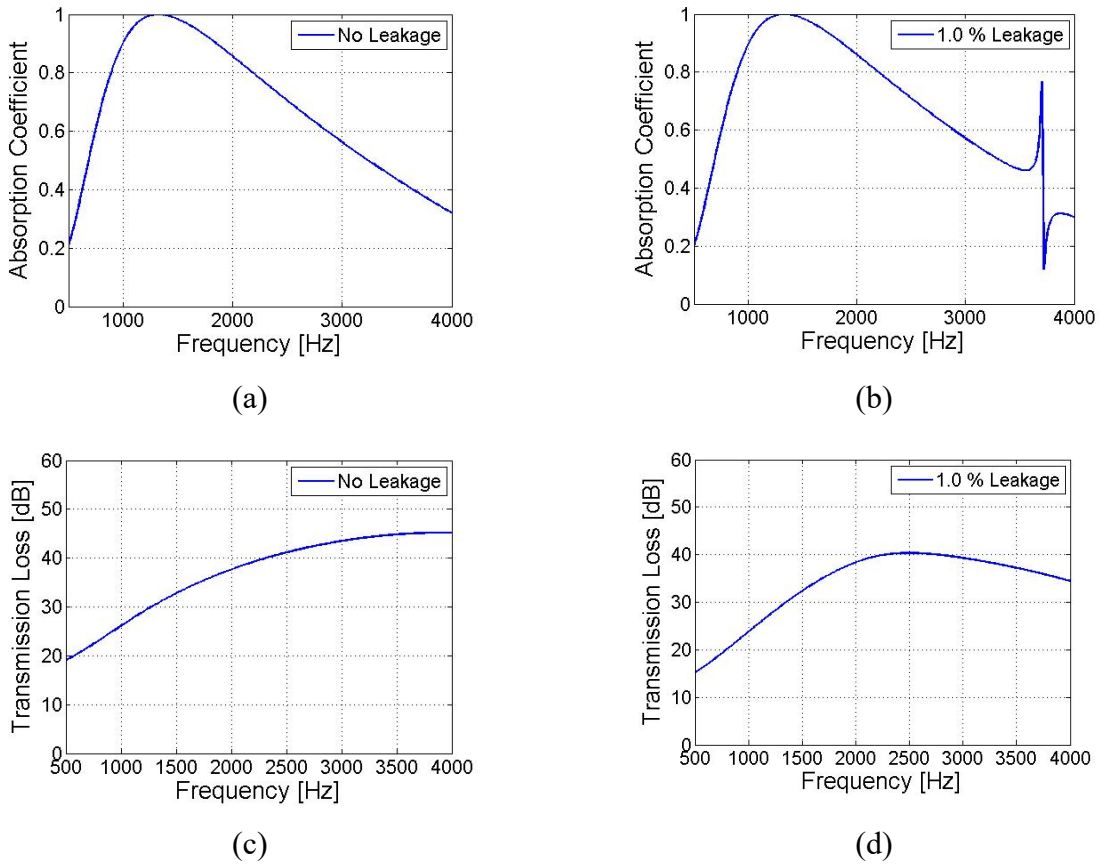

Figure 5.2: *Absorption coefficient and transmission loss for both (a), (c) No leakage (b), (d) 1.0 percent leakage cases.*

As shown in the plots above, when there is air leakage, the absorption performance of the sound package was not significantly affected except for a narrow feature related to a depth resonance; in contrast, the transmission loss is substantially reduced by the air leakage.

Table 5.1: The parameters of acoustic material for both no-leak and 1.0 percent leak cases.

	Flexible MPP	**Limp Porous Layer**	**Total**
Acoustic Material	Flow Resistance [MKS Rayls] 762.2	Flow Resistance [MKS Rayls] 1493	
	Surface Density [kg/m^2] 0.16	Surface Density [kg/m^2] 0.05	Surface Density [kg/m^2] 0.21

Once the transfer matrix of the sound package with leaks was constructed, the surface density optimization was performed in the same manner as in the no-leakage case. The only necessary change in the optimization process was to replace the [*N*] matrix with the [*T*] matrix for the transfer matrix of the sound package which now incorporates leaks. The results in Figure 5.3 indicate the possible surface density combinations, with 0.5 percent air leakage in the sound package, that yielded the space-averaged pressure magnitudes between 0.013 Pa and 0.041 Pa (i.e., 56.3 dB to 66.2 dB, respectively) in the air space. As before. it was observed that the surface densities tended to rise to the upper bound, which was 3.45 kg/m^2, below 0.016 Pa (58.1 dB) and fell to the lower bound, which was 0.13 kg/m^2, above 0.041 Pa (66.2 dB). And, once again, it can be seen that in the middle range of SAP's there is a wide range of possible solutions having widely different surface densities.

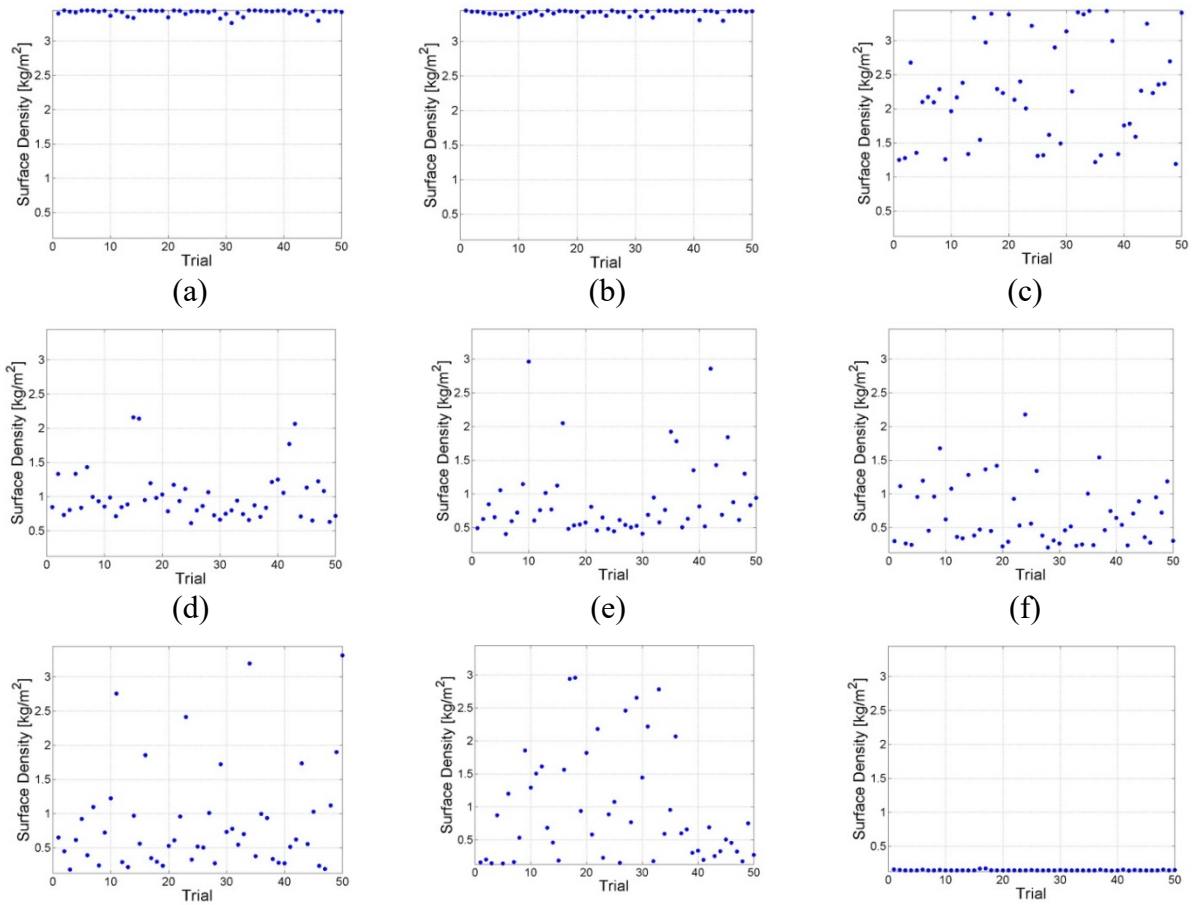

Figure 5.3: *Plots of various total surface densities that gave the targeted space-averaged pressure magnitude of (a) 0.013 Pa (b) 0.016 Pa (c) 0.019 Pa (d) 0.022 Pa (e) 0.028 Pa (f) 0.031 Pa (g) 0.034 Pa (h) 0.041(i) 0.043 Pa.*

Figure 5.4 (a) shows the heaviest and lightest surface density results for the complete range of SAP's. The limiting behavior at high and low SAP's is clearly visible here, as is the large range of possible surface densities in the middle range. When leakage is incorporated into the sound package, the space-averaged pressure in the interior space at a given total surface density increases compared to the no-leakage case.

The lightest sound package surface density combinations for both the leakage and no-leakage cases are plotted in Figure 5.4 (b) in order to demonstrate the impact of the leakage on the sound package performance. As shown in Figure 5.4 (b), there is very large weight penalty that results from even a small amount of leakage: e.g., in the presence of air-leakage, the surface density required to achieve a space-averaged pressure of 0.018 Pa (59.1 dB) increased by a factor of 4.

To illustrate the effect of the leaks on the sound package performance, the absorption coefficients and the transmission losses of the lightest and heaviest sound packages with and without leakage which yielded the space-averaged pressure of 0.022 Pa (60.8 dB) are shown in Figure 5.5. The lightest surface density in the leakage case was 0.62 kg/m^2, while in the no-leakage case, it was 0.27 kg/m^2: thus, it is clear once again that a significant weight penalty results from the presence of air-leaks.

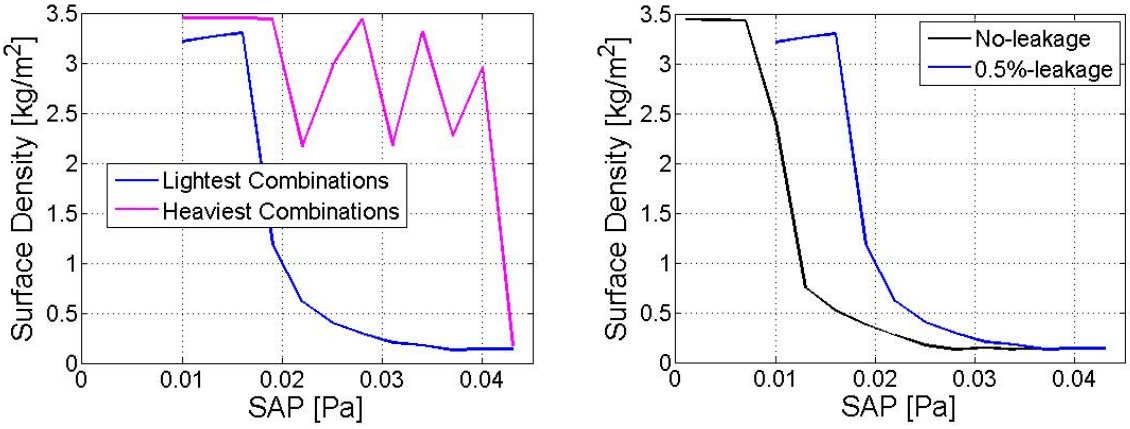

(a) (b)

Figure 5.4: *(a) Total surface density for various space-averaged pressures (r=0.005); (b) Lightest surface densities for no-leakage and 0.5 percent leakage cases.*

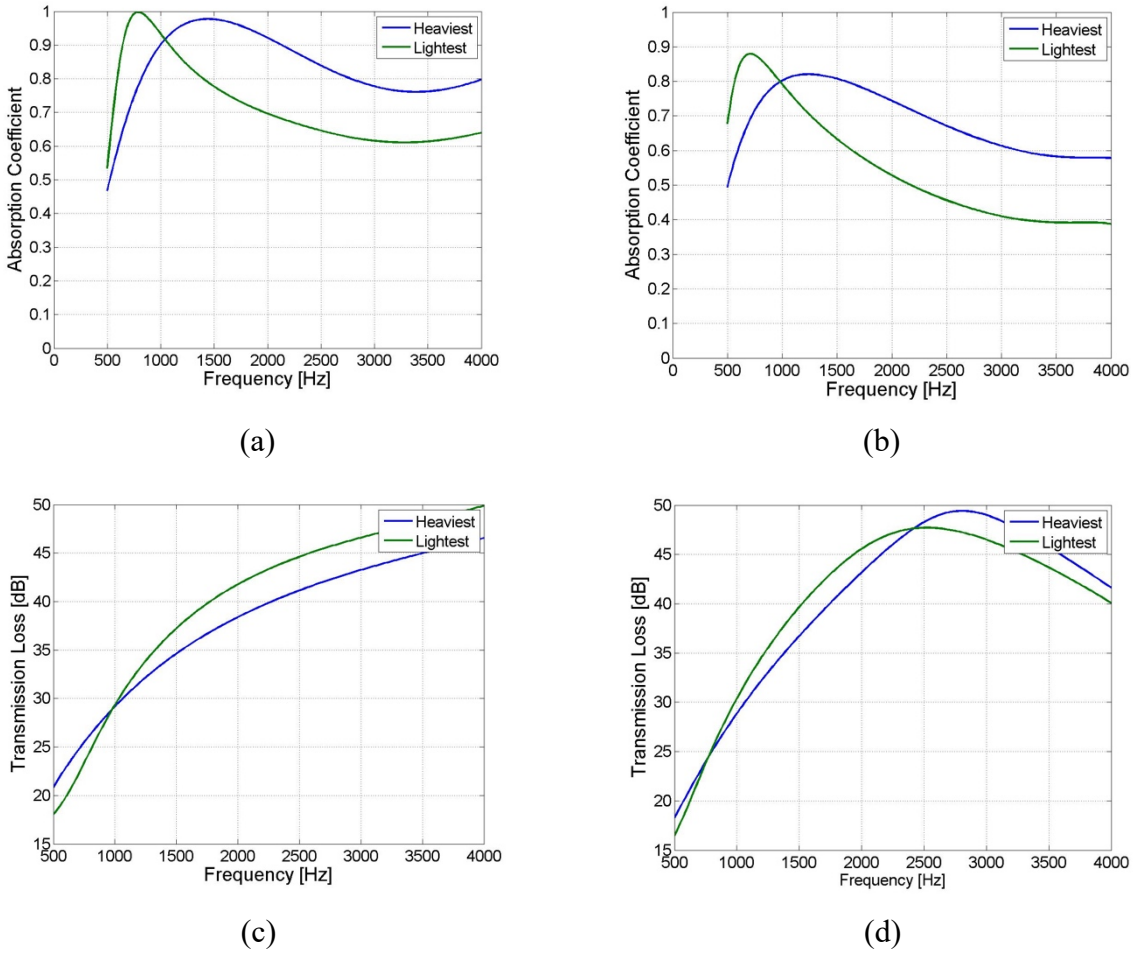

Figure 5.5: *Absorption coefficient and transmission loss for both (a), (c) No leakage (b), (d) 0.5 percent leakage when target space-averaged pressure was 0.022 Pa.*

When there was leakage in the sound package, the barrier performance of the sound package actually improved below 3 KHz, but was reduced at higher frequencies. In contrast, the absorption performance was generally reduced in the leakage case. That is, to compensate for the high frequency barrier performance loss due to the leakage, the optimized solutions for the 0.5 percent leakage case converged to a higher surface density as well as flow resistance, which resulted in comparable barrier performance to that of the no-leakage case, but which caused the relatively poor absorption performance. The acoustical properties of both the no-leakage and 0.5 percent leakage cases are listed in Table 5.2. From those values, it can be seen that the minimum surface density required to achieve a 0.022 Pa (60.8 dB) SAP more than doubled in the with-leak case. This result clearly demonstrates the major impact of leakage on sound package performance and weight efficiency. That conclusion is reinforced by the data summarized in Table 5.3 for

various SAP's. In all cases, the minimum surface density required to meet a target SAP more than doubles with even very minor leakage.

Table 5.2: The parameters of both no-leaks and 0.5 percent leaks cases for the optimized noise treatment when space averaged pressure was 0.022 Pa in the interior space.

Case	**Flexible MPP**	**Limp Porous Layer**	**Total**
No-leaks Lightest Combination	Flow Resistance [MKS Rayls] 1040.1	Flow Resistance [MKS Rayls] 1004.2	
	Surface Density [kg/m^2] 0.13	Surface Density [kg/m^2] 0.14	Surface Density [kg/m^2] 0.27
0.5% Leaks Lightest Combination	Flow Resistance [MKS Rayls] 1467.1	Flow Resistance [MKS Rayls] 1347.6	
	Surface Density [kg/m^2] 0.46	Surface Density [kg/m^2] 0.16	Surface Density [kg/m^2] 0.62

Table 5.3: The surface densities of both no-leaks and 0.5 percent leaks cases for various SAPs.

SAP [Pa]	No-leaks		0.5 percent leak	
	Lightest surface density [kg/m^2]	Heaviest surface density [kg/m^2]	Lightest surface density [kg/m^2]	Heaviest surface density [kg/m^2]
0.19	0.386	3.262	1.189	3.438
0.22	0.271	3.179	0.615	2.162
0.25	0.174	3.282	0.405	2.965

5.2 Heavier Rigid Panel Case

In general, automobile manufacturers favor the use of steel panels over aluminum panels, even though they are heavier, because of steel's better resistance to ding, dent and scratch. To make the current study more representative of present-day automotive applications, the aluminum panel was here replaced with a steel panel for the acoustic model being optimized. In that case, the density of the steel panel being used in the acoustic package model was 8700 kg/m^3, with a resultant surface density of 8.7 kg/m^2. The rest of the sound package was as before: i.e., a 3 cm layer of limp fibrous material topped with a flexible MPP layer, and in this case, leakage was not considered. The resulting surface density combinations from the optimization for the various targeted space-averaged pressures ranging from 1 X 10^{-3} Pa to 11 X 10^{-3} Pa are shown in Figure 5.6. That range of sound pressures represents interior sound levels going from 44 dB to 55 dB. The lowest possible SAP that can be obtained from this set up was 44 dB. Below 44 dB, the converged solutions could not meet the target SAP.

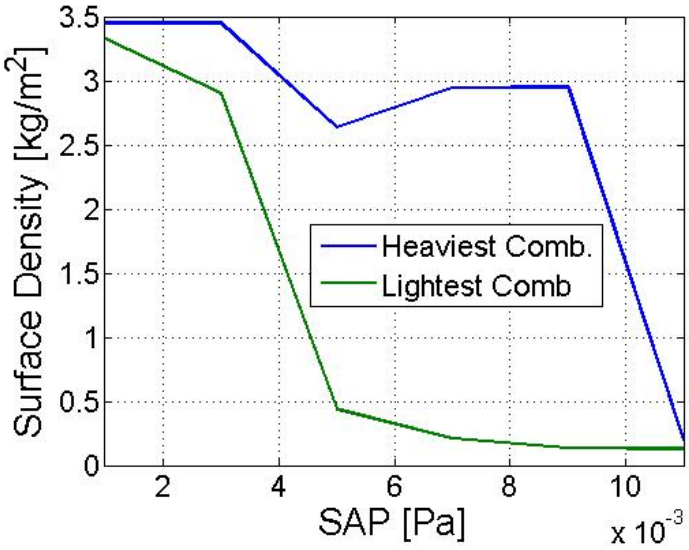

Figure 5.6: *Total surface density for various space-averaged pressures.*

First, it can be seen that a sound package with a heavier solid panel resulted in a broader space-averaged pressure range where possible weight minimization can occur. For the steel panel case, the solutions converged at a lower space-averaged pressure compared to the aluminum panel case since the transmission loss for a steel panel is higher than that of an aluminum panel of the same thickness. With the same acoustic properties for both flexible MPP and limp porous layer,

the sound package absorption coefficient does not change noticeably from the aluminum case, but the transmission performance showed a large increase when the aluminum panel was replaced by a steel panel, as can be seen in Figure 5.7.

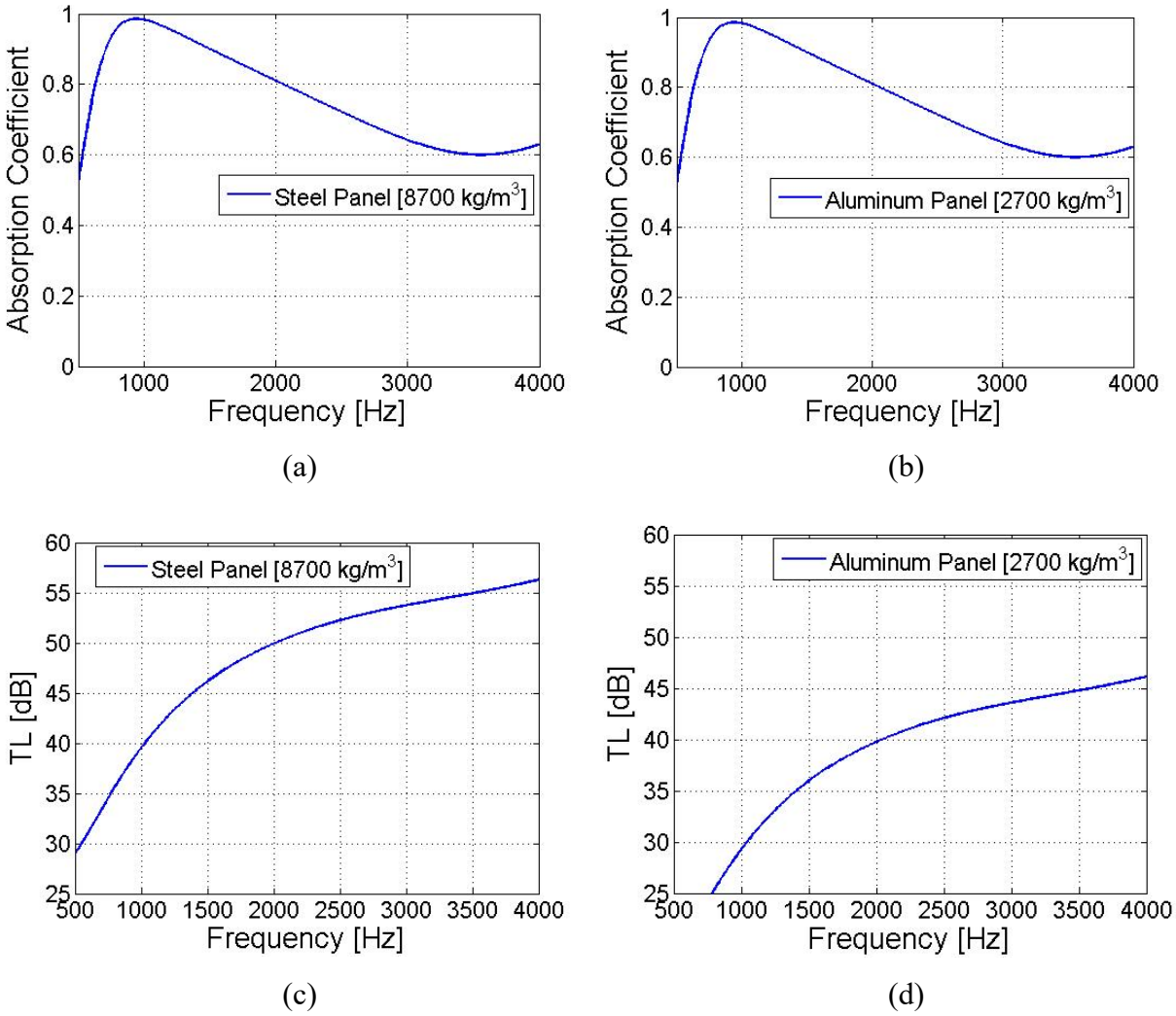

Figure 5.7: *Plots of acoustic performances for a steel panel (a) Absorption coefficient (c) Transmission loss, for an aluminum panel (b) Absorption coefficient (d) Transmission loss.*

In Table 5.4, the properties of the flexible MPP and the limp fibrous layer that were used to plot both the absorption coefficient and transmission for both the steel and aluminum panels are listed.

Table 5.4: The parameters of acoustic materials for both an aluminum panel and a steel panel cases.

Case	Flexible MPP	Limp Porous Layer	Total
Aluminum/ Steel Rigid Panel	Flow Resistance [MKS Rayls] 762.2	Flow Resistance [MKS Rayls] 1493	
	Surface Density [kg/m^2] 0.16	Surface Density [kg/m^2] 0.05	Surface Density [kg/m^2] 0.21

The results for both the steel and aluminum panels are summarized in Tables 5.5(a) and 5.5(b), respectively. In the steel case, it can be seen that for all the "lightest" cases, most of the surface density is given to MPP, and the same is true of the flow resistance at small space-averaged pressures. Thus, at low levels, the optimization is trying to emphasize barrier performance. But, as the target level increases, the MPP flow resistance drops while that of the fibrous layer increases, thus improving the absorption performance. This behavior contrasts with that of the aluminum case, in which case the MPP flow resistance and surface density are always greater that the corresponding values for the fibrous layer.

Table 5.5(a): The surface densities and flow resistance for the steel panel case for various SAPs.

SAP [Pa]	MPP		Limp Porous		Total
	Surface Density (kg/m^2)	**Flow Resistance (MKS Rayls)**	**Surface Density (kg/m^2)**	**Flow Resistance (MKS Rayls)**	**Surface Density (kg/m^2)**
0.003	2.456	1496.1	0.448	1401.2	2.904 (Lightest)
	3.000	1309.1	0.450	1348.1	3.450 (Heaviest)
0.005	0.306	1434.9	0.132	1352.7	0.438 (Lightest)
	2.202	746.6	0.431	247.9	2.633 (Heaviest)
0.007	0.163	762.2	0.047	1493.0	0.210 (Lightest)
	2.689	161.5	0.257	1160.9	2.946 (Heaviest)
0.009	0.100	217.7	0.034	1481.8	0.134 (Lightest)
	2.888	121.8	0.062	989.7	2.950 (Heaviest)
0.011	0.100	100.0	0.030	1420.8	0.130 (Lightest)
	0.163	100.0	0.031	100.1	0.194 (Heaviest)

Table 5.5(b): The surface densities and flow resistance for the aluminum panel case for various SAPs.

SAP [Pa]	MPP		Limp Porous		Total
	Surface Density (kg/m^2)	Flow Resistance (MKS Rayls)	Surface Density (kg/m^2)	Flow Resistance (MKS Rayls)	Surface Density (kg/m^2)
0.011	1.987	1485.1	0.427	1463	2.414 (Lightest)
	2.907	1442.2	0.2337	829.5	3.450 (Heaviest)
0.013	0.446	1397.3	0.2889	1178.1	0.755 (Lightest)
	2.907	1179.0	0.2337	829.5	3.141 (Heaviest)
0.016	0.3299	1420.2	0.1927	373.1	0.523 (Lightest)
	2.924	780.7	0.3924	258.3	3.317 (Heaviest)
0.019	0.311	864.2	0.0752	102.6	0.386 (Lightest)
	2.923	503.7	0.339	310.9	3.262 (Heaviest)
0.022	0.133	1040.1	0.139	1004.2	0.272 (Lightest)
	2.995	317.9	0.185	590.4	3.180 (Heaviest)
0.025	0.104	730.1	0.071	343.7	0.175 (Lightest)
	2.960	137.4	0.322	474.0	3.282 (Heaviest)
0.028	0.100	261.5	0.032	100.0	0.132 (Lightest)
	2.961	124.4	0.155	124.6	3.116 (Heaviest)

It can also be seen that the optimized solutions for the steel panel case generally required a higher flow resistance of the limp porous layer compared to the aluminum panel case. Also, the steel panel case yielded a wider possible optimization range of SAPs than did the relatively lighter aluminum panel. To reach the same target SAP for both the steel and aluminum panel cases, the aluminum case only required a total surface density of 5.11 kg/m^2, but the steel case required 8.83 kg/m^2. Thus, a weight optimized sound package with a relatively light rigid panel can give

comparable acoustic performance to that of a heavier rigid panel. However, further work should be conducted with steel panels to clearly identify systematic differences from the aluminum case.

5.3 High Termination Impedance Case

All of the previous cases have been run with the same air space termination impedance, $11.25\rho c$, giving an absorption coefficient of 0.3. A change in the impedance, and hence the average absorption in the interior space could change the required balance between absorption and transmission loss required to achieve a specified SAP. That effect will be considered in this section.

In order to see the effect of the interior absorptivity of the cabin on the weight resulting from the sound package optimization, the calculation of the aluminum, no leakage case was repeated with a higher termination impedance, $22.5\rho c$, which corresponds to an absorption coefficient of 0.16. The surface density results obtained from the optimization are shown in Figure 5.8.

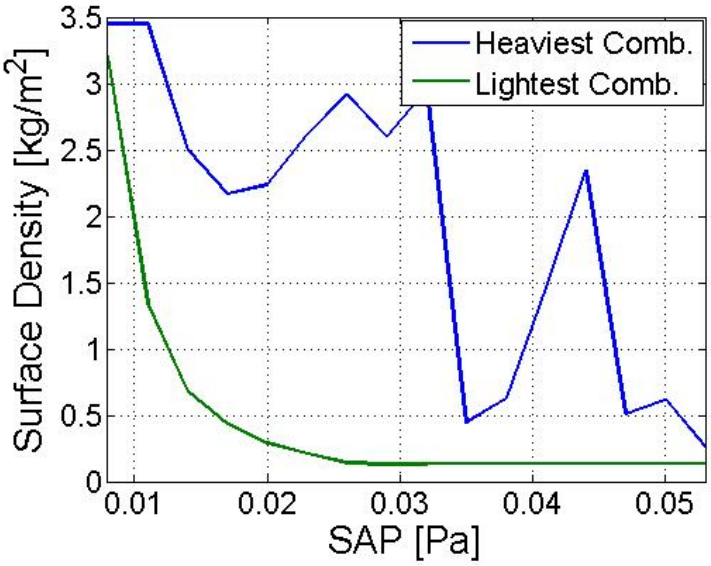

Figure 5.8: *Total surface density for various space-averaged pressures for higher termination impedance.*

To illustrate the optimization results obtained in this case, absorption coefficients and the transmission losses are plotted in the Figure 5.9. To achieve the 0.026 Pa space-averaged pressure for the termination impedance of $22.5\rho c$, the total surface density was actually reduced by 21 percent compared to the case when the termination impedance was $11.25\rho c$, even though this case would appear to be more difficult because of the reduced interior absorption. When comparing the

lightest solutions, the absorption was reduced in the 22.5 ρc case compared to the 11.25 ρc, while the transmission loss increased.

Once again, this seems to emphasize that good barrier performance is preferred to good absorption performance in the lightest cases, and with lighter base panels (i.e., aluminum versus steel). And further, as can be seen from Table 5.6, the majority of both the mass and flow resistance are given to the MPP rather than to the fibrous layer.

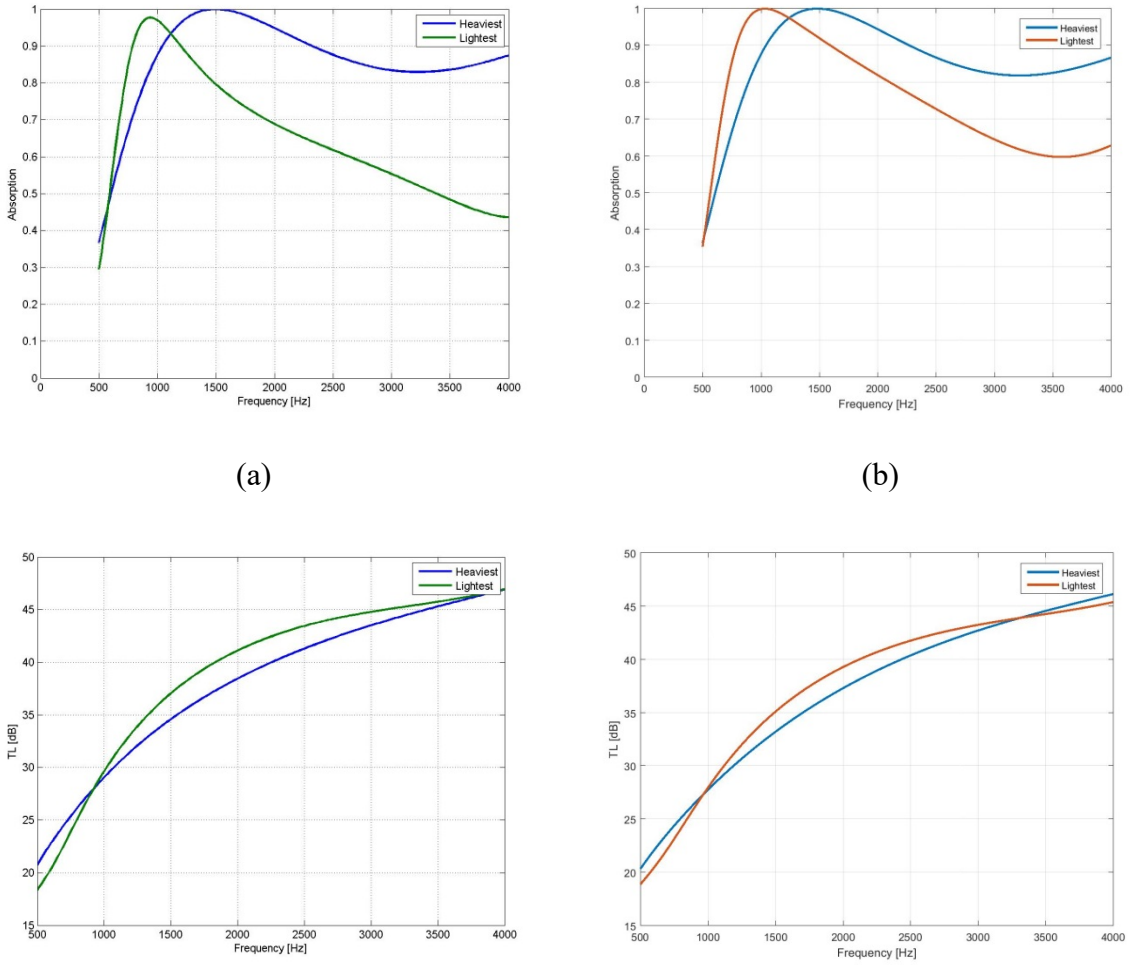

Figure 5.9: *Plots of acoustic performances for (a), (c) Termination impedance of 22.5 ρc, (b), (d) Termination impedance of 11.25 ρc when space-averaged pressure is 0.026 Pa.*

Table 5.6: The parameters of the sound package obtained from two different termination impedance cases when space averaged pressure was 0.026 Pa in the interior space.

Case	Flexible MPP	Limp Porous Layer	Total
Lightest Combination Term. impedance (11.25 ρc)	Flow Resistance [MKS Rayls] 730.1	Flow Resistance [MKS Rayls] 343.7	
	Surface Density [kg/m^2] 0.10	Surface Density [kg/m^2] 0.07	Surface Density [kg/m^2] 0.17
Lightest Combination Term. impedance (22.5 ρc)	Flow Resistance [MKS Rayls] 1339.7	Flow Resistance [MKS Rayls] 119.3	
	Surface Density [kg/m^2] 0.11	Surface Density [kg/m^2] 0.03	Surface Density [kg/m^2] 0.14

5.4 A-Weighted SAP Case

In previous optimization cases, the weight optimization of the sound package was performed with the objective of meeting a specified SAP averaged over the frequency range from 500 Hz to 4000 Hz, which is the speech interference range. In the work described in this section, the optimization process remained the same as in previous cases, but different frequency weightings are considered in the optimization. The objective here was to illustrate the impact of different frequency weighting on the minimum weight solutions.

In the first case, the A-weighing, designed to emphasize the high frequency region, and which mimics the frequency response of the human hearing system, was used so that the results from the optimization would be more applicable to perceived loudness. The frequency spectrum of A-

weighting function and its acoustical effect on the space-averaged pressures are demonstrated in Figure 5.10.

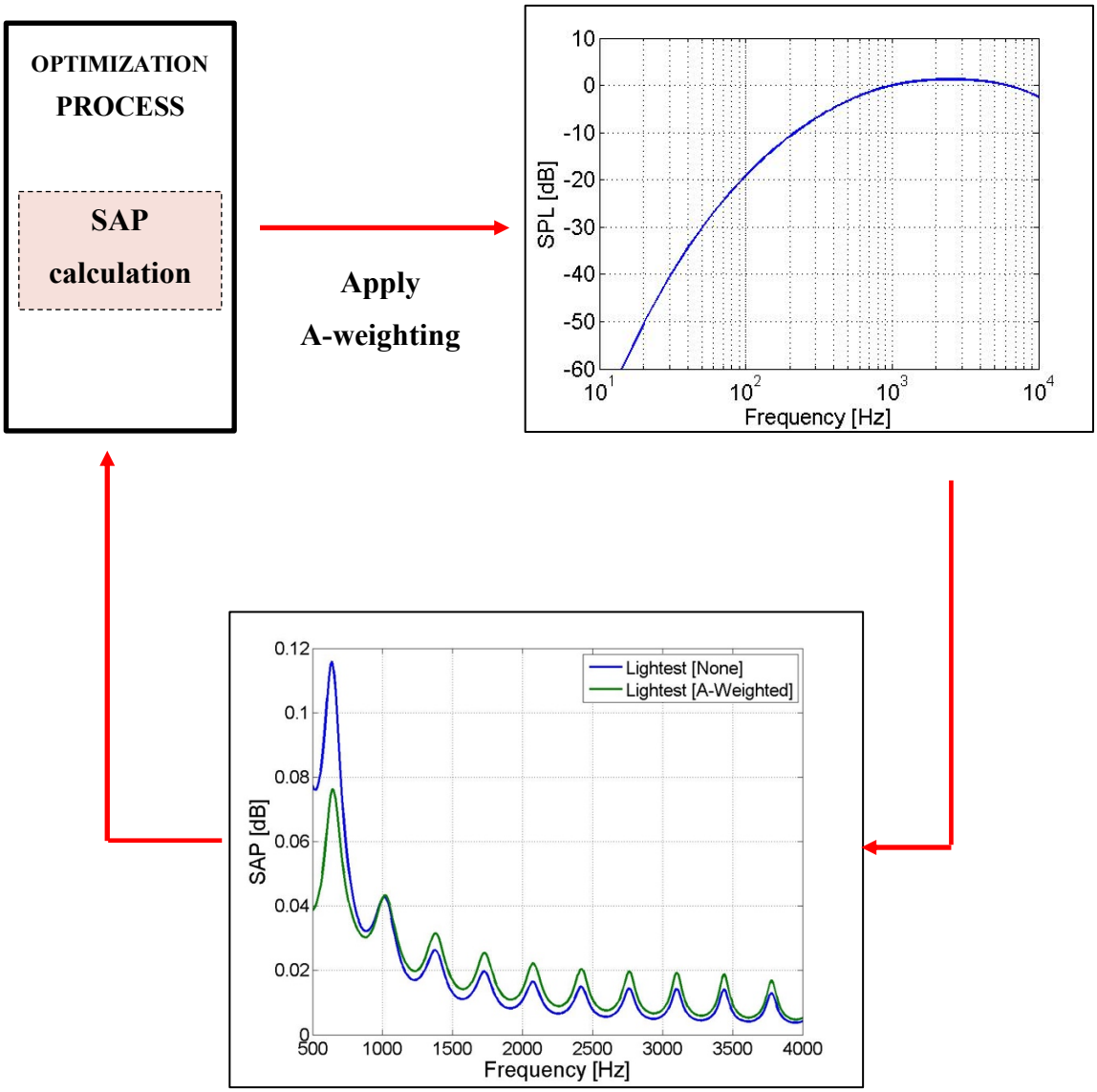

Figure 5.10: *The schematic of an optimization with an A-weighted function in the process.*

The A-weighting function was applied at the stage where the space-averaged pressure was calculated. It can be seen that the A-weighting function de-emphasizes the very low frequency components in the SAP. The optimization was ran for 50 different times in the A-weighted space-averaged pressure range between 0.007 Pa (50.9 dB) to 0.034 Pa (64.6 dB). The resulting surface density combinations are plotted in Figure 5.11.

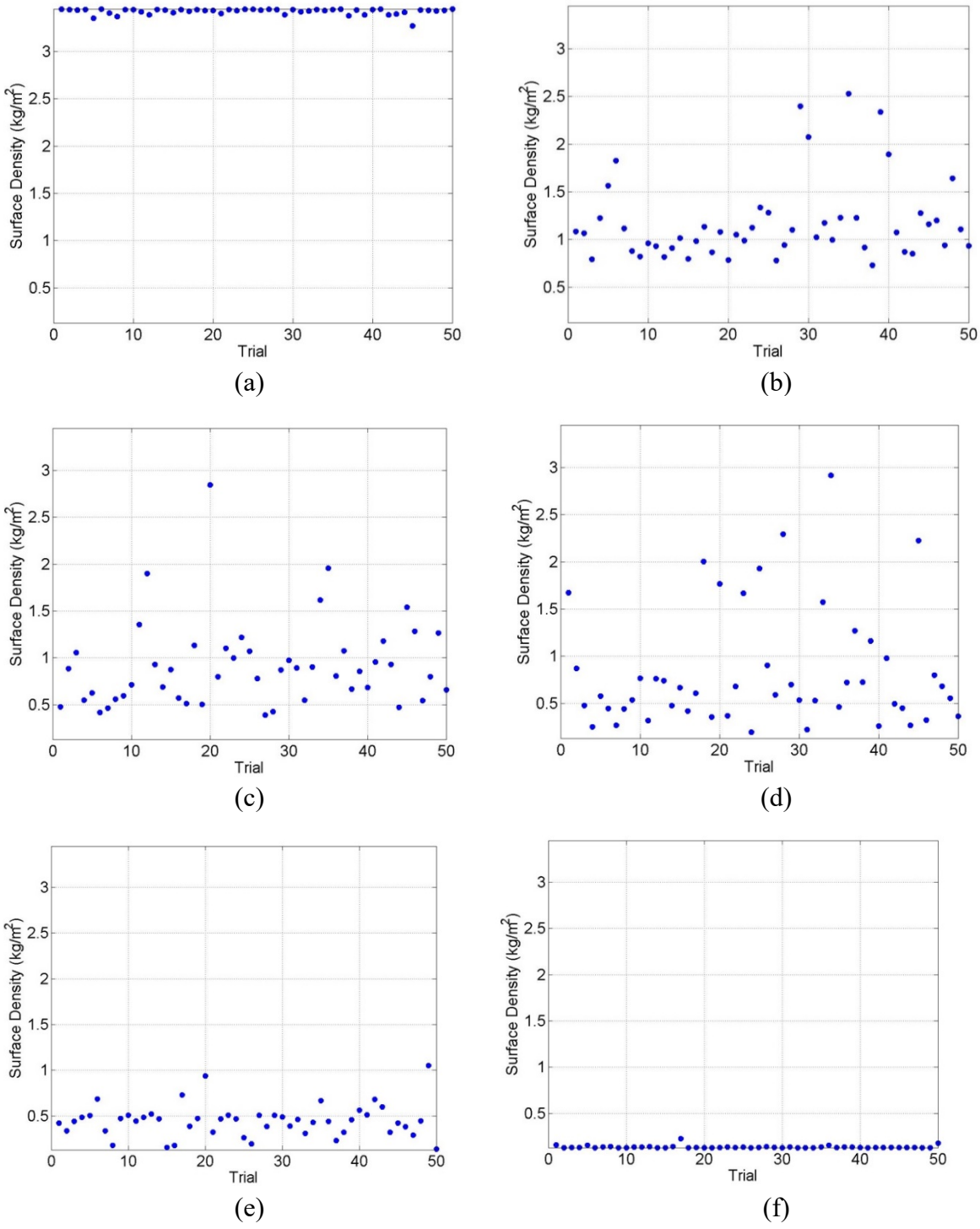

Figure 5.11: *Plots of various total surface densities that gave the targeted space-averaged pressure magnitude of (a) 0.007 Pa (b) 0.013 Pa (c) 0.019 Pa (d) 0.022 Pa (e) 0.031 Pa (f) 0.034 Pa.*

The lightest and heaviest optimized total surface densities for the A-weighting case for various space-averaged pressures are plotted in the Figure 5.12.

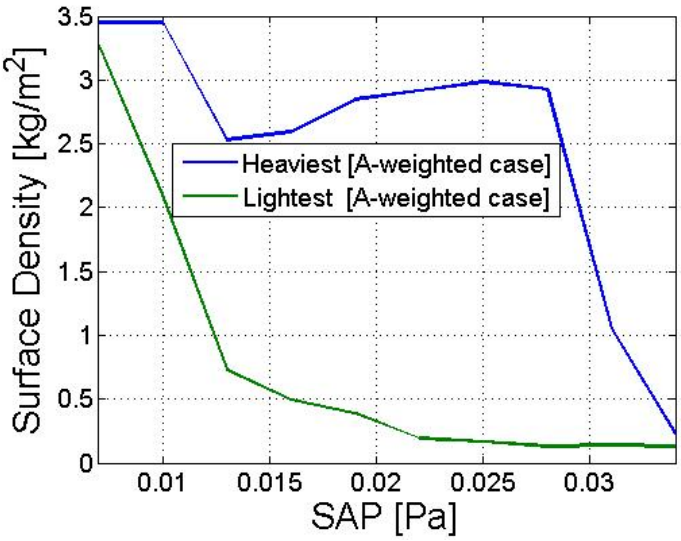

Figure 5.12: *Plots of total surface density with respect to various space-averaged pressures.*

Figure 5.13 shows the comparison between the A-weighted and the non-weighted case for the various space-averaged pressures.

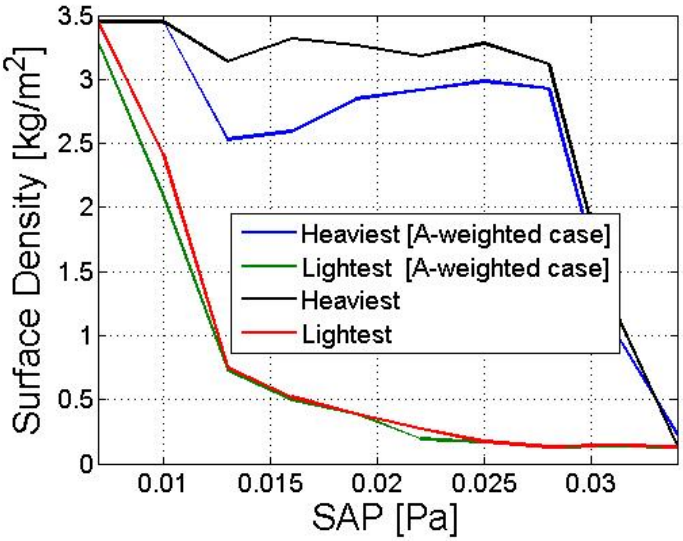

Figure 5.13: *Plots of total surface density with respect to various space-averaged pressures. Possible heaviest surface density combinations for the A-weighted class (Blue), possible lightest surface density combinations for the A-weighted case (Green), possible heaviest surface density combinations for the no-weighted case (Black), possible lightest surface density combinations for the no-weighted case (red).*

It can be seen that the possible surface density combinations for the A-weighted case are generally lower than those for the no-weighted case for both the lightest and heaviest surface density combination results, but the weight difference is more noticeable in the heaviest surface density combinations. The reason for this is that the optimizer does not have much freedom to reduce the surface density values further. The comparison of absorption and transmission performance for those cases will be demonstrated in the next section.

5.4.1 Absorption and Transmission Performance Analysis

It was observed that when the A-weighting function was applied in the optimization process, the surface density combinations tended to have lower values than in the no-weighting case. The A-weighting function naturally emphasizes the absorption and the barrier performance of the sound packages at higher frequency (above 1000 Hz). Therefore, the surface density that was required to yield a certain level of barrier performance at lower frequencies (say, below 1000 Hz) was reduced compared to the cases described in earlier chapters. Both the absorption and the transmission loss of the optimized sound packages for both the lightest possible and the heaviest possible combinations that gave the space-averaged pressure of 0.019 Pa (59.55 dB) are plotted and compared in Figure 5.14, and the space-averaged pressures are plotted in Figure 5.15.

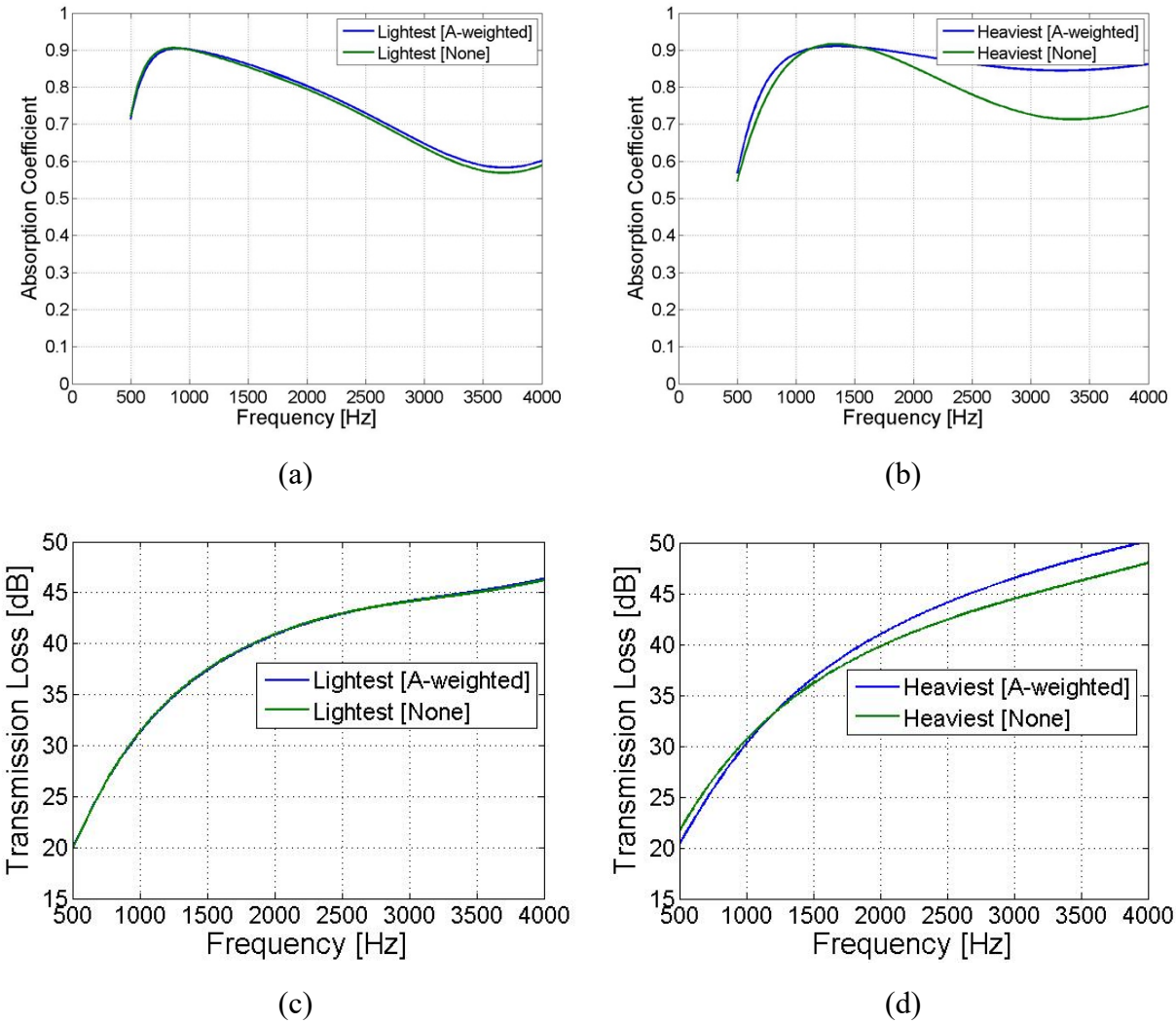

Figure 5.14: *Plots of absorption coefficient for (a) lightest (c) heaviest solutions, and transmission loss for (c) lightest (d) heaviest solutions for both the A-weighted and no-weighting cases.*

For the lightest possible surface density cases, there is not much difference between the A-weighted and no-weight case. However, for the heaviest possible surface density cases, there is a noticeable difference between the A-weighted and the no-weighting optimization results. Note that the A-weighted optimization emphasized the barrier performance above 1000 Hz in order to reduce the space-averaged pressure above 1000 Hz. The material properties resulting from the optimization are listed in Table 5.7.

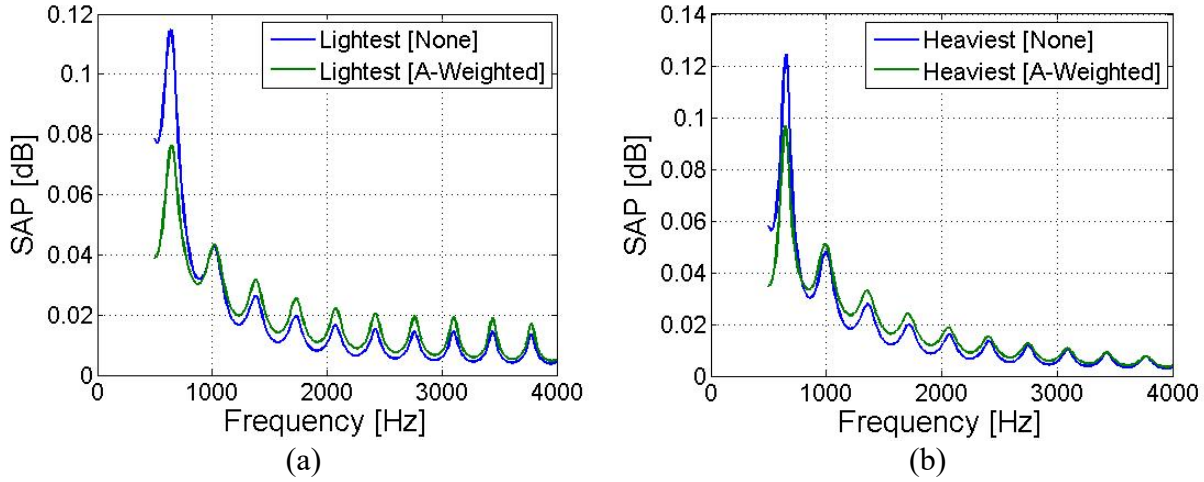

Figure 5.15: *The space-averaged pressure of 0.019Pa for both the lowest (a) and the highest surface density (b).*

Table 5.7: The acoustic parameters for both the A-weighting and the no-weighting cases for various SAPs.

SAP [Pa]	MPP		Limp Porous		Total
	Surface Density (kg/m^2)	**Flow Resistance (MKS Rayls)**	**Surface Density (kg/m^2)**	**Flow Resistance (MKS Rayls)**	**Surface Density (kg/m^2)**
0.019 (No-weighting)	0.311	864.2	0.075	102.6	0.386 (Lightest)
	2.923	503.7	0.339	310.9	3.262 (Heaviest)
0.019 (A-weighting)	0.315	829.4	0.074	450.1	0.389 (Lightest)
	2.445	257.0	0.401	1295.8	2.846 (Heaviest)
0.022 (No-weighting)	0.133	1040.1	0.139	1004.2	0.272 (Lightest)
	2.995	317.9	0.185	590.4	3.180 (Heaviest)
0.022 (A-weighting)	0.159	1053.3	0.037	288.2	0.344 (Lightest)
	2.693	220.2	0.224	1280.5	2.917 (Heaviest)
0.025 (No-weighting)	0.104	730.1	0.071	343.7	0.175 (Lightest)
	2.960	137.4	0.322	474.0	3.282 (Heaviest)
0.025 (A-weighting)	0.103	781.7	0.063	1052.5	0.166 (Lightest)
	2.790	140.4	0.194	809.8	2.984 (Heaviest)

The noticeable material property difference between the A-weighted and no-weighting cases is that the optimizer gave relatively high flow resistances to the limp porous layer for the A-weighted optimization case for the heaviest possible surface density combinations. It is noted that in the A-weighted case, the limp porous layer was given almost almost twice the flow resistance as in the no-weighting space-averaged optimization case. Another significant result for the A-weighted optimization was that the flexible MPP now was given lighter surface densities than in the no-weighting case. From the optimization results, it can be concluded that when higher frequency components are emphasized in the optimization process, the optimizer tend to reduce the mass barrier performance of the flexible MPP, so that the absorption performance is improved.

5.5 Octave Frequency Bands

Another approach to weighting the objective function would be to average over octave bands, which in contrast to the A-weighting tends to emphasize the low frequency end of the spectrum. The latter follows since a relatively narrow band of low frequencies is given the same weight as a much broader range of higher frequencies. So, here, the SAP calculation was performed by numerically averaging octave band levels. In order to perform the weight optimization in the octave bands, SAPs that were first calculated on a linear scale needed to be converted to octave band level scale. Table 5.8 lists the octave frequency bands that were used for the linear-to-octave bands conversion. Each octave band is defined by

$$\text{Middle Frequency: } f_o, \text{ Lower Frequency: } f_o/f_o^{1/2}, \text{ Upper Frequency: } f_o \times f_o^{1/2}. \quad (47)$$

Once the octave bands are defined, each pressure value on the linear scale that falls within corresponding octave band was collected. Then, the total acoustic pressure in each band was calculated as,

$$\text{Total pressure in each band: } \sqrt{\sum_1^N (P_{rms,i})^2}. \quad (48)$$

where $P_{rms,i}$ denotes the individual root-mean-square pressure values that falls within each octave band, and where *N* denotes the total number of individual pressures that fall into a specific octave band.

Table 5.8: Lower, middle, and upper octave bands

Lower Frequency [Hz]	Middle Frequency [Hz]	Upper Frequency [Hz]
353.6	**500**	**707.1**
707.1	**1000**	**1414.2**
1414.2	**2000**	**2828.4**
2828.4	**4000**	**5656.9**

Then the sound pressures in the four bands was averaged arithmetically to yield the octave-based Speech Interference Level. The total Speech Interference Level was then calculated as

$$\frac{L_1+L_2+L_3+L_4}{N},\ N=4 \tag{49}$$

where L_1, L_2, L_3, and L_4denote the total pressures in the 500 Hz, 1000 Hz, 2000 Hz, and 4000 Hz bands, respectively. The Speech Interference Level calculation method was then implemented in the optimizer to perform the weight optimization as shown in Figure 5.16.

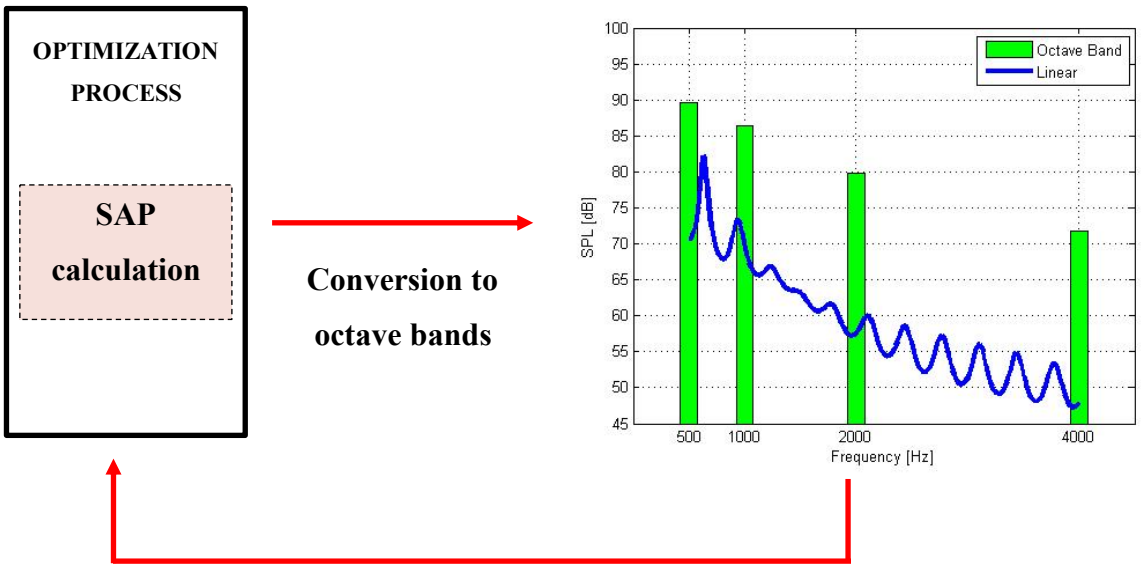

Figure 5.16: *The schematic of an optimization in octave bands.*

The optimization was run 50 different times in the space-averaged pressure range between 0.007 Pa (50.88 dB) to 0.023 Pa (61.21 dB). The resulting surface density combinations are plotted in Figure 5.17.

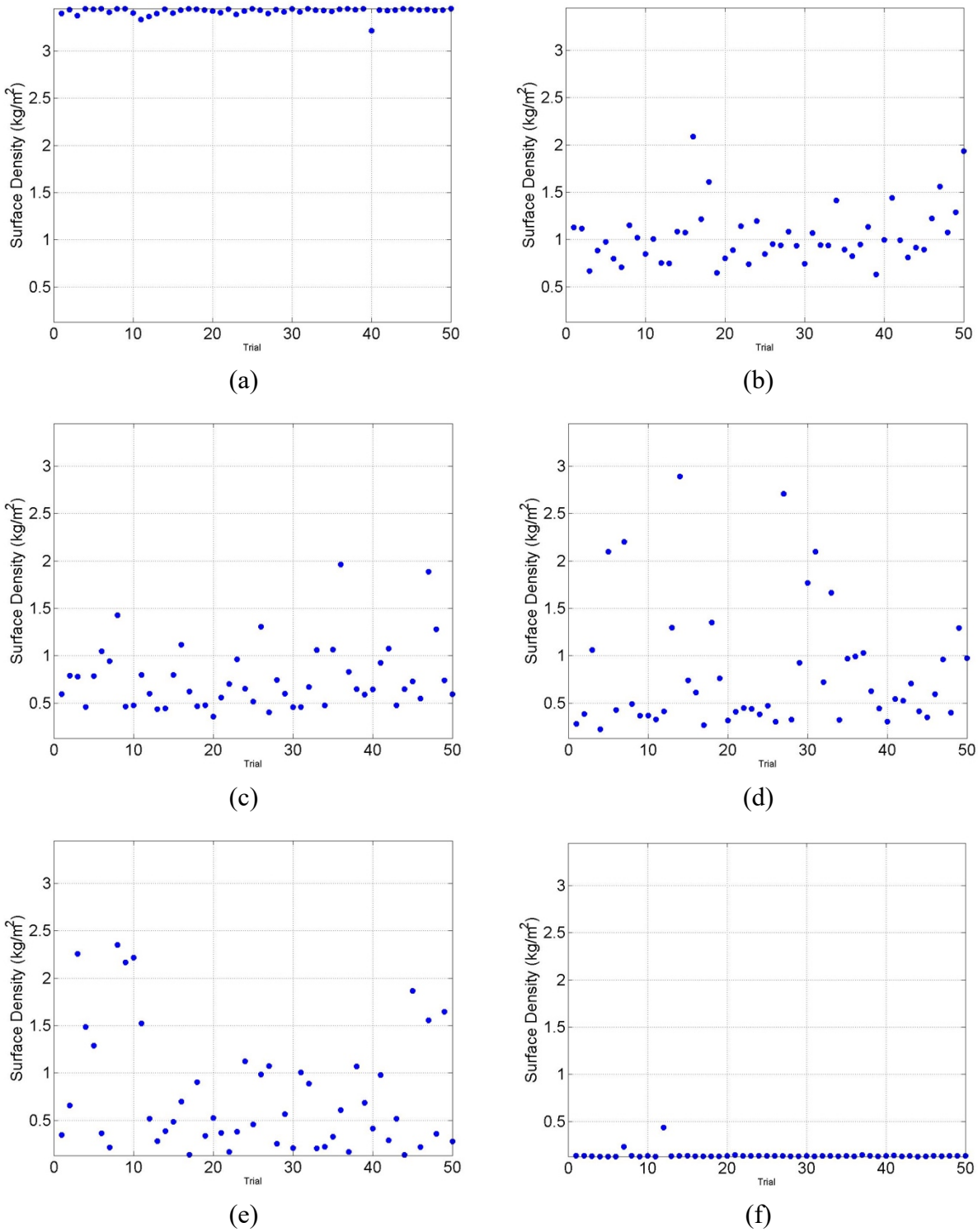

Figure 5.17: *Plots of various total surface densities that gave the targeted space-averaged pressure magnitude of (a) 0.007 Pa (b) 0.010 Pa (c) 0.013 Pa (d) 0.016 Pa (e) 0.019 Pa (f) 0.022 Pa.*

The maximum and minimum weight optimized total surface densities for the octave band (Speech Interference Level) case for various SAP targets are plotted in Figure 5.18.

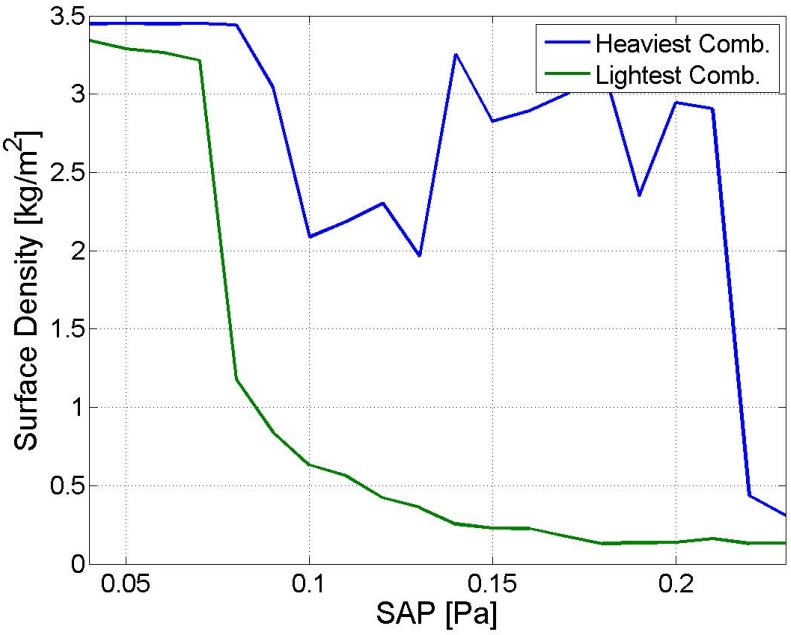

Figure 5.18: *Plots of total surface density with respect to various space-averaged pressures.*

5.5.1 Absorption and Transmission Performance Analysis

It was noted that when octave bands were used in the optimization process, the surface density combinations tend to become lighter than in the non-weighted optimization case. The absorption and the transmission loss performance of the weight optimized sound packages for both the lightest possible and the heaviest possible combinations that gave the space-averaged pressure of 0.019 Pa (59.6 dB) are plotted and compared in Figure 5.19, and the corresponding space-averaged pressures are plotted in Figure 5.20.

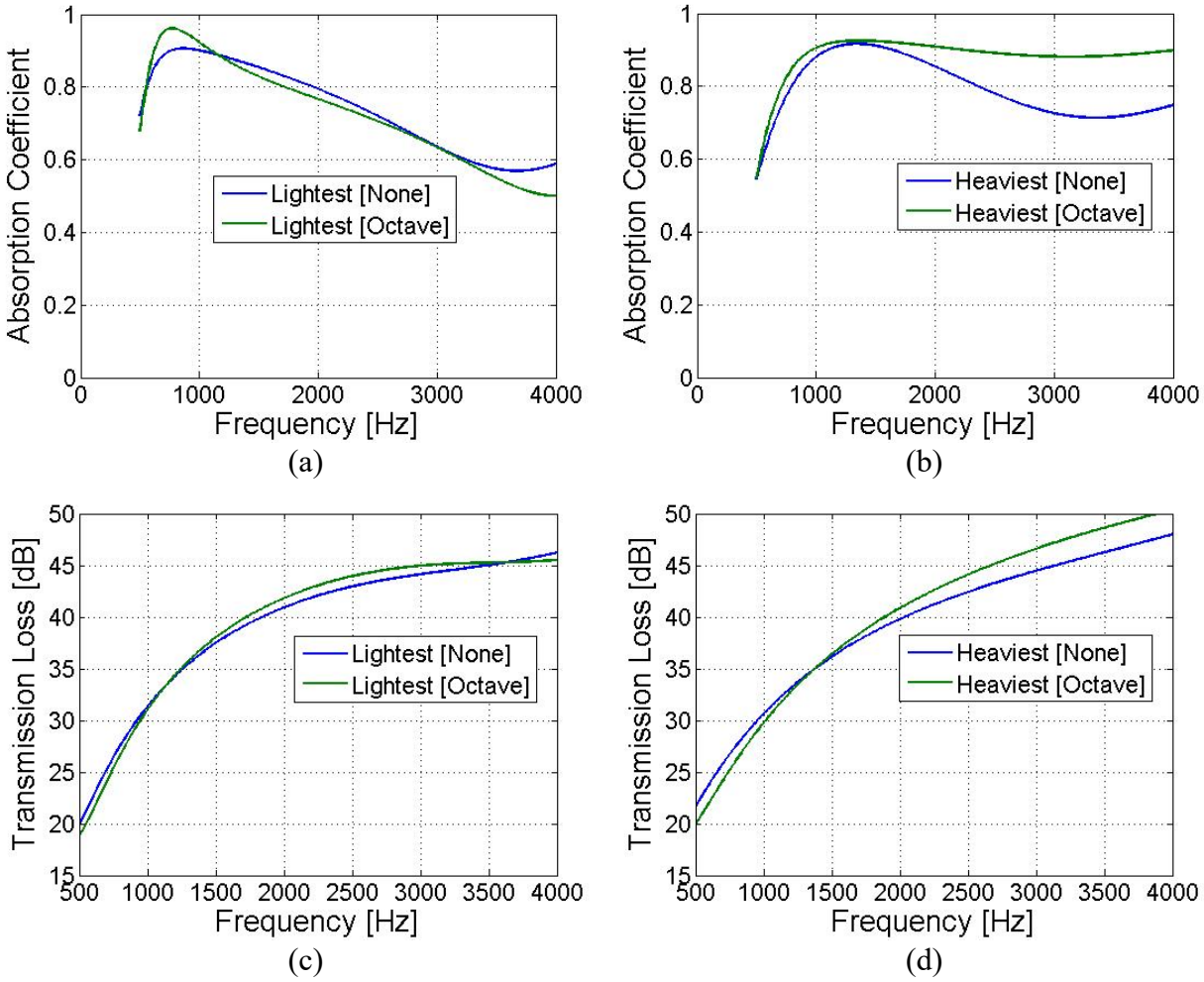

Figure 5.19: *Plots of absorption coefficient (a) lightest (b) heaviest solutions, and transmission loss(c) lightest (d) heaviest solutions for both the Octave band and no-weighting cases.*

There is not a very significant difference between the two weighting results in the case of the lightest solutions, although the octave weighting tends to result in a slightly higher transmission loss: i.e., barrier performance is emphasized.

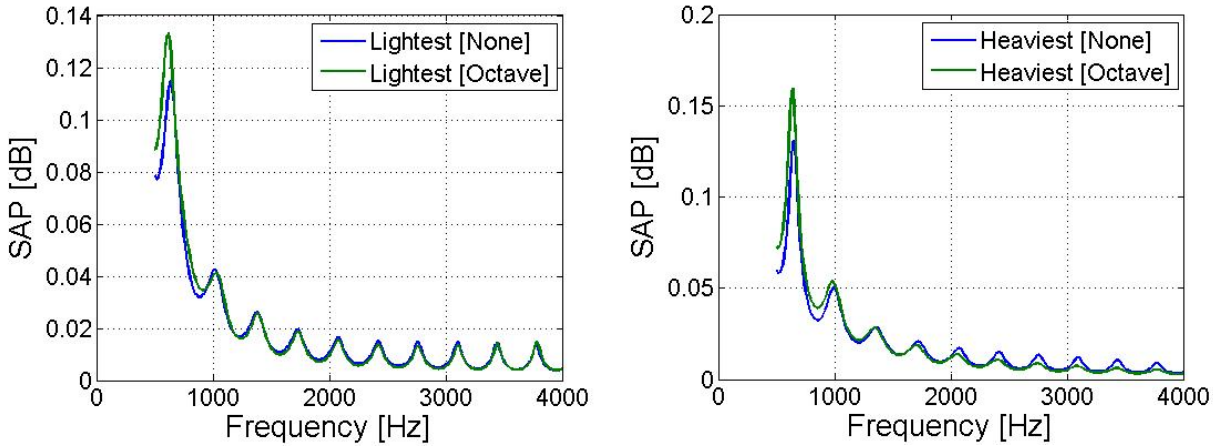

(a) (b)

Figure 5.20: *The space-averaged pressure of 0.019Pa for both the lowest (a) and the highest surface density (b).*

The material properties of the sound packages obtained from the optimization are listed in Table 5.9.

Table 5.9: The material properties for both the Octave band and the no-weighting cases for various SAPs.

SAP [Pa]	MPP		Limp Porous		Total
	Surface Density (kg/m^2)	Flow Resistance (MKS Rayls)	Surface Density (kg/m^2)	Flow Resistance (MKS Rayls)	Surface Density (kg/m^2)
0.019 (No-weighting)	0.311	864.2	0.075	102.6	0.386 (Lightest)
	2.923	503.7	0.339	310.9	3.262 (Heaviest)
0.019 (Octave Band)	0.269	1455.2	0.089	759.9	0.359 (Lightest)
	1.658	390.1	0.305	846.9	1.963 (Heaviest)
0.022 (No-weighting)	0.133	1040.1	0.139	1004.2	0.272 (Lightest)
	2.995	317.9	0.185	590.4	3.180 (Heaviest)
0.022 (Octave Band)	0.190	1226.1	0.038	100.0	0.228 (Lightest)
	2.677	359.1	0.146	103.8	2.823 (Heaviest)
0.025 (No-weighting)	0.104	730.1	0.071	343.7	0.175 (Lightest)
	2.960	137.4	0.322	474.0	3.282 (Heaviest)
0.025 (Octave Band)	0.128	544.8	0.047	1282.2	0.175 (Lightest)
	2.762	123.4	0.235	803.6	2.987 (Heaviest)

5.6 Comparison

In order to summarize the effect of the different SAP frequency weightings on the weight optimization results, both the lightest and the heaviest optimization results based on octave band, A-weighted, and no-weighting SAP calculation for various SAPs are plotted in Figures 5.21 and 5.22, respectively.

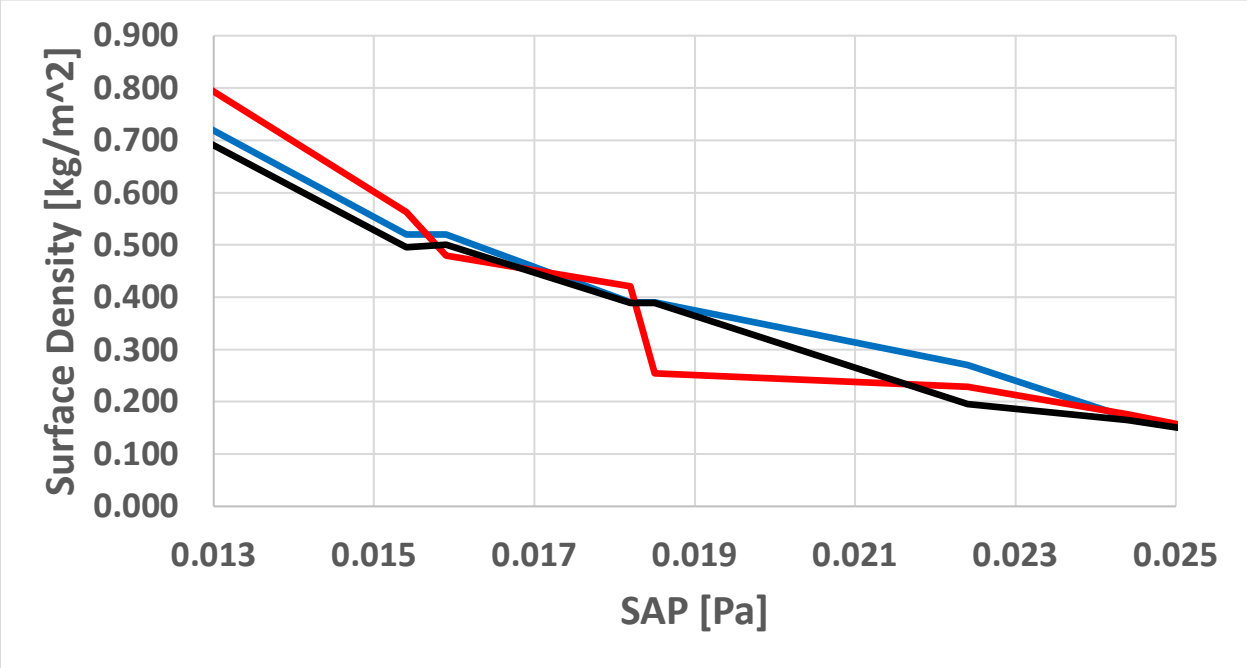

Figure 5.21: *The lightest possible solutions for various SAPs. (Red: Octave band, Blue: Linear, Black: A-weighting)*

It can be seen that there is not much difference between the cases for the lightest surface density combinations, but it was found that the A-weighting (black), and linear (blue) cases gave slightly lower surface densities than that of the octave-band (red) case in the low-target SAP range. In the octave band case, the low frequency range is emphasized slightly in the optimization, and so larger surface densities are required to achieve a specified SAP.

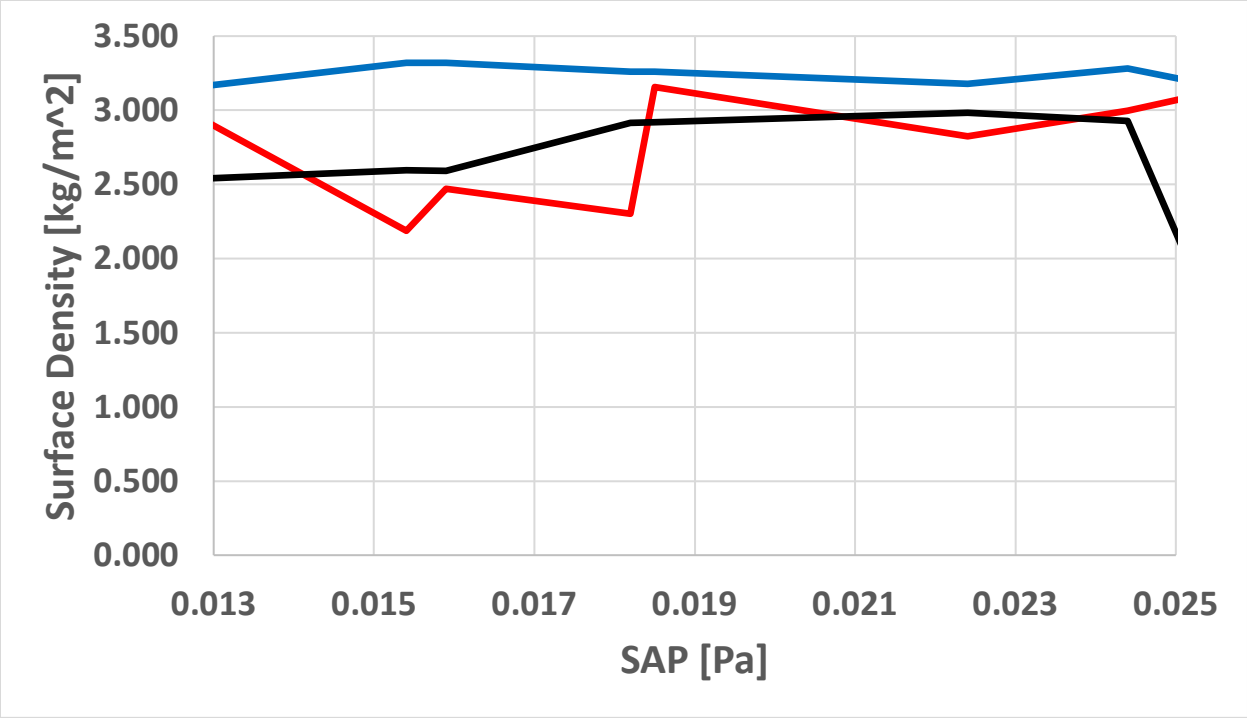

Figure 5.22: *The heaviest possible solutions for various SAPs. (red: Octave band, Blue: Linear, Black: A-weighting)*

In contrast, for the heaviest combinations, it is clear to see that the octave band case (red) and A-weighting (blue) case tend to give lower surface densities than no-weighting case.

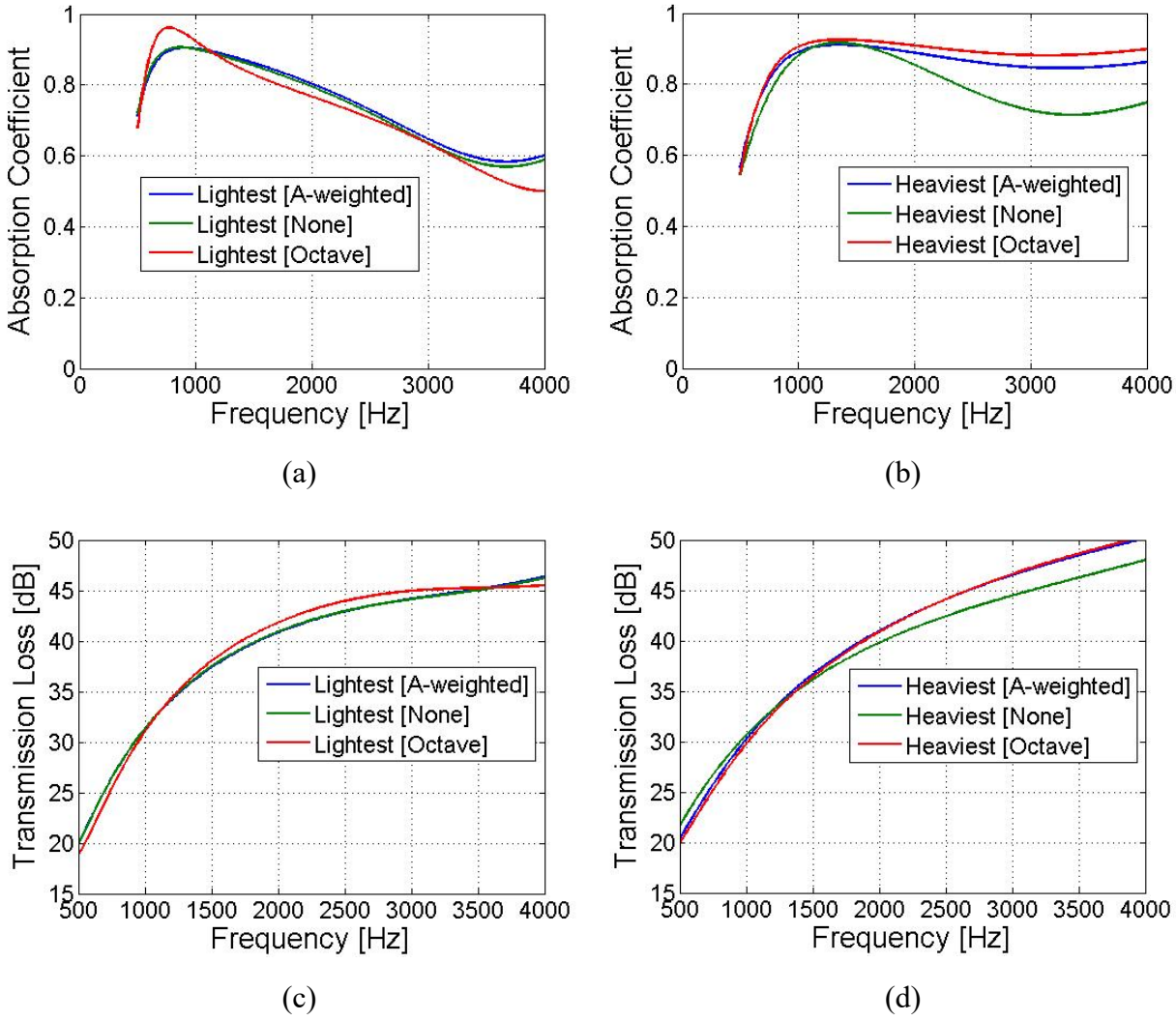

Figure 5.23: *Plots of absorption coefficient and transmission loss for the A-weighted, Octave band, and no-weighted cases. Absorption coefficient for the (a) lightest and (b) heaviest combinations. Transmission loss for the (c) lightest and (d) heaviest combinations.*

A comparison of the absorption coefficient and transmission loss for the various cases is presented in Figure 5.23, and the material properties of the lowest and highest surface densities for three different cases are listed in Table 5.10.

‘

Table 5.10: The material properties for both the Octave band and the no-weighting cases for various SAPs.

SAP [Pa]	MPP		Limp Porous		Total
	Surface Density (kg/m^2)	Flow Resistance (MKS Rayls)	Surface Density (kg/m^2)	Flow Resistance (MKS Rayls)	Surface Density (kg/m^2)
0.019 (No-weighting)	0.311	864.2	0.075	102.6	0.386 (Lightest)
	2.923	503.7	0.339	310.9	3.262 (Heaviest)
0.019 (Octave Band)	0.269	1455.2	0.089	759.9	0.359 (Lightest)
	1.658	390.1	0.305	846.9	1.963 (Heaviest)
0.019 (A-weighting)	0.315	829.4	0.074	450.1	0.389 (Lightest)
	2.445	257.0	0.401	1295.8	2.846 (Heaviest)
0.022 (No-weighting)	0.133	1040.1	0.139	1004.2	0.272 (Lightest)
	2.995	317.9	0.185	590.4	3.180 (Heaviest)
0.022 (Octave Band)	0.190	1226.1	0.038	100.0	0.228 (Lightest)
	2.677	359.1	0.146	103.8	2.823 (Heaviest)
0.019 (A-weighting)	0.159	1053.3	0.037	288.2	0.344 (Lightest)
	2.693	220.2	0.224	1280.5	2.917 (Heaviest)
0.025 (No-weighting)	0.104	730.1	0.071	343.7	0.175 (Lightest)
	2.960	137.4	0.322	474.0	3.282 (Heaviest)
0.025 (Octave Band)	0.128	544.8	0.047	1282.2	0.175 (Lightest)
	2.762	123.4	0.235	803.6	2.987 (Heaviest)
0.025 (A-weighting)	0.103	781.7	0.063	1052.5	0.166 (Lightest)
	2.790	140.4	0.194	809.8	2.984 (Heaviest)

5.7 Summary

In this chapter, several different case studies were performed to illustrate the effect of placing various constraints on the sound package optimization. When there was air leakage present in the sound package, the transmission performance deteriorated at high frequencies while the absorption performance remained nearly the same. The possible weight optimization range broadened when the mass of the rigid panel in front of the sound package increased owing to the higher transmission

performance provided by the steel panel. From the higher termination impedance case study, the optimized solutions for the limp porous tended to converge to a lower flow resistance while a flexible MPP tended to a higher flow resistance in order to maximize the barrier performance at the expense of the absorption performance. Finally, it was seen that applying different frequency weightings to the objective function had a noticeable, but not large effect on the optimal surface densities.

CHAPTER 6. SOUND PACKAGE MODELING BY USING A FINITE ELEMENT APPROACH

6.1 Finite Element Analysis Setup

To this point, the weight optimizations have been based on a very simple interior geometry: i.e., a straight duct. It is of interest to see whether these results can be applied to more complex geometries representative of real vehicle interiors. So, in this chapter, the development and validation of a relatively simple model having a slightly more complicated shape, and which was implemented by using a finite element (FE) analysis tool will be described. Given that the FE model can be successfully validated, it becomes possible to predict the acoustic performance of the optimized sound packages identified previously for a complex geometry, such as a vehicle cabin: that work will be described in Chapter 7.

To validate the finite element approach, the absorption coefficient and the transmission loss of a sound package was first calculated using a finite element version of the standing wave tube model described in refs. [28] and [29] and shown in Figure 6.1, and they were compared to results of the analytical transfer matrix method approach. In order to emulate the standing wave tube in the finite element model, an axi-symmetric 2D model was used for the analysis, and a quad dominant mesh was enlarged. For the element size, the maximum element size was calculated based on the maximum frequency as

$$Element_{max} = \frac{c}{maximum\ frequency\ \mathrm{X}\ 5} = \frac{343\ [\frac{\mathrm{m}}{\mathrm{s}}]}{4000\ [\mathrm{Hz}]\ \mathrm{X}\ 5}. \tag{50}$$

That is, the maximum element size was required to be less than a fifth of a wavelength at the highest frequency of interest [30]. The boundary condition at the edges of the sound package was specified as free-free to avoid the edge-constraint effect [31]. For the input pressure, a plane wave was applied at the upstream end of the model. The diameter of the finite element model was chosen to be the same as the duct cross-sectional dimension for the analytical acoustic model. The absorption coefficient was estimated by using the two-microphone approach [32] based on the pressures “measured” at the two locations indicated in Figure 6.1, and the transmission loss was estimated based on the four-microphone method [33]. In the absorption calculation, the incident sound was directed towards the microperforated facing, and the aluminum panel rested against a hard termination. In the transmission cases, the sound also approached from the microperforated

panel side, but the sound package was backed by an anechoic space. Note that sound transmission through a layered system is reciprocal in the linear regime [34].

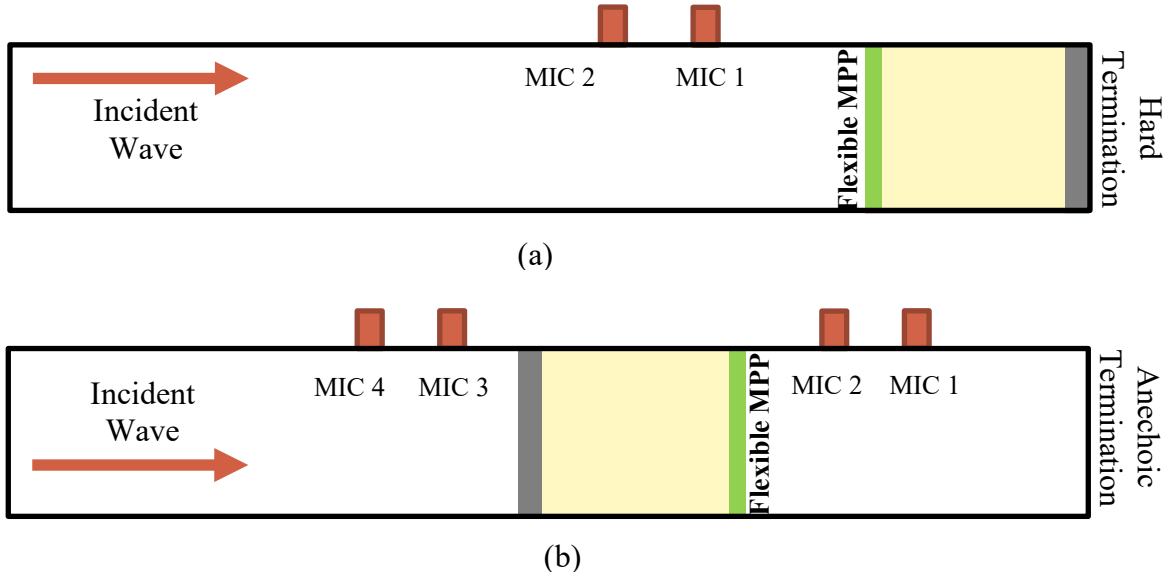

Figure 6.1: *Standing wave tube set-up for (a) absorption coefficient calculation (b) transmission loss.*

6.2 Flexible MPP Model (Limp Porous JCA Model)

In order to validate the flexible microperforated panel model in the FEA tool, a rigid microperforated panel was first modeled and verified. The rigid microperforated panel was modeled as an equivalent fluid by using the embedded Johnson, Champoux, Allard (JCA) model in the FEA tool [35]. The acoustical properties of the rigid microperforated panel used here are shown in Table 6.1. The absorption coefficient of the rigid microperforated panel with a 3 cm deep air-cavity depth behind it is shown in Figure 6.2 (a), and the FE prediction agreed well with the analytical TMM approach. The FE prediction of the transmission loss of the rigid MPP panel when backed by an anechoic termination is shown in Figure 6.2 (b), and the agreement with the TMM prediction is excellent. In Figure 6.2, the green solid line indicates the FEA solutions, and the blue solid line indicates the analytical solutions.

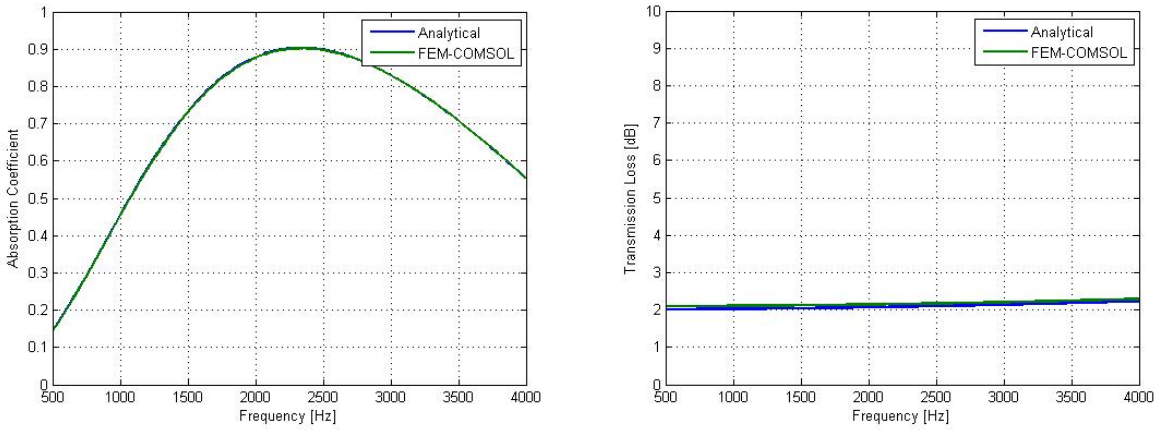

(a) (b)

Figure 6.2: *Plots of acoustic performance of a rigid MPP (a) Absorption coefficient (b) Transmission Loss.*

Once the rigid microperforated model created by using the FEA tool was validated, the flexible microperforated panel could be modeled by using the limp JCA model as described in previous work [29]. The acoustical properties of the flexible microperforated panel used here are also shown in Table 6.1. The absorption coefficient of the flexible microperforated panel backed with a 3 cm deep air-cavity depth is shown in the Figure 6.3, as is the transmission loss of the anechoically-backed panel. As seen in the figure, the absorption coefficient and transmission loss of the flexible MPP for both FEA and analytical solutions are in good agreement. Thus, it was concluded that the finite element model of the flexible MPP could be used with confidence. Note also that both the absorption coefficient and transmission loss of a lightweight flexible MPP are considerably smaller than those of its rigid counterpart due to the motion of the solid part of the panel in response to the incident sound field in the former case.

Table 6.1: Acoustic properties of sound package used for the COMSOL setup

Material	**Surface Density (kg/m^2)**	**Thickness (mm)**	**Young's Modulus (Pa)**	**Poisson's Ratio**
Aluminum Plate	2.7	1	$69x10^9$	0.33
Limp Porous	0.033	30		
Flexible MPP	0.010	0.2		
Material	**Porosity**	**Thermal Characteristic Length (m)**	**Viscous Characteristic Length (m)**	**Tortuosity**
Limp Porous	0.99	$105x10^{-6}$	$33x10^{-6}$	1
Flexible MPP	0.05	$50x10^{-6}$	$50x10^{-6}$	1
Material	**Hole Diameter (m)**	**Flow Resistance (MKS Rayls/m)**		
Limp Porous		617		
Flexible MPP	$100x10^{-6}$	213		

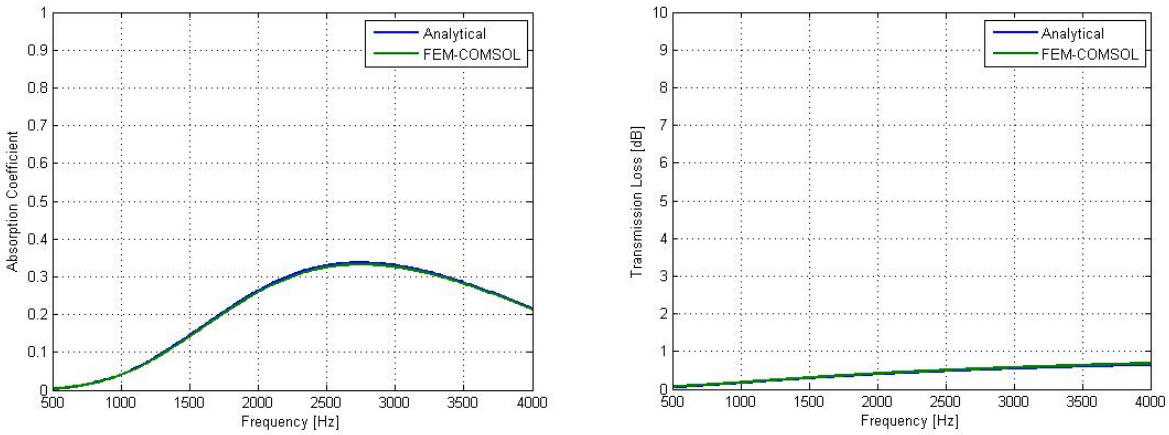

(a) (b)

Figure 6.3: *Plots of acoustic performance of a flexible MPP (surface density of 0.01 kg/m^2) (a) Absorption coefficient (b) Transmission Loss.*

6.3 Limp Porous Model (Limp Porous JCA Model)

Similarly, it was necessary to validate the finite element model of the limp porous layer. In order to calculate the absorption coefficient of the rigid porous material using COMSOL 5.2. The normal incidence absorption coefficient was calculated as

$$\alpha_{FEM} = 1 - \left|\frac{P_{scat}}{P_{in}}\right|^2 \tag{51}$$

where, P_{scat} indicates the pressure difference between the total acoustic pressure and the input pressure, P_{in}: i.e., the reflected pressure. For the transmission loss calculation, the incident power at the upstream surface and the outgoing power at the downstream surface were calculated, respectively, as

$$W_{incident} = \int_{\partial\Omega} \frac{|P_0|^2}{2\rho c}\, dA \tag{52}$$

where P_0 indicates the incident acoustic pressure amplitude at the upstream surface, and

$$W_{outlet} = \int_{\partial\Omega} \frac{|P|^2}{2\rho c}\, dA \tag{53}$$

where P is the acoustic pressure at a node at the anechoic termination, and where in both cases the integration is performed over duct cross-sectional areas. Once the acoustic power at the inlet and outlet were calculated, the transmission loss was calculated as,

$$\mathrm{TL} = 10 \log\left(\frac{W_{inlet}}{W_{outlet}}\right). \tag{54}$$

Recall that the limp porous medium is modeled by modifying the rigid JCA model. The characteristic impedance, Z_c, the complex wave number, k_c, and the surface impedance of the rigid JCA layer, Z_{surf_imp}, respectively, were calculated by using the following equations:

$$Z_c = \sqrt{\tilde{\rho}_{eq}\tilde{K}_{eq}} \tag{55}$$

$$k_c = \omega\sqrt{\tilde{\rho}_{eq}/\tilde{K}_{eq}} \tag{56}$$

$$Z_{surf\_imp} = -\mathrm{j}Z_c \cot\left(k_c L_{porous}\right) \tag{57}$$

where, L_{porous} indicates the depth of the porous layer, and $\tilde{\rho}_{eq}$ and $\tilde{K}_{eq}$ denote the complex equivalent density and bulk modulus, respectively, of the rigid porous material [1]. The equivalent density of a limp model can be obtained by considering the apparent density of the porous medium, $\rho_{mat} = (1-\phi)\rho_S + \phi\rho_o$, where ρ_S denotes the density of the solid part constituting the skeleton, and ϕ and ρ_o denote the open porosity and fluid density, respectively [1, 29].

In Figures 6.4 (a) and (b), respectively, the absorption coefficient and transmission loss for a 3 cm deep layer of rigid porous media are plotted: the material properties used in the calculation are listed in Table 6.1. In the absorption case, the porous layer was given a hard backing; in the transmission case, it was given an anechoic termination. As shown in the graphs, the analytical approach and the finite element method agreed well, although there was a small discrepancy in the high frequency region. As a further check, the surface impedance and the complex wave number of the rigid porous material were plotted along with the corresponding complex density and bulk modulus in Figures 6.4 (c), (f), (d) and (e), respectively.

In all cases, the analytically and numerically calculated values agreed well, but with minor high frequency differences. The absorption and transmission loss calculations were then repeated for the limp porous layer having the properties listed in Table 6.1: see Figure 6.5. As for the flexible MPP, both the analytical and FE predictions of the absorption coefficient and transmission loss of the limp porous layer agree reasonably well, and note that both are reduced compared to the rigid case, as expected for a lightweight limp porous layer.

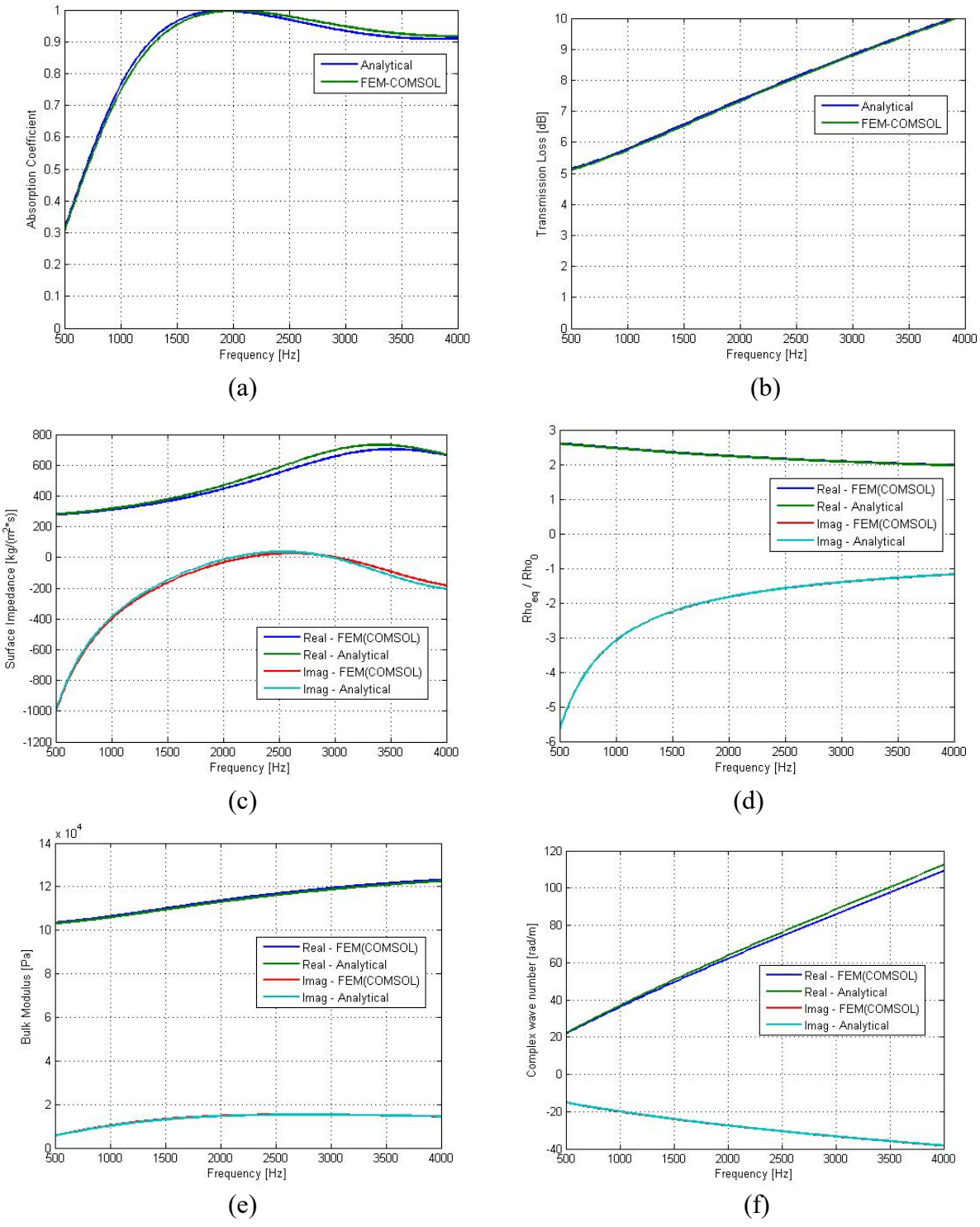

Figure 6.4: *Plots of acoustic performance of a rigid porous (a) Absorption coefficient (b) Transmission loss (c) Surface impedance (d) Complex density (e) Bulk modulus (f) Complex wave number.*

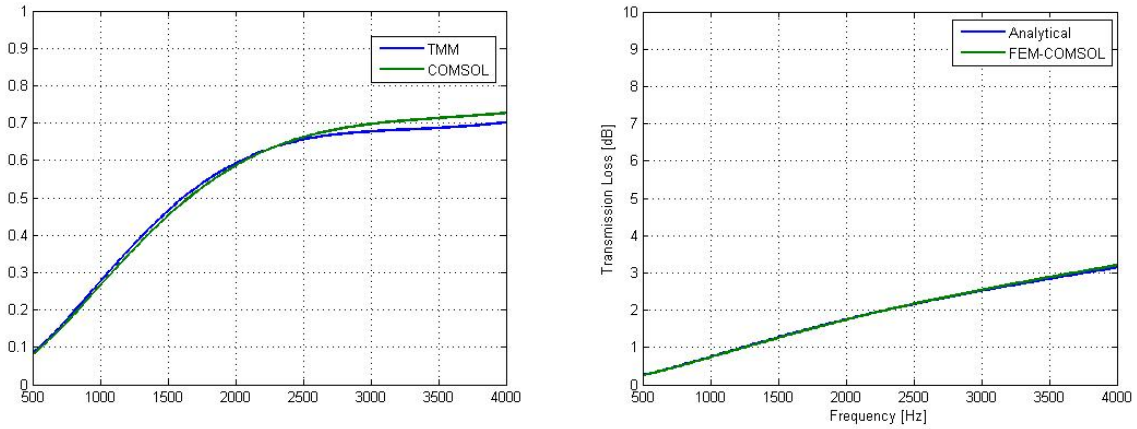

(a) (b)

Figure 6.5: *Plots of acoustic performance of a limp porous (a) Absorption coefficient (b) Transmission loss.*

6.4 Rigid Panel Model (Rigid Aluminum Model)

Finally, to validate the numerical approach for modeling the aluminum panel, the sound absorption of the panel placed against a hard backing and the transmission loss of the panel with an anechoic backing (and with free-free edge conditions) were calculated using the finite element method. The panel was modeled by using the “solid mechanics” feature in COMSOL. An Acoustic-Structure Interface feature was used to capture the coupling of the solid and a fluid motion. The results are compared in Figure 6.6, where good agreement between the analytical and numerical models can be seen. The panel offers no absorption by itself, and its transmission loss follows the mass law: i.e., the transmission loss increases by 6 dB for each doubling of frequency.

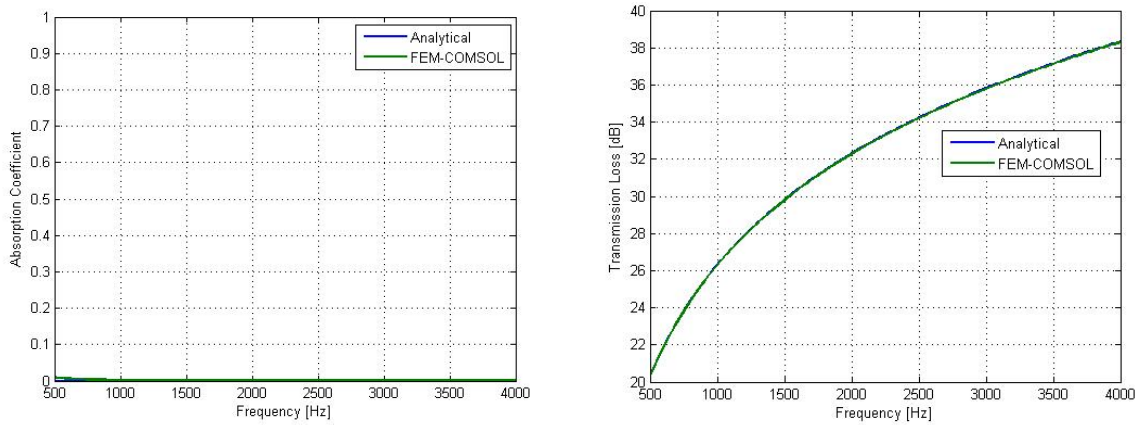

(a) (b)

Figure 6.6: *Plots of acoustic performance of an aluminum panel (a) Absorption coefficient (b) Transmission loss.*

6.5 Sound Package (Absorption and Transmission Calculation)

After verifying the modeling of both the flexible microperforated panel and limp porous layer by comparing the finite element calculation of the absorption coefficient and transmission loss of each material to the corresponding analytical prediction, the analytical and numerical models of the complete sound package as specified in Table 6.1 were then compared. Both the absorption coefficient of the hard-backed treatment and the transmission loss of the anechoically-terminated sound package are plotted in Figure 6.7, where again, it can be seen that there is excellent agreement between the analytical and numerical predictions, thus suggesting that the finite element model is working properly. Note that the transmission loss of the sound package is larger than that of the aluminum panel by itself owing to the presence of the MPP and porous layer.

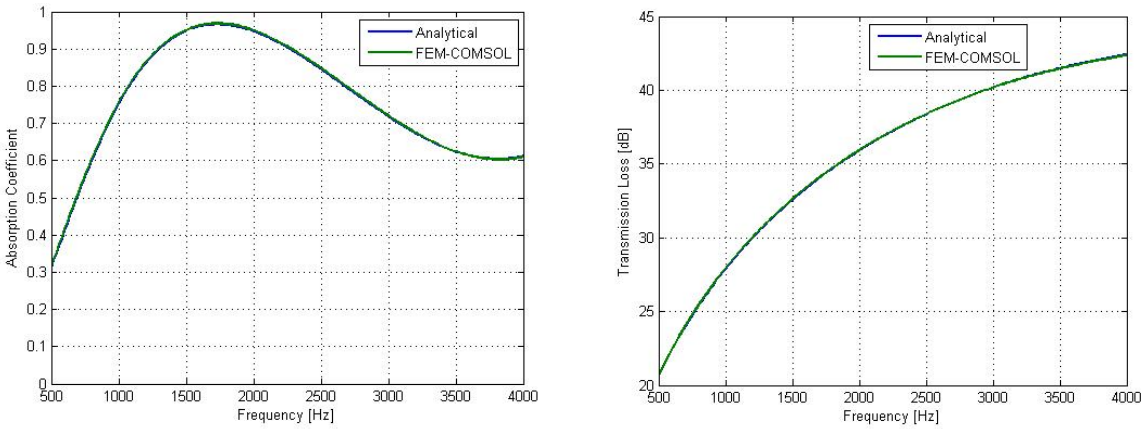

(a) (b)

Figure 6.7: *Plots of acoustic performance of a complete sound package with material properties listed in Table 6.1 (a) Absorption coefficient (b) Transmission loss.*

6.6 Space-Averaged Pressure in the Cavity)

Based on the finite element model described in this chapter, the acoustic performance of a sound package was first analyzed for a slightly more complex air-cavity geometry. That is before beginning the acoustic analysis of a realistic car cabin model, a rectangular chamber-like air-cavity was studied. The geometry of the air-cavity used for the analysis is shown in the Figure 6.8. The width of the cavity has been expanded, so that higher order modes are generated at the area transition from the sound package to the air cavity. This case is still simple enough that it can be approximated by using the transfer matrix method, and so provides a further test for the accuracy of the finite element model.

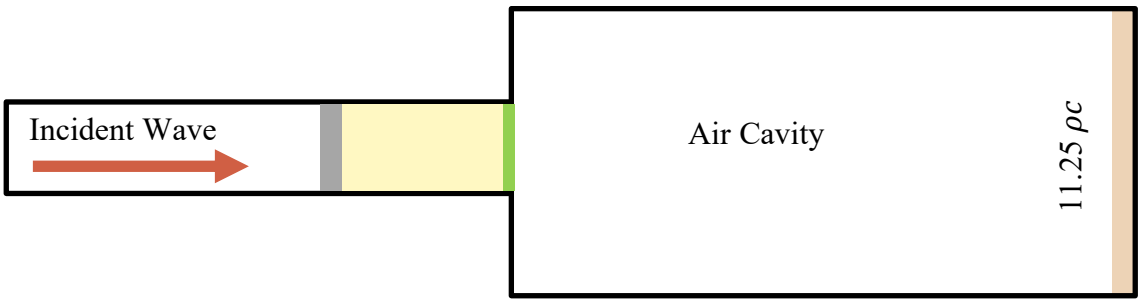

Figure 6.8: *Acoustic model for the chamber like air cavity.*

The boundary conditions and the input for the chamber-like air cavity were the same as for the duct-like air cavity (i.e., the no sudden-area-change case). As noted, the only difference here was the dimensions of the downstream chamber. The width of the chamber was chosen to be 10 cm, while the length remained the same at 50 cm. The impedance at the termination was the same as before, $11.25\rho c$. And also as before, to quantify the acoustic performances of the sound package for a given geometry, the space-averaged effective pressure in the air cavity was calculated.

To validate the finite element model, the space-averaged pressure was compared with predictions made using an analytical model. For the analytical approach, to account for the sudden area change at the junction between the sound package and the air-cavity, the transfer matrices for both the sound package and the downstream air cavity in the downstream were modified as follows by the incorporation of appropriate area factors: i.e.,

$$\begin{bmatrix} Q_{11} & Q_{12}/S_1 \\ Q_{21}S_1 & Q_{22} \end{bmatrix} \tag{58}$$

$$\begin{bmatrix} \cos kh & \dfrac{jZ_{air}\sin kh}{S_2} \\ \dfrac{jS_2\sin kh}{Z_{air}} & \cos kh \end{bmatrix} \tag{59}$$

$$Z_t = \frac{P_t}{U_t}S_2 \tag{60}$$

$$P_i = 1 + R \text{ and } U_i = \frac{S_1}{\rho c}(1 - R). \tag{61}$$

In these equations, $[Q]$ is the transfer matrix of the sound package, S_1 indicates the area of the upstream section as well as the sound package, S_2 in the cross-sectional area of the air cavity in the downstream section, Z_{air} indicates the characteristic impedance of air, k indicates the wave number in the air, h indicates the length of the air cavity in the horizontal direction, Z_t indicates the termination impedance, P_t indicates the acoustic pressure at the termination, U_t indicates the acoustic volume velocity at the termination, P_i and U_i indicate the acoustic pressure and volume velocity at the inlet, respectively, and ρc indicates the characteristic impedance of the air. These parameters are illustrated in Figure 6.9.

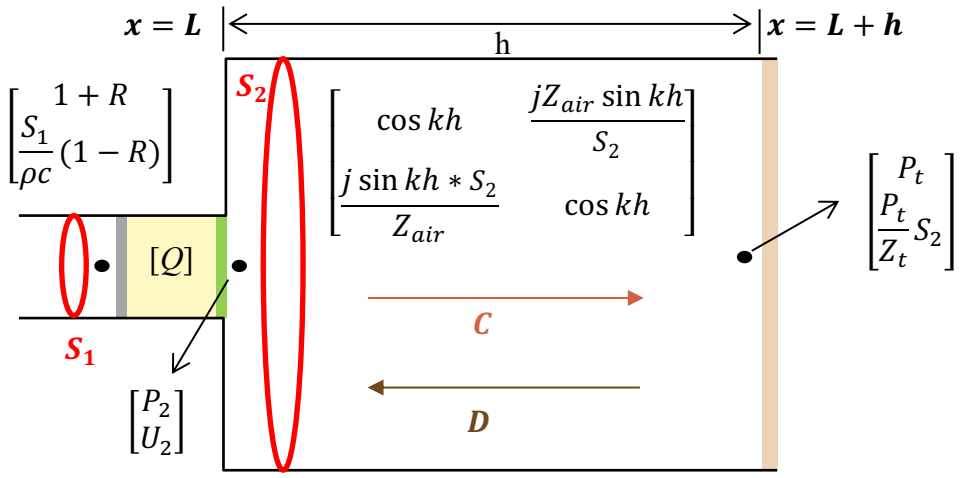

Figure 6.9: *Acoustic model for the transfer matrix method.*

Then, to calculate the sound pressure in the chamber, the transfer matrix was constructed as follow

$$\begin{bmatrix} P_i \\ U_i \end{bmatrix} = \begin{bmatrix} 1+R \\ \frac{S_1}{\rho c}(1-R) \end{bmatrix} = \begin{bmatrix} Q_{11} & Q_{12}/S_1 \\ Q_{21} * S2 & Q_{22} \end{bmatrix} \begin{bmatrix} \cos kh & \frac{jZ_{air}\sin kh}{S_2} \\ \frac{j\sin kh * S_2}{Z_{air}} & \cos kh \end{bmatrix} \begin{bmatrix} P_t \\ \frac{P_t}{Z_t} S_2 \end{bmatrix} \tag{62}$$

where $[Q]$ indicates the transfer matrix of the sound package, previously introduced in Chapter 4, of surface area of S_1. To simplify the above equation, the total matrix $[M]$ is defined as

$$\begin{bmatrix} M_{11} & M_{12} \\ M_{21} & M_{22} \end{bmatrix} = \begin{bmatrix} Q_{11} & Q_{12}/S_1 \\ Q_{21} * S2 & Q_{22} \end{bmatrix} \begin{bmatrix} \cos kh & \frac{jZ_{air}\sin kh}{S_2} \\ \frac{j\sin kh * S_2}{Z_{air}} & \cos kh \end{bmatrix}. \tag{63}$$

Then, Equation (62) can be solved to give the reflection coefficient, R, as follows:

$$R = P_t\left(M_{11} + M_{12}\frac{S_2}{Z_t}\right) - 1. \tag{64}$$

Once R is obtained, it can be substituted back into Equation (62) to calculate the sound pressure at the termination,

$$P_t = \frac{2}{\left(M_{11} + M_{12}\frac{S_2}{Z_t} + M_{21}\frac{\rho c}{S_1} + \frac{\rho c}{S_1}\frac{S_2}{Z_t}M_{22}\right)}. \tag{65}$$

Next, since the pressure and the particle velocity immediately behind the sound package, indicated as P_2 and U_2, are related to the pressure at the termination, by the expression

$$\begin{bmatrix} P_2 \\ U_2 \end{bmatrix} = \begin{bmatrix} \cos kh & \frac{jZ_{air} \sin kh}{S_2} \\ \frac{j\, S_2 \sin kh}{Z_{air}} & \cos kh \end{bmatrix} \begin{bmatrix} P_t \\ \frac{P_t}{Z_t} S_2 \end{bmatrix} \tag{66}$$

P_2 and U_2 can be rewritten in terms of the plane wave pressure amplitudes in the chamber as,

$$P_2 = Ce^{-jk_{air}L} + De^{jk_{air}L} \tag{67}$$

$$U_2 = \frac{S_2}{\rho c}\left(Ce^{-jk_{air}L} - De^{jk_{air}L}\right). \tag{68}$$

By using equations (67) and (68), the unknown pressure amplitudes, *C* and *D,* can be calculated as

$$D = \frac{1}{2} e^{-jk_{air}L}(P_2 - \frac{\rho c}{S_2} U_2) \tag{69}$$

$$C = P_2 e^{-jk_{air}L} - De^{2jk_{air}L}. \tag{70}$$

Thus, the acoustic pressure at any location, *x,* in the chamber can now be predicted by using the equation,

$$P_x = Ce^{-jK_{air}x} + De^{jK_{air}x}. \tag{71}$$

The rest of calculations for the space-averaged pressure in the chamber remained the same as in the previous calculation process for the straight duct case.

To calculate the SAP by using COMSOL, both the real and imaginary parts of the acoustic pressures at 51 different nodes in the chamber, each 1 cm apart along the length of the chamber, were exported and post-processed by using Equation (71). The red solid box in the Figure 6.10 indicates the 51 node locations.

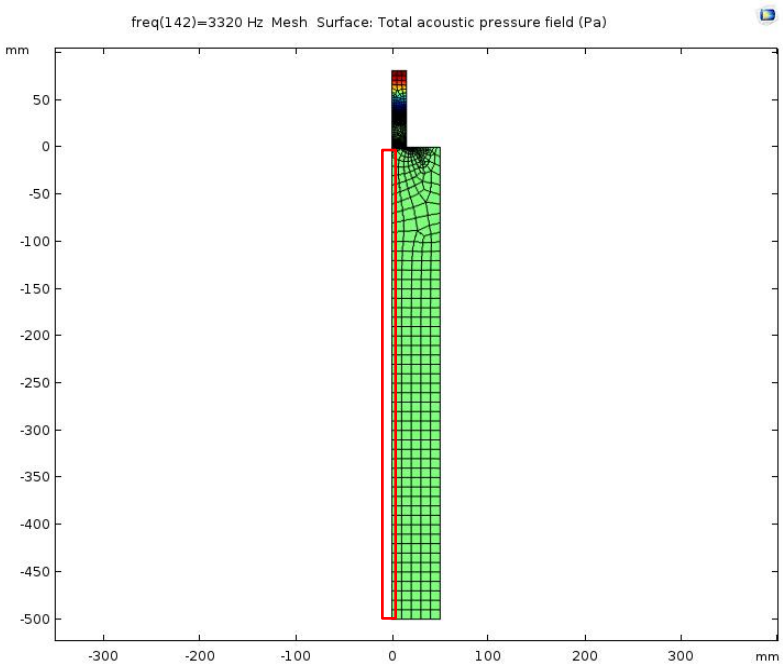

Figure 6.10: *COMSOL acoustic model used for the SAP calculations.*

In Figure 6.11, the space-averaged pressures in the chamber are plotted for both the analytical and finite element methods. The properties of the sound package used to calculate the SAP are listed in Table 6.1.

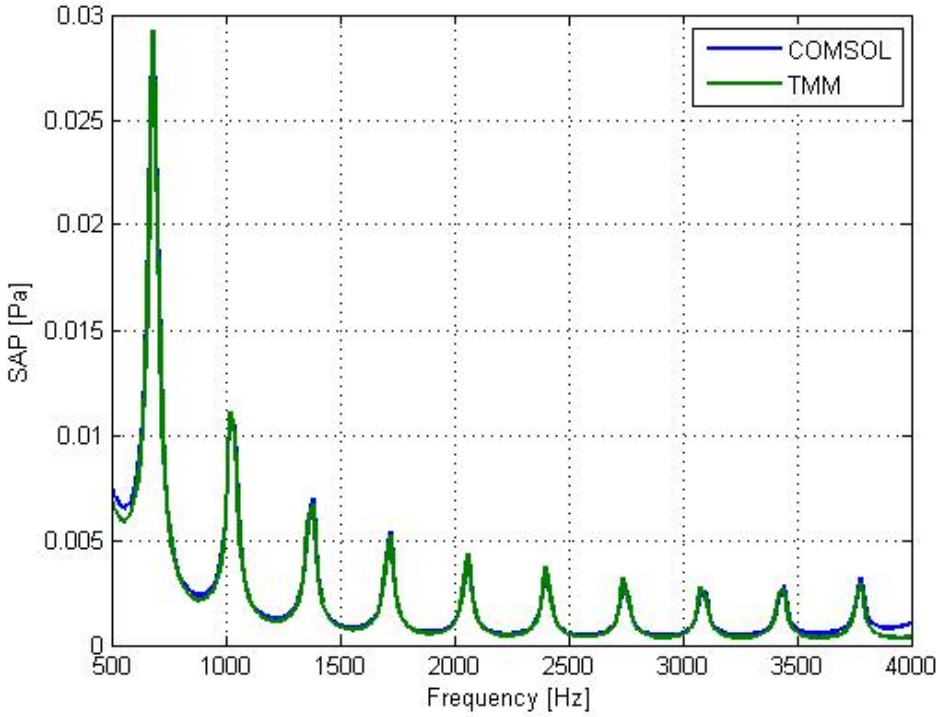

Figure 6.11: *Space-averaged pressures (green solid line) analytical approach (blue solid line) finite element approach for chamber-like air cavity.*

It can be seen that both analytical and finite element calculations agreed well, so that it is reasonable to conclude that the SAP in the chamber can be accurately predicted by using the finite element model developed in this chapter.

6.7 Optimization of the Weight of the Sound Package

In the previous section, a finite element analysis of the sound package for the chamber-like air cavity was described and results obtained using that model were compared to the analytical solution for validation purposes. In the work described in this section, optimization of the weight of the sound package for the chamber-like air cavity was performed to demonstrate the effect of the air-cavity shape on the optimization results. The optimized acoustic properties of sound package were then used to calculate the space-averaged mean square pressure in the air cavity. The optimization process remained the same, while the transfer matrices for the sound package and the air cavity were modified as mentioned in the previous section.

The heaviest and lightest optimized total surface densities for the chamber-like air-cavity case for various space-averaged pressures are plotted in Figure 6.12.

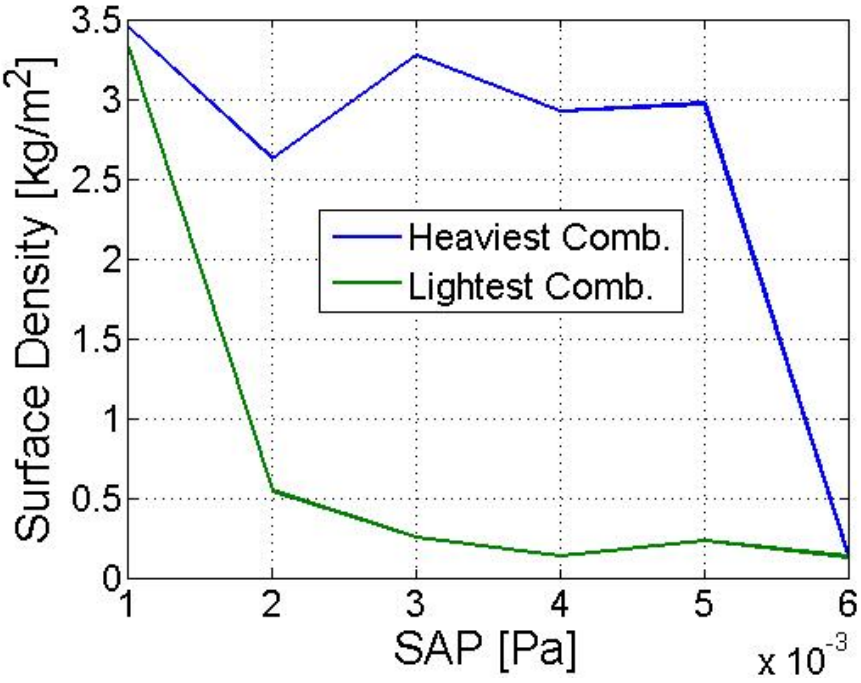

Figure 6.12: *Plots of total surface density with respect to various space-averaged pressures.*

The blue solid line indicates the heaviest surface density combinations for a given space-averaged pressure while the green solid line indicates the lightest surface density combinations.

The optimization process was intended to yield many different possible surface density combinations which yield the same space-averaged pressure for various targeted space-averaged pressures. These optimized surface density solutions are shown in Figure 6.13. Once again, it can be seen that the solutions converge to the largest surface density at the lowest space-averaged pressure, and to the smallest surface density at the highest target space-averaged pressures.

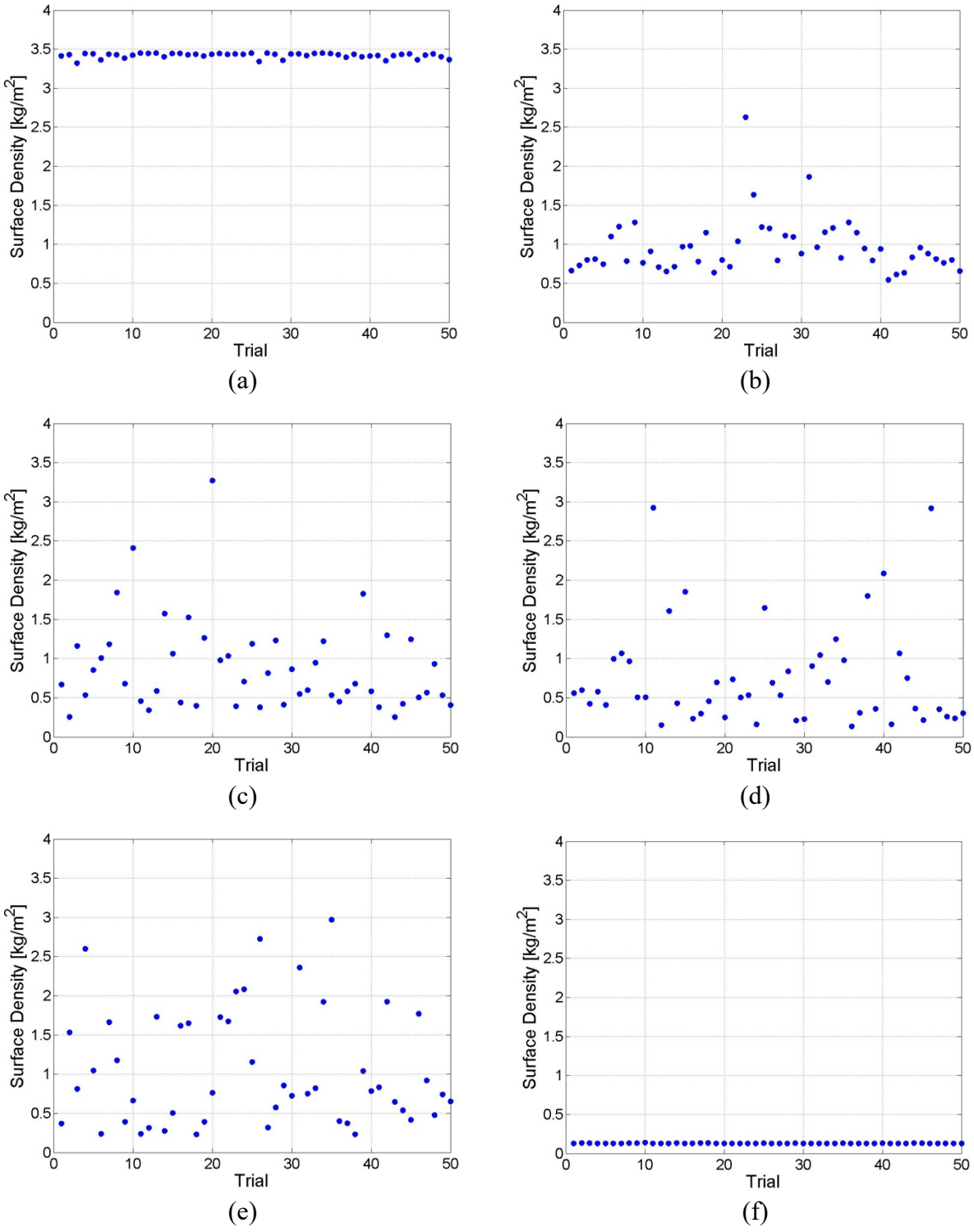

Figure 6.13: *Plots of various total surface densities that gave the targeted space-averaged pressure magnitude of (a) 0.001 Pa (b) 0.002 Pa (c) 0.003 Pa (d) 0.004 Pa (e) 0.005 Pa (f) 0.006 Pa.*

Among these many optimized solutions for the various space-averaged pressures, a space-averaged pressure of 0.004 Pa case was selected for further examination because the optimized surface density solutions were distributed evenly as shown in Figure 6.13 (c). The material properties of the heaviest and lightest sound packages that gave the space-averaged pressure of 0.004 Pa are shown in Table 6.2. In the lightest solution, most of the total flow resistance was provided by the porous layer while almost all of the surface density was provided by the MPP layer.

Table 6.2: Optimized noise treatment when space averaged pressure was 0.004Pa in the interior space.

Case	Flexible MPP	Limp Porous Layer	Total
Lightest Combination	Flow Resistance [MKS Rayls] 800.5	Flow Resistance [MKS Rayls] 1450.2	
	Surface Density [kg/m^2] 0.11	Surface Density [kg/m^2] 0.03	Surface Density [kg/m^2] 0.13
Heaviest Combination	Flow Resistance [MKS Rayls] 112.7	Flow Resistance [MKS Rayls] 903.3	
	Surface Density [kg/m^2] 2.72	Surface Density [kg/m^2] 0.21	Surface Density [kg/m^2] 2.93

Both the absorption and transmission performance of the sound package that yielded the space-averaged pressure of 0.004 Pa are plotted in Figure 6.14. It can be seen from these plots that the lightest solution tends to emphasize barrier performance at the expense of absorption performance, as seen in a number of examples before.

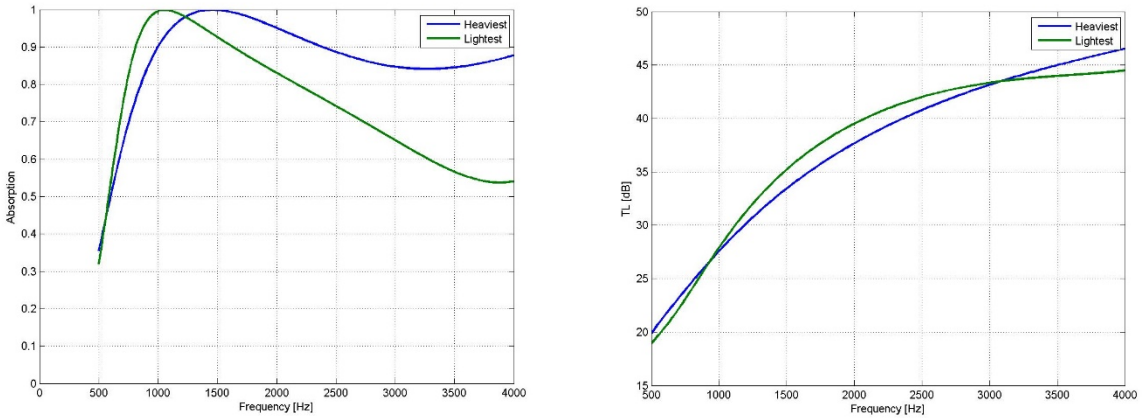

(a) (b)

Figure 6.14: *Plots of (a) absorption coefficient and (b) transmission loss of the optimized sound package that yielded the space-averaged pressure of 0.004 Pa.*

The space-averaged pressures for the 0.004 Pa case are plotted as a function of frequency for both the finite element and analytical approach are shown in Figure 6.15. The difference between the two results, visible at very low frequencies results from the neglect of nearfield effects in the analytical model: i.e., the non-propagating nearfield generated at the area transition. That effect is accounted for in the finite element model. So, in that respect, the finite element model is more accurate than the analytical model. Nevertheless, as shown in the Figure 6.14, the finite element model generally agreed well with the analytical prediction. Therefore, in principle it is now possible to optimize the weight of the sound package when connected to spaces having complex geometries by using a finite element method.

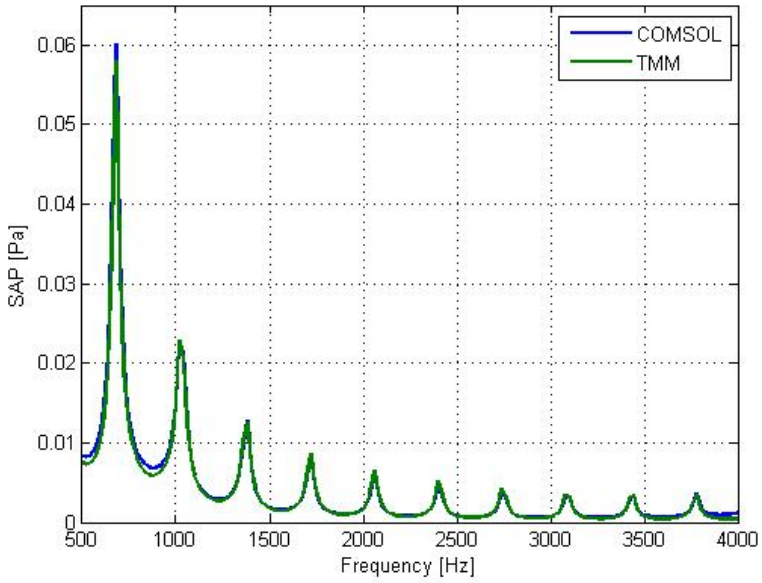

Figure 6.15: *Space-averaged pressures of 0.004 Pa (a) analytical approach (b) finite element approach for chamber-like air cavity.*

6.8 Summary

In this chapter, a finite element approach to analyzing the acoustic performance of the sound package was demonstrated. The absorption coefficient and the transmission loss of the sound package were obtained using COMSOL 5.2 and they showed good agreement with the analytical approach using the transfer matrix method. Therefore, the finite element analysis offers a valid approach for modeling the performance of sound packages under more realistic geometrical conditions.

A chamber-like air cavity in the downstream section was introduced in order to make it possible to conduct a preliminary study of the effect of the air cavity shape behind the sound package on the optimization results as well as to compare with the previous duct-like air cavity. The results obtained from the chamber-like air cavity by using the finite element method agreed well with the analytical results. Thus, it will now be possible to consider more complicated geometries in the optimization study. However, it was ultimately found not to be feasible to simply replace the TMM calculation with the FE calculation in the optimization process owing to the lengthy computation time required. Thus, it was decided to pursue an alternative approach, as described in the next chapter.

CHAPTER 7. SOUND PACKAGE MODELING BY USING A FINITE ELEMENT APPROACH

Following the FE numerical model development for the MPP and the limp porous layer, and the preliminary validation described in Chapter 6, the geometry of the downstream air cavity was modified to a shape that was more characteristic of a vehicle interior volume. As noted previously, since the FE calculations proved to be prohibitively computationally expensive, they could not be incorporated directly into the optimization procedure. Thus, as an alternative, the FE model was used instead to see whether it was possible to establish a link between the space-averaged pressure in the straight duct, and in the vehicle-shaped space. If that is possible, then the results of the relatively fast TMM optimization procedure can be applied to find treatments that satisfy specific targets in a more realistic environment.

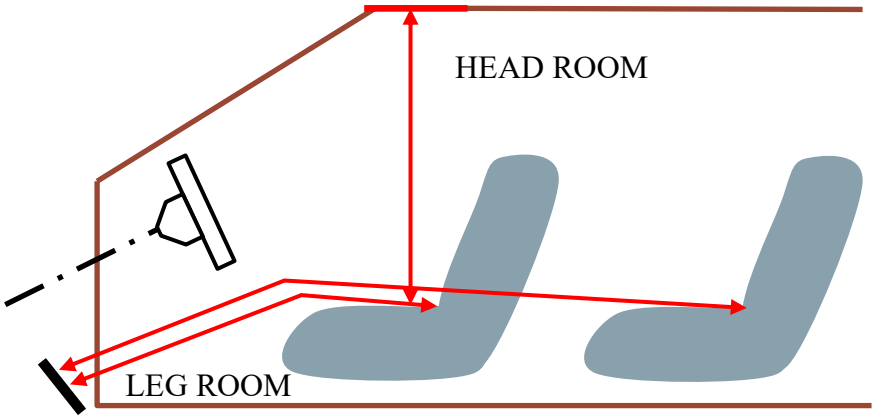

Figure 7.1: *Vehicle interior space mockup.*

7.1 Modeling of Vehicle-Like Air Cavity

Figures 7.1 and 7.2 illustrate the dimensions that were used to describe the dimensions and volume of the vehicle interior. Note, again, that the vehicle interior model is still two-dimensional for the sake of computation speed. For conventional passenger vehicles, the head room dimension typically falls between 1000 mm and 1100 mm, and the front and rear leg room falls in between 1800 mm and 2100 mm [35]. The vehicle interior space was modeled here based on those dimensions. In Figure 7.2, the air cavity that was used for the analysis is shown. As noted, the

model was built in 2-dimensions to reduce the calculation time and complexity, and the total area of the air space was 1.6 m^2.

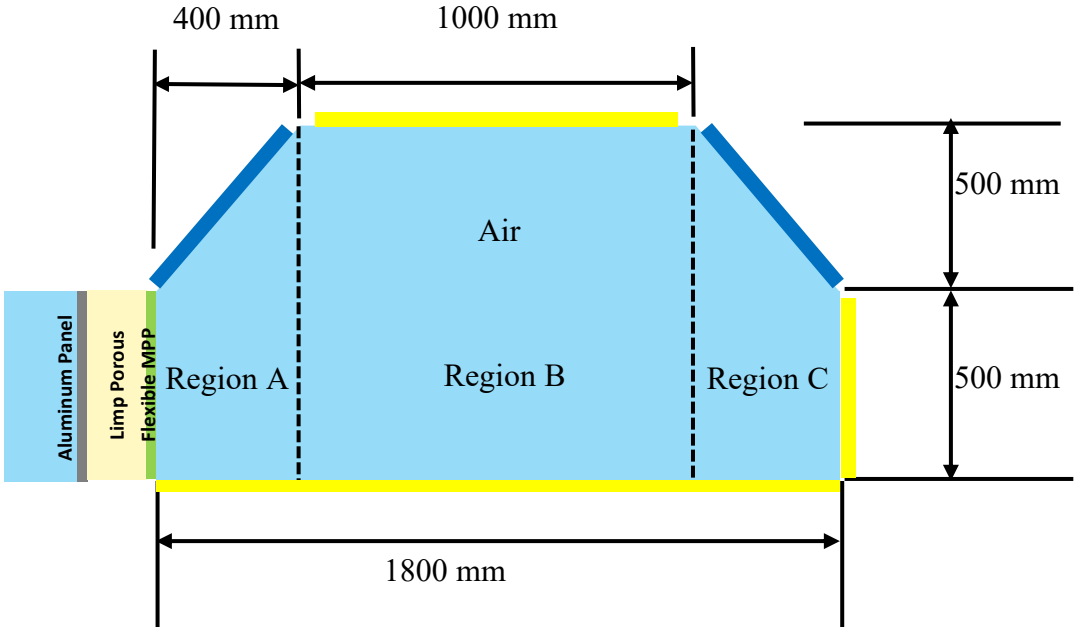

Figure 7.2: *Vehicle interior space dimensions used for the FEM analysis.*

In Figure 7.2, the dark blue surfaces were given high impedances (representing the windshield, hard trim, etc.) while the yellow boundaries indicate relatively absorbent surfaces, such as the car seats, carpets, etc. The relationship between the space-averaged pressure and the surface impedance (controlling the average absorption in the air cavity) will be demonstrated in a latter section.

Because of the more complex geometry compared to the uniform duct considered previously, i.e., because of the area expansion and contraction in regions *A* and *C*, an analytical approach based on using the TMM is not suitable. Thus, a finite element analysis tool was used to calculate the sound pressure in the downstream air cavity, and the results were used to calculate interior space-averaged pressures that could be compared with the rectangular duct case.

7.2 Finite Element Analysis Setups

Here, the energy density, averaged input intensity, and space-averaged pressure were calculated to quantify the performance of the sound packages. To calculate the space-averaged pressure in the vehicle cabin, the spatial-averaging feature of COMSOL was used. That spatial-integration method is independent of the number of elements in the domain [37]. For example, a variable such as the pressure, that is a function of both x and y-coordinates, can then be integrated over the domain (i.e., $\int_{\Omega} F(x,y)\,dxdy$). This approach allows the various cases with different downstream geometries to be compared regardless of the total number of elements in the domain.

To check that the spatial integration method was working properly, a simple validation was performed and the results are shown in Table 7.1. The space-averaged sound energy density of several square ducts having the same areas (1 m^2) but having different numbers of elements (see Figure. 7.3) were calculated. In each case, the duct was terminated by an impedance of 11.25 ρc.

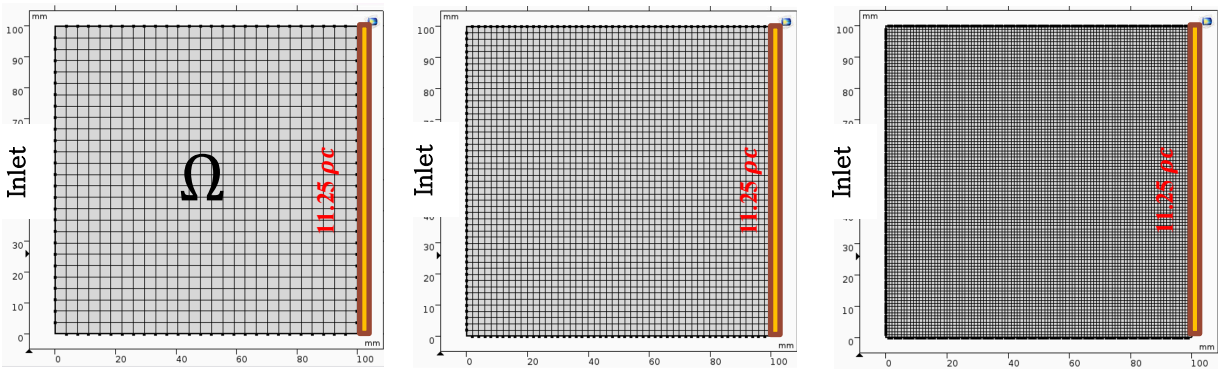

(a) (b) (c)

Figure 7.3: *Square ducts with different number of elements. The total number of element (a) 729, (b) 2500, and (c) 10000.*

Plane wave incidence was assumed at the inlet (on the left-hand face of the domains shown in Figure 7.3), and the space-averaged sound energy density (Pa) in the cavity was calculated by using the equation

$$E_{cavity} = \frac{1}{A}\int_{\Omega} \frac{|P|^2}{\rho c^2}\,dA. \tag{72}$$

where Ω denotes the domain being analyzed, P denotes the effective (i.e., rms) pressure amplitude of the field in the domain, and where A denotes the area of the domain. The space-averaged pressure was similarly calculated as,

$$SAP_{cavity} = \frac{1}{A}\int_{\Omega} |P|\, dA,. \tag{73}$$

Table 7.1: Energy density, SAP in the domain for different number of elements.

Case	Number of Element	Energy Density [Pa]	SAP [Pa]
Case (a)	**729**	**1.9301 X 10^{-7}**	**1.1905**
Case (b)	**2500**	**1.9301 X 10^{-7}**	**1.1905**
Case (c)	**10000**	**1.9301X 10^{-7}**	**1.1905**

In Table 7.1, note that, the energy density in the air domain for the three different cases are all the same. Thus, it can be concluded that the spatial-integration method is an effective approach for comparing cases modeled with different numbers of elements.

To extend the finite element analysis case study, energy density calculations for different downstream areas were performed to check the effect of area on the energy calculation. In Figure 7.4, the two straight ducts with different areas used for the energy density calculation are shown. In both cases, the plane wave input was the same, as were the termination impedances. The only difference between these two cases was the area: case (a) has an area of 1 m^2 while case (b) has an area of 0.5 m^2.

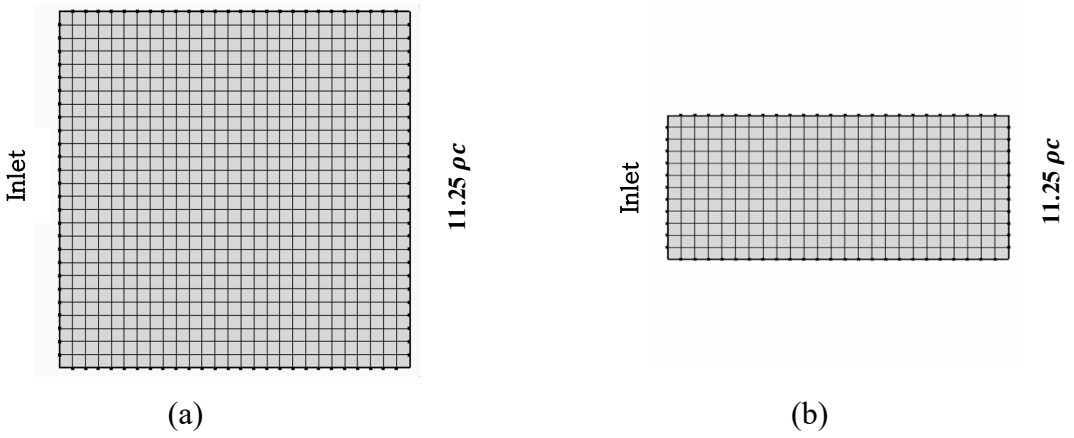

Figure 7.4: *Ducts with different area.*

The energy density calculation results obtained by using COMSOL are shown in Table 7.2 for these cases. It can be seen that the total integrated energy density for the two cases are different, but that the area-normalized energy density for these cases are the same. Thus, it is concluded that the energy density for two different areas can be directly compared by normalizing with respect to their surface area. This conclusion leads to the idea that the results of sound package weight optimization that were obtained by using the TMM in combination with a small straight duct can conceivably be compared to more realistic cases with relatively larger surface area.

Table 7.2: Energy density, Area, and Area-normalized energy density for the two different areas.

Case	Integrated Energy Density [Pa]	Area [m^2]	Energy Density/Area [Pa/m^2]
Case (a)	**1.2063 X 10^{-7}**	**1**	**1.2063 X 10^{-7}**
Case (b)	**6.0315 X 10^{-8}**	**0.5**	**1.2063 X 10^{-7}**

7.3 Contribution of the Area Expansion to the Space-Averaged Pressure

It was seen that simple area differences between two different geometries do not necessarily have an effect on their normalized energy density as long as the boundary condition remains the same in the two cases. However, this is possibly not true for cases that involve an area change within the domain. For example, the vehicle-like geometry introduced in Figure 7.2 has an area change between regions *A* and *B*, and the results is an impedance change at the inlet boundary, which in

turn leads to a sound reduction in the chamber. Thus, the effect of a progressive area change on the space-averaged pressure in the cavity is described in this section.

In Figure 7.5, two different geometries with the same surface area are shown. Case (a) represents the straight duct case, and (b) indicates the vehicle-like geometry case.

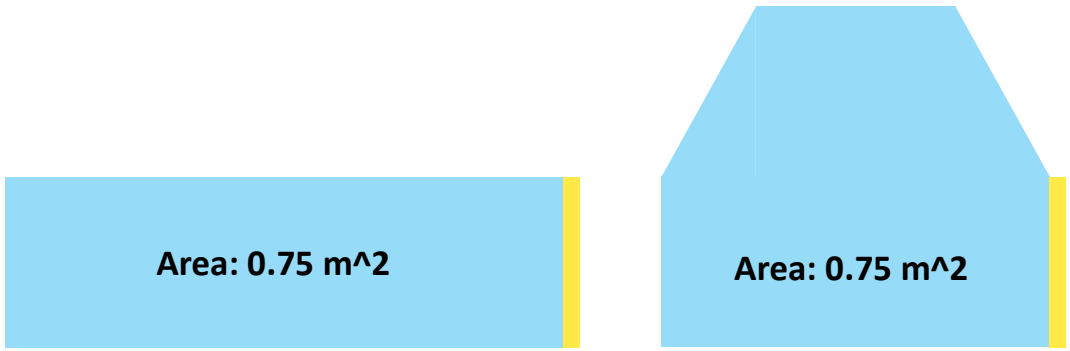

Figure 7.5: *Anechoically terminated two different geometries. (a) straight duct case, (b) vehicle-like-cavity case.*

For the analysis, plane wave incidence was assumed at the inlet, and an anechoic termination condition was applied at the end of the downstream section. The transmission loss for both cases were calculated by using Equations (52) to (54), and the results are plotted in Figure 7.6. It can be seen that the straight duct (blue solid line) does not show any significant energy loss since there is no impedance change along the length of the duct. However, the vehicle-like cavity (red solid line) shows a small, but noticeable transmission loss because of the impedance mismatch caused by the area changes.

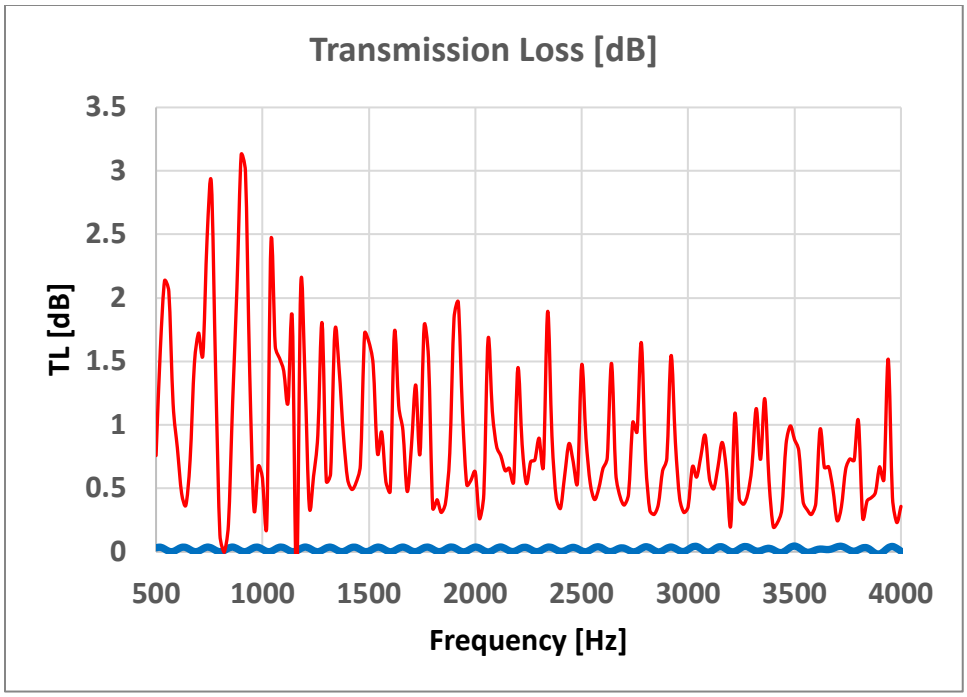

Figure 7.6: *The Transmission Loss of a straight duct (blue solid line) and a vehicle-like-cavity (red solid line).*

To demonstrate the effect of area-change when the sound package is present, the Transmission Loss with the sound package in place was calculated and is plotted in Figure 7.7. It can be seen that the area changes in the air cavity caused a slight increase in the Transmission Loss (red solid line) that can be seen as the ripples in the Transmission Loss curve. The material properties used for the calculation are listed in Table 7.3. Thus, it can be concluded that the geometry of the interior space has some impact on the sound energy in the cavity.

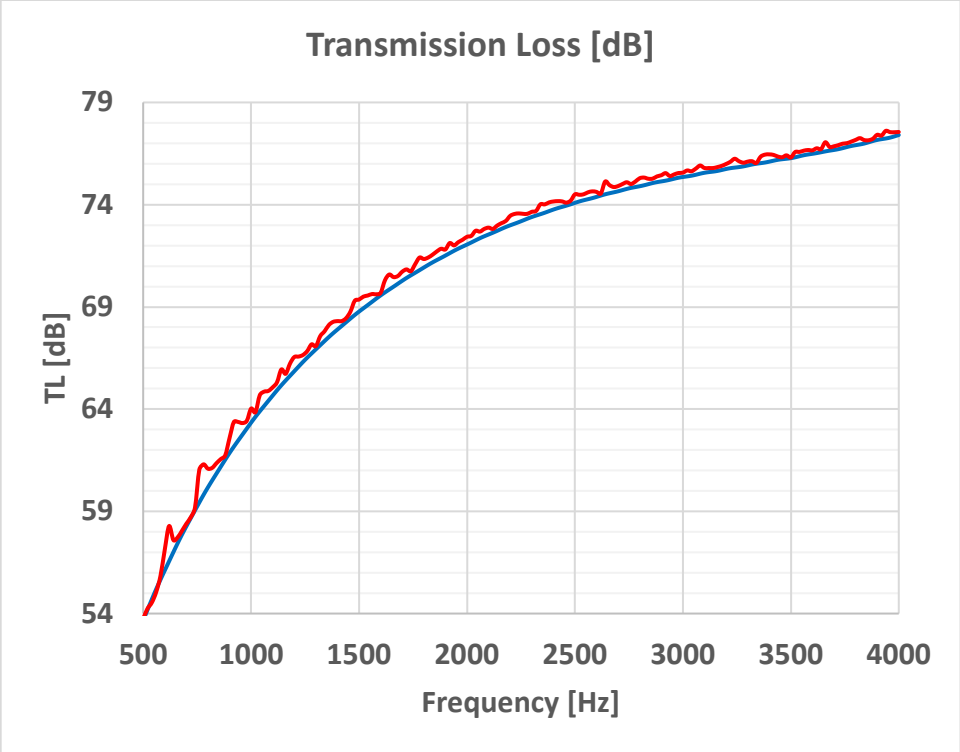

Figure 7.7: *The Transmission Loss of a straight duct (blue solid line) and a vehicle-like-cavity (red solid line) with the sound package.*

Table 7.3: Material properties of the sound package.

	Flexible MPP	**Limp Porous Layer**	**Total**
Sound Package	Flow Resistance [MKS Rayls] 654.9	Flow Resistance [MKS Rayls] 650.7	Flow Resistance [MKS Rayls] 1305.6
	Surface Density [kg/m^2] 0.77	Surface Density [kg/m^2] 0.06	Surface Density [kg/m^2] 0.83

7.4 Space-Averaged Pressure in the Cavity

In this section, the process of calculating a space-averaged pressure in the vehicle-cabin-like cavity is demonstrated. The space-averaged pressure of the vehicle-cabin-like cavity is then compared to that of a straight duct case to validate the idea that optimization procedure introduced in Chapter 4 can be applied to more realistic cases. If that is indeed the case, then, the process used to minimize

the weight of the sound package in practical situations becomes simple and less expansive in terms of computational resources since the simple straight duct model can be used as a reference.

In Chapter 6, the procedure used to perform the space-averaged pressure calculation in the air cavity was demonstrated. Here, the procedure used to calculate the space-averaged pressure in the vehicle-cabin-like cavity, in particular, is introduced. Since the geometry of the air cavity is no longer uniform, plane wave propagation cannot be assumed. Thus, finite element software was used to calculate the pressure in the air cavity for the space-averaged pressure prediction. Figure 7.8 shows the model that was used to calculate the acoustic pressure in the vehicle-like-cavity.

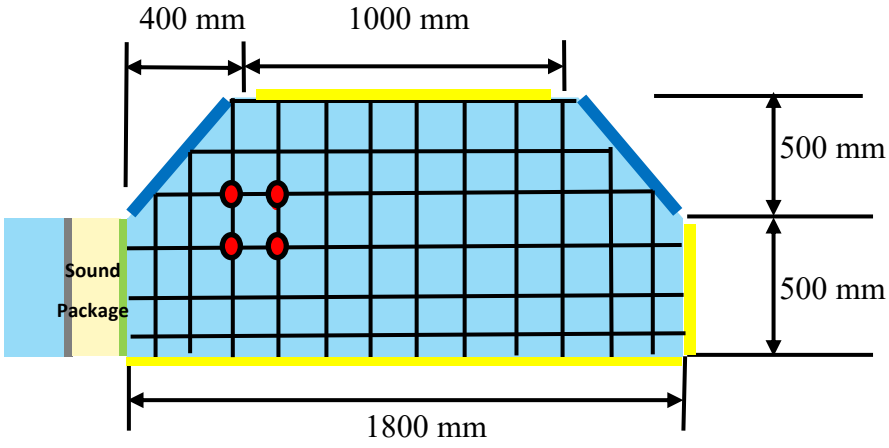

Figure 7.8: *Model used for the space-averaged pressure.*

The dots indicate the nodes where the sound pressure was calculated: note that in the actual calculation, all the nodes, in the model were used for the calculation. Here, 4 nodes are highlighted in the figure for explanation purposes only. The space-averaged pressure was calculated in the same way as for the straight duct case, but instead of using Equation (31), the calculation was performed by averaging the absolute acoustic pressures in the domain by using the finite element tool.

The TMM optimization was performed 50 different times to obtain 50 different possible sound package solutions which have distinct flow resistivities and surface densities for both the limp porous layer and the flexible MPP (the target SAP in this case was 0.019 Pa [59.6 dB]). In order to see how the TMM optimized results based on a duct-like cavity perform in the vehicle-like cavity case, the 8 lightest combinations (total surface densities less than 0.8 kg/m^2 in Figure

4.4.) obtained from the optimization were used as inputs to the vehicle-like cavity case to calculate the space averaged pressures and the results are plotted in Figure 7.9.

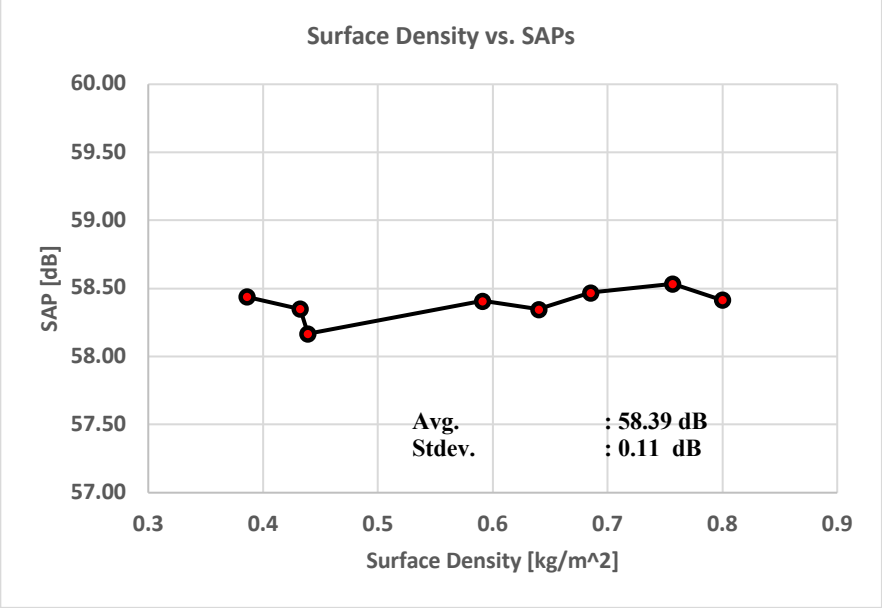

Figure 7.9: *Space-averaged pressure in the vehicle-like cavity.*

It can be seen that space-averaged pressures in the vehicle-like cavity showed good consistency in terms of magnitude. Thus, it was concluded that the optimized results obtained by using a straight duct cavity can yield the similarly consistent space-averaged pressure distributions in the vehicle-like cavity case. Recall that, the optimized sound packages for the duct-like cavity case resulted in a space-averaged pressure of 0.019 Pa (59.6 dB). However, the same sound packages gave a space-averaged pressure of 0.016 Pa (58.4 dB) for the vehicle-like cavity case;

7.5 Space-Averaged Pressure Comparison Between Duct-Like Cavity vs. Vehicle-Cabin-Like Cavity

Figure 7.10 shows the relation between the SAPs for the rectangular duct and the vehicle-like geometry cases. The average of the SAPs resulting from 10 different surface density combinations (the set of 10 lowest surface densities that gave the same SAP in the TMM case) were calculated using the FE model and were plotted over the downstream SAP range in the TMM case from 0.013 Pa (~56 dB) to 0.028 Pa (~63 dB).

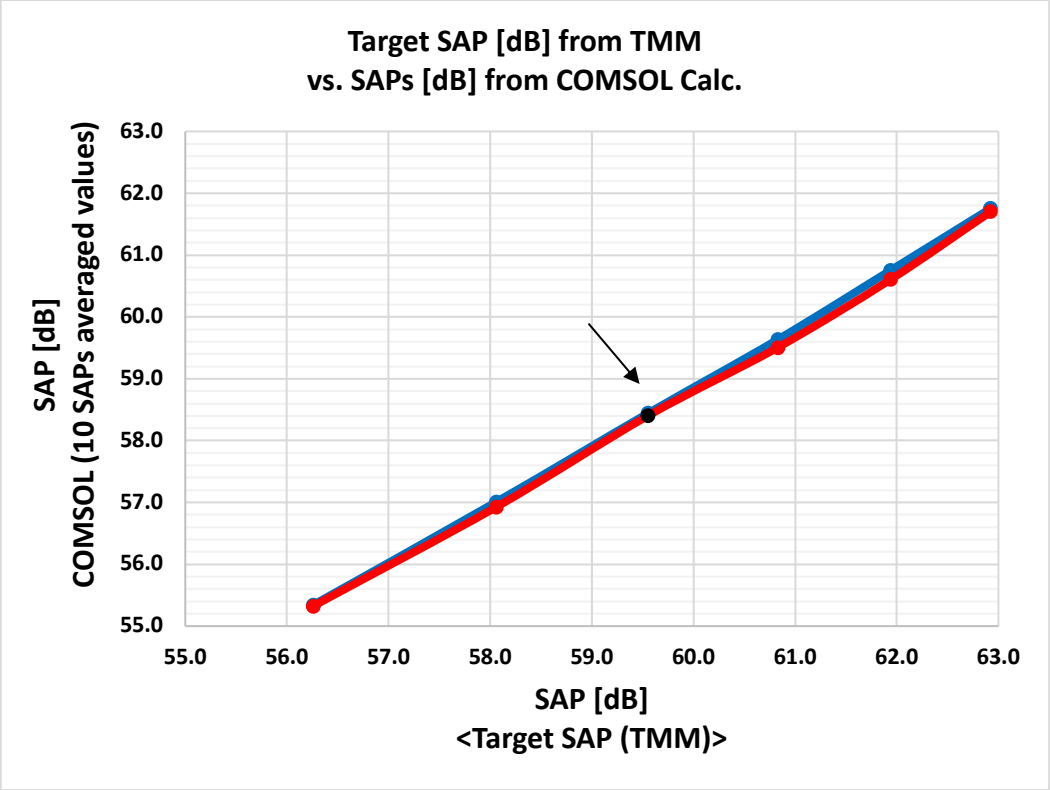

Figure 7.10: *Space-averaged pressures for the rectangular duct case vs. vehicle-like cavity case.*

The rectangular shape and the complex geometry cases were given the same sound package material properties. The only difference between these two are the downstream area and its shape. The red solid line indicates the averaged 10 heaviest surface density combinations for the various space-averaged pressures. Likewise, the blue solid line indicates the averaged 10 lightest surface density combinations for the various space-averaged pressures. For example, the black dot pointed by a black arrow (Figure 7.10) indicates the average of 10 different space-averaged pressures calculated with the 10 heaviest surface density combinations obtained from the optimizer for both rectangular case (59.6 dB) and the complex geometry case (58.4 dB).

That magnitude difference results from several different effects. As stated in the previous section, area changes can reduce the pressure level in the cavity. Another possibility is that the average absorption difference in the two cavities has an effect. In the duct-like cavity case, the termination impedance was set to $11.25\rho c$, which gives an absorption of 0.3. Here, in the vehicle-like cavity case, the impedance of $11.25\rho c$ was applied only to the surface which was directly opposite the inlet surface, which gave an average absorption of only 0.03 in the cavity. Thus, the

effect of the average absorption in the downstream (air cavity) on the space-averaged pressure is demonstrated in the next section.

The average SAPs for the two cases are quantitatively different, however, it can be seen that the trend of SAP increase (slope) in the duct case and the complex geometry case is similar. Thus, it can be concluded that the results that are obtained from the TMM-based sound package weight optimizer can be extended to the larger and more complex geometry case.

7.6 Effect of the Average Absorption in the Cavity

In previous sections, the SAPs of the rectangular-shaped cavity case were calculated with an absorption of 0.3 (corresponding to the termination impedance of 11.25 ρc) at the end of the straight duct downstream section. On the other hand, the finite element analysis was not performed with that average absorption in the downstream section: the average absorption in that case was 0.03. That is, the absorption patch was the same in both cases, but the total interior surface area in the second case was much larger, hence decreasing the average absorption. In order to match the absorption in the air cavity to that of the TMM case, the equation giving the average absorption for evenly distributed absorption surfaces was used: i.e.,

$$\overline{\alpha_{Total}} = \frac{\sum S_i A_i}{S} \tag{74}$$

where S denotes the total interior surface area, while S_i is the area of each surface having the absorption coefficient A_i, and $\overline{\alpha_{Total}}$ denotes the average absorption coefficient of the interior.

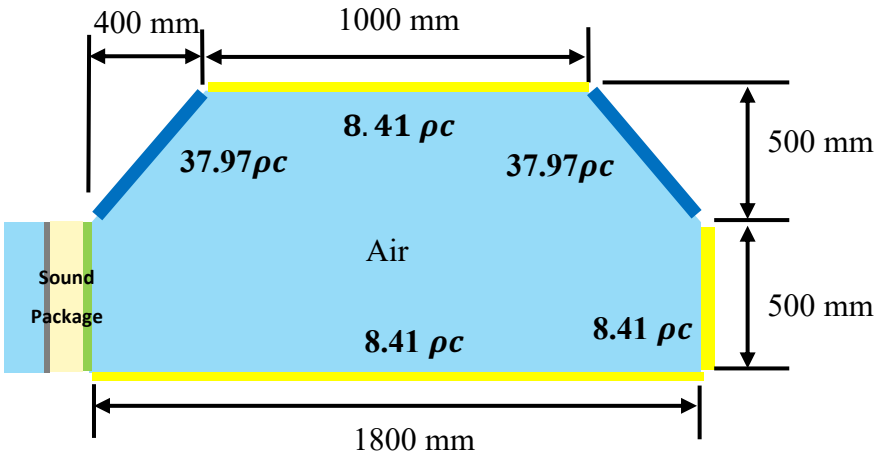

Figure 7.11: *Impedance of each surface which makes the average absorption in the downstream 0.3.*

To obtain an average absorption of 0.3, the surfaces corresponding to the front and rear windows were given an absorption of 0.1, while the rest of the surfaces (nominally describing the roof, carpet, and seats) were given an absorption of 0.38. The impedances corresponding to those absorptions are shown in Figure 7.11. Recall that a 1 Pa plane wave was assumed to be incident on the exterior surface of the sound package.

Figure 7.12 demonstrates the effect of the average absorption in the downstream section on the SAPs. In that figure, the SAPs of the 8 different surface density combinations (surface densities less than 0.8 kg/m^2 in Figure 4.4) were calculated and plotted for both an average absorption of 0.03 (the original value) and 0.3 in the downstream section. The red solid line indicates the SAPs for various surface density combinations when the average absorption of the downstream was 0.3 while the blue solid line indicates the corresponding results for the average absorption of 0.03.

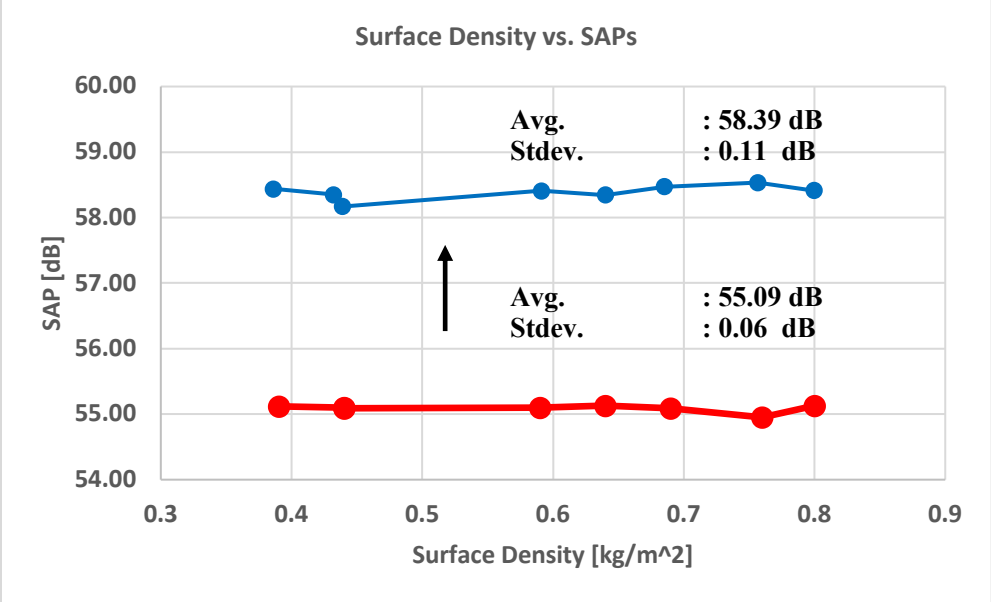

Figure 7.12: *Plots of surface density vs. SAPs for two different average absorption in the cavity.*

The black arrow indicates that the SAP increases in the downstream space due to the increase of surface impedance on the surfaces and hence the decrease in absorption. However, it can also be seen that although there was a magnitude difference between two the cases, the values followed a nearly identical trend. Therefore, it can be concluded that the absorption difference in the

downstream section has a large impact on the magnitude of the SAPs, but that the trend remains the same regardless of the average absorption in the downstream section.

7.7 Summary

In this chapter, it was demonstrated that the FE tool COMSOL can be used to evaluate the acoustic performance of the sound package for the complex air cavity geometry case. The sound pressures were calculated and compared for different number of element cases, and for the different area cases. Moreover, the contribution of the sound geometry shape change was studied by comparing the transmission loss of two different cases.

Analytically obtained solutions were compared to the finite element solutions attained by using COMSOL software in a more realistic downstream air cavity case. In order to study the contribution of the average absorption in the downstream, two different average absorption cases were then compared. It can be seen that the average absorption in the downstream region has an impact on the magnitude of the SAPs in that region; the higher the average absorption in the downstream section, the lower the SAPs since the sound energy tends to dissipate more rapidly given highly absorptive surfaces.

CHAPTER 8. SAP PREDICTION METHOD

In this chapter, the process used to develop an empirical equation that can be used to estimate the space-averaged pressures for various averaged absorptions in a realistically-shaped downstream section is demonstrated. The significance of this empirical equation is that it can be used to predict the SAP in the complex geometry (or vehicle-like cavity) case by using inputs that resulted from a simple rectangular duct optimization. Then, the application of this equation can be extended to estimate the space-averaged pressure of the vehicle interior with a weight-minimized sound package.

8.1 Correlation Study

To study the acoustic performance of the sound packages that were obtained by running the optimization for the straight duct case when those packages were used as inputs to the vehicle-like cavity case, the FEA model was used to calculate the total energy, space-averaged pressure, and the intensity behind the flexible MPP to establish the correlation between the two cases. The dimensions of the model were presented in Figure 7.2.

Figure 8.1 shows the relation between the SAPs for the rectangular duct and the vehicle-like geometry cases. The average of SAPs resulting from 10 different surface density combinations (the set of 10 lowest surface densities that gave the same SAP in the TMM case) were calculated by using the FE model and are plotted over the downstream SAP range in the TMM case from 0.013 Pa (~56 dB) to 0.028 Pa (~63 dB).

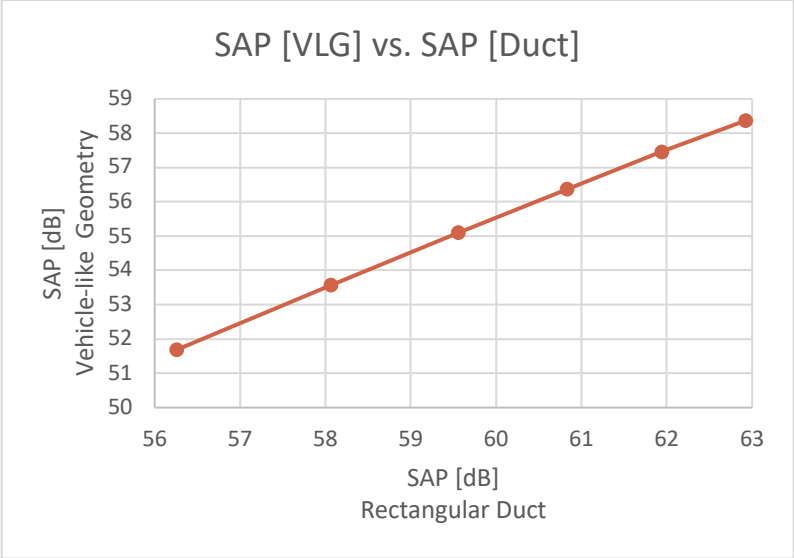

Figure 8.1: *Space-averaged pressures in the duct and vehicle-like geometry (or vehicle-like cavity) when the average interior absorption was 0.3.*

It can be seen that there is a nearly linear relationship between the SAPs calculated for the rectangular duct and the vehicle-like geometry cases. The SAPs for both cases are listed in Table 8.1, where it can be seen that the VLG SAP's are consistently approximately 4.5 dB below the duct results.

Table 8.1: SAP for both the rectangular duct and vehicle-like geometry.

SAP [dB] Duct	56.3	58.1	59.6	60.8	61.9	62.9
SAP [dB] VLG	51.7	53.6	55.1	56.4	57.5	58.4

*VLG: Vehicle-Like Geometry (or VLC: Vehicle-Like Cavity)

As noted, there is a level difference between the two cases, and this level difference needs to be accounted for if the TMM optimization procedure is to be used to identify sound packages that result in specified SAPs in the vehicle-like shape cavity. The level difference comes from the shape and the area differences between the two cases. For this particular case, the area of the duct was 0.015 m^2 and the area of the vehicle-like geometry was 1.6 m^2, so that the area ratio between them was 107.

It was previously observed that the area normalized integrated energy density was identical for two different geometries so long as the boundary condition remained the same between the two

(i.e., straight duct case with the same termination impedance). Here, the case when there was a simple area change in the downstream region was considered. For example, the vehicle-like geometry introduced in Figure 7.2 has an area change within regions *A* and *C*. Thus, the effect of the area change on the sound pressure in the cavity with a change in absorption area was studied.

In Figure 8.2, the two different geometries that were used to calculate the energy density and SAP are shown. Case (a) indicates the straight duct case and case (b) indicates the vehicle-cabin-like geometry case, both with the same $11.25\rho c$ impedance placed opposite to the inlet.

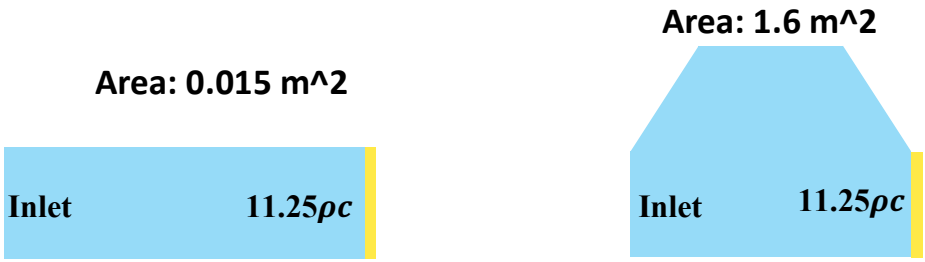

(a) (b)

Figure 8.2: *Two impedance- terminated geometries. (a) straight duct case, (b) vehicle-like-cavity case.*

For the analysis, a plane wave was applied at the inlet, and the same impedance of $11.25\rho c$ was specified at the end of the downstream section in both cases. The energy density in the cavity (Equation (72)), SAP (Equation (73)) were calculated and the results are plotted in Figure 8.3. Since the two geometries had different areas, the calculated values were all normalized with respect to the model's area.

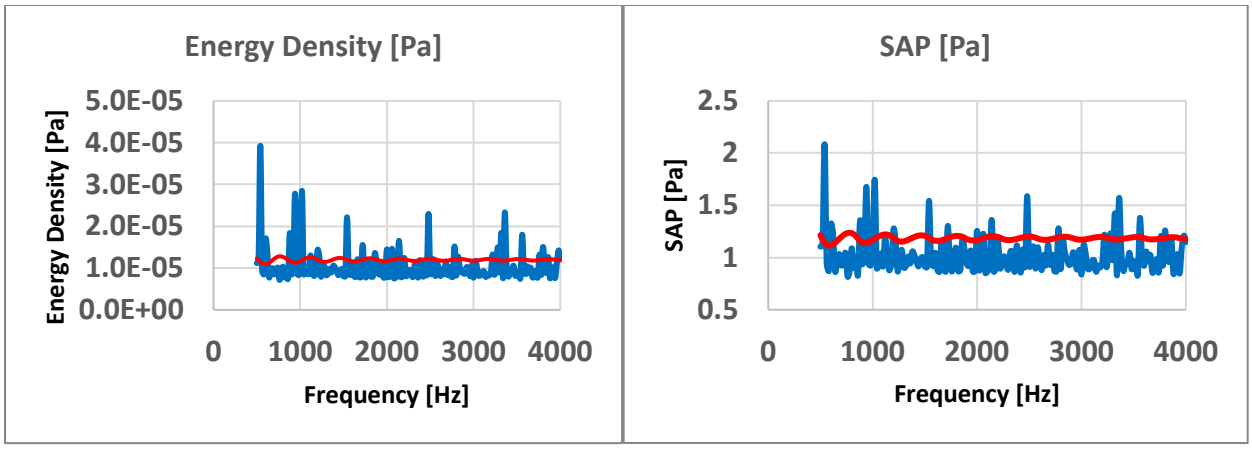

(a) (b)

Figure 8.3: *(a) The energy density, (b) SAP for a straight duct (red solid line) and a vehicle-like-cavity (Blue solid line).*

It can be seen that the trends are an average similar for the energy density in the cavity and the SAP. Therefore, these values will be studied in the next section to develop an equation based on this correlation. The average of the energy density and SAPs in the frequency range between 500 Hz to 4000 Hz are listed in the Table 8.2.

Table 8.2: Energy density, and SAP for different areas.

CASE	Energy Density [Pa]	SAP [Pa]
DUCT	1.19×10^{-5}	1.18
VLC	1.04×10^{-5}	1.02
DUCT/VLC	1.14	1.17

*VLC: Vehicle-Like Cavity (or VLG: Vehicle-Like Geometry)

8.2 Developing the Equation to Predict the SAPs in the Cavity

In the previous section, it was seen that the energy density is correlated to the SAP. Therefore, this correlation will be used to develop a method that predicts the SAPs in the vehicle-like shape cavity by using the outputs from the rectangular duct case. In order to study the correlation among the

acoustical characteristics, the acoustic behaviors of the duct and vehicle-like cavity cases for various absorption conditions were compared. Figure 8.4 shows the ratio between the energy density ratio $[(\widehat{E}_{Duct})/(\widehat{E}_{VLC})]$ and the SAP ratio (SAP_{Duct}/SAP_{VLC}) that were obtained by averaging the results for the previously mentioned 10 different sound packages that resulted from the straight duct optimization for various target SAPs ranging from 0.013 Pa to 0.028 Pa. Here, $\widehat{E}_{Duct}$ and $\widehat{E}_{VLC}$ denote the sound energy density in the air cavity obtained by using Equation (72).

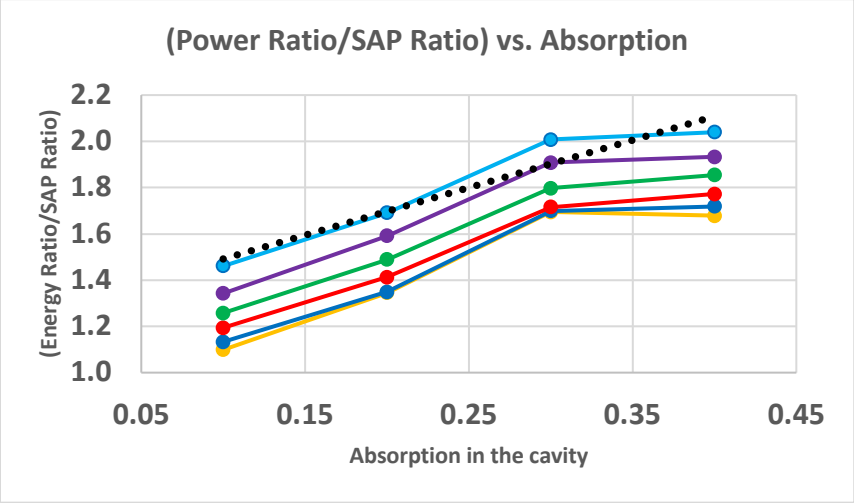

Figure 8.4: *Sound energy density ratio with respect to SAP ratio for various absorption. (Target SAPs [Pa]: Teal → 0.028, Purple → 0.025, Green → 0.022, Red → 0.019, Blue → 0.016, Orange → 0.013).*

It can be seen from Figure 8.4 that the relation between sound energy density ratio and the SAPs ratio for various target SAPs is non-linear. However, to simplify the prediction process, a linear approximation (e.g., the dotted black line in Figure 8.4) was used here. The absorption range considered here is between 0.1 and 0.4. The linear approximations for the various target SAPs are presented in Table 8.3. The coefficients for each target SAP were then averaged to give a single equation describing the relation between the two quantities.

Table 8.3: Linearized equation for various target SAPs.

Target SAP [Pa]	**Linearized Equation [$\mathbf{F_1(\bar{\alpha}_{VLC})}$]**
0.013	$2.0917(\bar{\alpha}_{\mathrm{VLC}}) + 0.9313$
0.016	$2.1070(\bar{\alpha}_{\mathrm{VLC}}) + 0.9480$
0.019	$2.0399(\bar{\alpha}_{\mathrm{VLC}}) + 1.0137$
0.022	$2.0972(\bar{\alpha}_{\mathrm{VLC}}) + 1.0752$
0.025	$2.0903(\bar{\alpha}_{\mathrm{VLC}}) + 1.1712$
0.028	$2.0544(\bar{\alpha}_{\mathrm{VLC}}) + 1.2860$
AVG	$\mathbf{2.0801(\bar{\alpha}_{VLC}) + 1.0709}$

Once the equation that describes the relation between the sound energy density ratio and the SAP ratio is obtained, the following equations that represent the SAPs in the complex geometry case were formulated as,

$$\frac{\bar{E}_{\mathrm{Duct/VLC}}}{SAP_{\mathrm{Duct/VLC}}} = F_1(\bar{\alpha}_{\mathrm{VLC}}) \tag{75}$$

so that it is possible to write

$$SAP_{\mathrm{VLC}} = \frac{\bar{E}_{\mathrm{VLG}}\, F_1(\bar{\alpha}_{\mathrm{VLC}})}{\bar{E}_{\,\mathrm{Duct}}} SAP_{\mathrm{Duct}}. \tag{76}$$

Note that, the sound energy density relates to the sound power by a factor of $2/c$ (i.e., $\bar{E}_{\mathrm{Duct}} = (2\bar{P}_{\mathrm{Duct}})/(cA_{\mathrm{cavity,Duct}})$) where c is the speed of sound. Thus, $(\bar{E}_{\mathrm{VLC}}/\bar{E}_{\mathrm{Duct}})$ can be replaced with $(\bar{P}_{\mathrm{VLC}}/A_{\mathrm{cavity,VLC}})$ $/(\bar{P}_{\mathrm{Duct}}/A_{\mathrm{cavity,Duct}})$, where $\bar{P}_{\mathrm{VLC}}$ and $\bar{P}_{\mathrm{Duct}}$ denotes the sound power in the vehicle-like cavity and the rectangular duct, respectively. Also, $\mathrm{A}_{\mathrm{cavity,Duct}}$ and $\mathrm{A}_{\mathrm{cavity,VLC}}$ denote the areas of the air cavity for the rectangular duct and the vehicle-like cavity, respectively. To compare the sound power in the air cavity in the complex case to that of the power incident on the sound package, the relation between $\bar{P}_{\mathrm{VLC}}$ and $\bar{P}_{\mathrm{in,VLC}}$ is plotted in Figure 8.5 for the various averaged absorptions in the cavity. Here, $\bar{P}_{\mathrm{in,VLC}}$ denotes the power incident on the cavity that is obtained by using Equation (53), but, here, the line integral was performed at the boundary between the flexible MPP and the air cavity. The values used to find the relation are listed in Table 8.7. The equation that describes this relation for various absorptions is listed in Table 8.4. Again, the coefficient for the individual cases were averaged to give the values in the bottom row of Table 8.4.

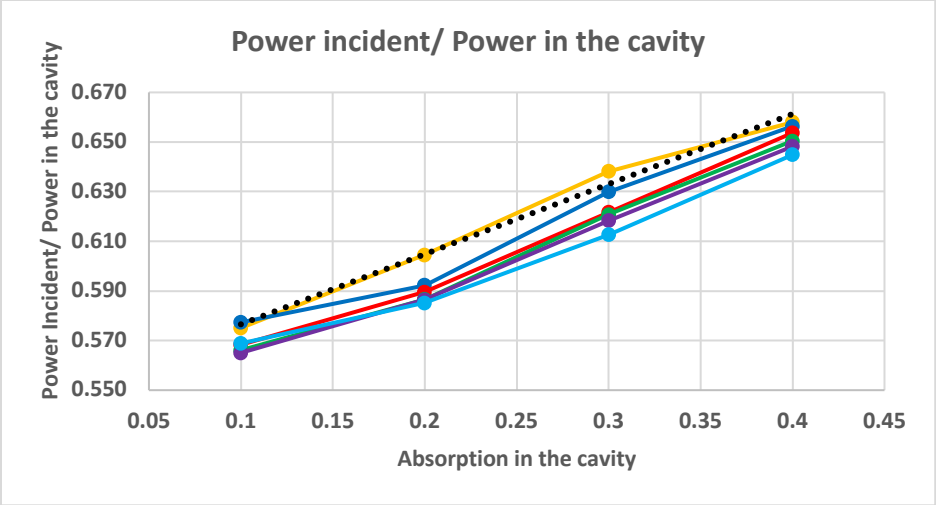

Figure 8.5: *Power incidence (VLC) and the total sound power (VLC). (Target SAPs [Pa]: Teal → 0.028, Purple → 0.025, Green → 0.022, Red → 0.019, Blue → 0.016, Orange → 0.013).*

Table 8.4: Linearized equations for various target SAPs.

Target SAP [Pa]	**Linearized Equation [$F_2(\bar{\alpha}_{\mathrm{VLC}})$] [1/m]**
0.013	$0.2825(\bar{\alpha}_{\mathrm{VLC}}) + 0.5483$
0.016	$0.2749(\bar{\alpha}_{\mathrm{VLC}}) + 0.5452$
0.019	$0.2883(\bar{\alpha}_{\mathrm{VLC}}) + 0.5362$
0.022	$0.2872(\bar{\alpha}_{\mathrm{VLC}}) + 0.5342$
0.025	$0.2813(\bar{\alpha}_{\mathrm{VLC}}) + 0.5342$
0.028	$0.2554(\bar{\alpha}_{\mathrm{VLC}}) + 0.5390$
AVG	$\mathbf{0.2783(\bar{\alpha}_{\mathrm{VLC}}) + 0.5395}$

The equation that relates $\bar{P}_{\mathrm{VLC}}$ to $\bar{P}_{\mathrm{in,VLC}}$ is then

$$\bar{P}_{\mathrm{VLC}} = \bar{P}_{\mathrm{in,VLC}} / F_2(\bar{\alpha}_{\mathrm{VLC}}) \tag{77}$$

and then Equation (77) is substituted into Equation (76) to relate $\bar{P}_{\mathrm{in,VLC}}$ to SAP_{VLC} as: i.e.,

$$SAP_{\mathrm{VLC}} = \frac{\bar{P}_{\mathrm{in,VLC}} A_{\mathrm{cavity,Duct}} F_1(\bar{\alpha}_{\mathrm{VLC}})}{\bar{P}_{\mathrm{Duct}} A_{\mathrm{cavity,VLC}} F_2(\bar{\alpha}_{\mathrm{VLC}})} SAP_{\mathrm{Duct}}. \tag{78}$$

The only unknown remaining in Equation (78) is the power incidence, $\bar{P}_{\mathrm{in,VLC}}$, and this power incidence can be related to the power incident in the rectangular duct case. The relation between $\bar{P}_{\mathrm{in,VLC}}$ and $\bar{P}_{\mathrm{in,Duct}}$ is plotted in Figure 8.6: the values used to fit the relations are listed in Table 8.8, and the coefficient were again averaged to give a single result.

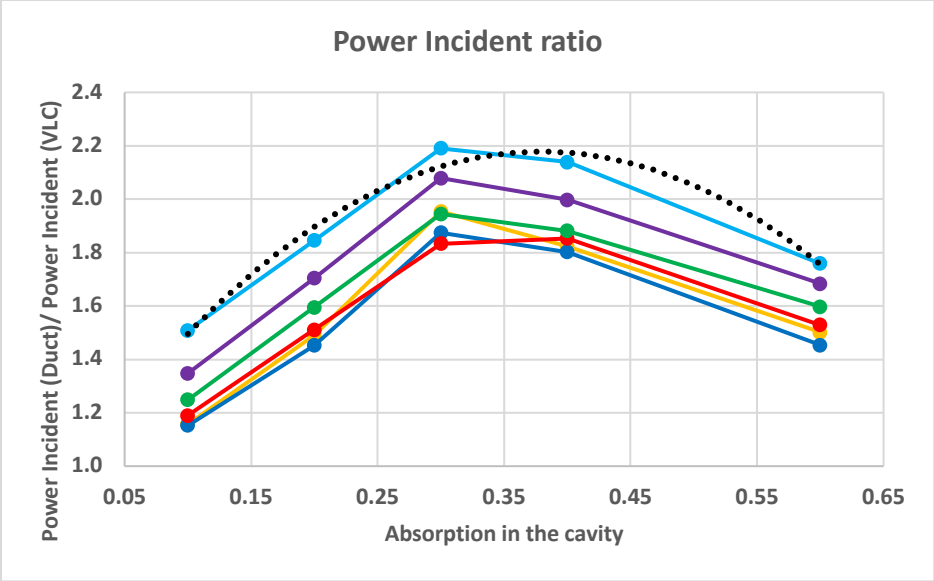

Figure 8.6: *Power incidence/ inlet area ratio (VLC) and the total sound power/cavity area (VLC). (Target SAPs [Pa]: Teal → 0.028, Purple → 0.025, Green → 0.022, Red → 0.019, Blue → 0.016, Orange → 0.013)*

From the results shown in Figure 8.6, it was decided that the equation that relates $\bar{P}_{\mathrm{in,VLC}}$ and $\bar{P}_{\mathrm{in,Duct}}$ could be expressed as,

$$\bar{P}_{\mathrm{in,VLC}} = \frac{\bar{P}_{\mathrm{in,Duct}} A_{\mathrm{in,VLC}}}{A_{\mathrm{in,Duct}} F_3(\bar{\alpha}_{\mathrm{VLC}})}. \tag{79}$$

That is, in this case, a polynomial (black dotted line) seemed to be the most suitable choice to represent the relation between the power inputs for the vehicle-like cavity and duct cases: the corresponding equations are listed in Table 8.5.

Table 8.5: Polynomial equations for various target SAPs.

Target SAP [Pa]	**Polynomial Equation [$\mathbf{F_3(\bar{\alpha}_{VLC})}$]**
0.013	$-8.6922(\bar{\alpha}_{VLC})^2 + 6.7342(\bar{\alpha}_{VLC}) + 0.5393$
0.016	$-9.0944(\bar{\alpha}_{VLC})^2 + 7.0745(\bar{\alpha}_{VLC}) + 0.5220$
0.019	$-7.9139(\bar{\alpha}_{VLC})^2 + 6.2567(\bar{\alpha}_{VLC}) + 0.6259$
0.022	$-8.0582(\bar{\alpha}_{VLC})^2 + 6.3344(\bar{\alpha}_{VLC}) + 0.6899$
0.025	$-8.5810(\bar{\alpha}_{VLC})^2 + 6.6757(\bar{\alpha}_{VLC}) + 0.7589$
0.028	$-8.7053(\bar{\alpha}_{VLC})^2 + 6.6142(\bar{\alpha}_{VLC}) + 0.9210$
AVG	$\mathbf{-8.5075(\bar{\alpha}_{VLC})^2 + 6.6150(\bar{\alpha}_{VLC}) + 0.6762}$

Finally, Equation (79) was substituted into Equation (78) to yield the equation that predicts the space-averaged pressure in the vehicle-like cavity: i.e.,

$$SAP_{\mathrm{VLC}} = \frac{\bar{P}_{\mathrm{in,Duct}} A_{\mathrm{in,VLC}} A_{\mathrm{cavity,Duct}} F_1(\bar{\alpha}_{\mathrm{VLC}})}{\bar{P}_{\mathrm{Duct}} A_{\mathrm{cavity,VLC}} A_{\mathrm{in,Duct}} F_2(\bar{\alpha}_{\mathrm{VLC}}) F_3(\bar{\alpha}_{\mathrm{VLC}})} SAP_{\mathrm{Duct}} \tag{80}$$

Table 8.6: Ratios between sound power ratio (Duct/VLC) and SAP ratios (Duct/VLC).

	Target SAP [Pa] – TMM					
	0.013 Pa	**0.016 Pa**	**0.019 Pa**	**0.022 Pa**	**0.025 Pa**	**0.028 Pa**
Absorption	Power Ratio /SAP Ratio	Power Ratio /SAP Ratio	Power Ratio /SAP Ratio	Power Ratio /SAP Ratio	Power Ratio /SAP Ratio	Power Ratio /SAP Ratio
0.1	1.099	1.133	1.194	1.258	1.342	1.461
0.2	1.344	1.348	1.412	1.489	1.591	1.690
0.3	1.695	1.699	1.716	1.797	1.908	2.008
0.4	1.679	1.718	1.773	1.854	1.933	2.039

Table 8.7: Sound power incidence/ inlet area ratio (VLC) and total sound power/ cavity area (VLC).

	Target SAP [Pa] – TMM					
	0.013 Pa	**0.016 Pa**	**0.019 Pa**	**0.022 Pa**	**0.025 Pa**	**0.028 Pa**
Absorption	Power In/ Power	Power In/ Power	Power In/ Power	Power In/ Power	Power In/ Power	Power In/ Power
0.1	0.575	0.577	0.568	0.566	0.565	0.569
0.2	0.604	0.592	0.590	0.587	0.586	0.585
0.3	0.638	0.630	0.622	0.621	0.618	0.613
0.4	0.658	0.656	0.654	0.650	0.648	0.645

Table 8.8: Sound power incidence/ inlet area ratio (DUCT) and Power incidence/ inlet area (VLC).

	Target SAP [Pa] – TMM					
	0.013 Pa	**0.016 Pa**	**0.019 Pa**	**0.022 Pa**	**0.025 Pa**	**0.028 Pa**
Absorption	Power In Ratio (DUCT)/ (VLC)	Power In Ratio (DUCT)/ (VLC)	Power In Ratio (DUCT)/ (VLC))	Power In Ratio (DUCT)/ (VLC)	Power In Ratio (DUCT)/ (VLC)	Power In Ratio (DUCT)/ (VLC)
0.1	1.157	1.152	1.190	1.248	1.348	1.509
0.2	1.491	1.453	1.511	1.595	1.704	1.845
0.3	1.954	1.874	1.833	1.945	2.079	2.190
0.4	1.824	1.803	1.853	1.881	1.998	2.139

By using Equation (80), the predicted space-averaged pressures in the vehicle-like cavity case can be compared with the values obtained by using FE analysis, as shown in Figure 8.7.

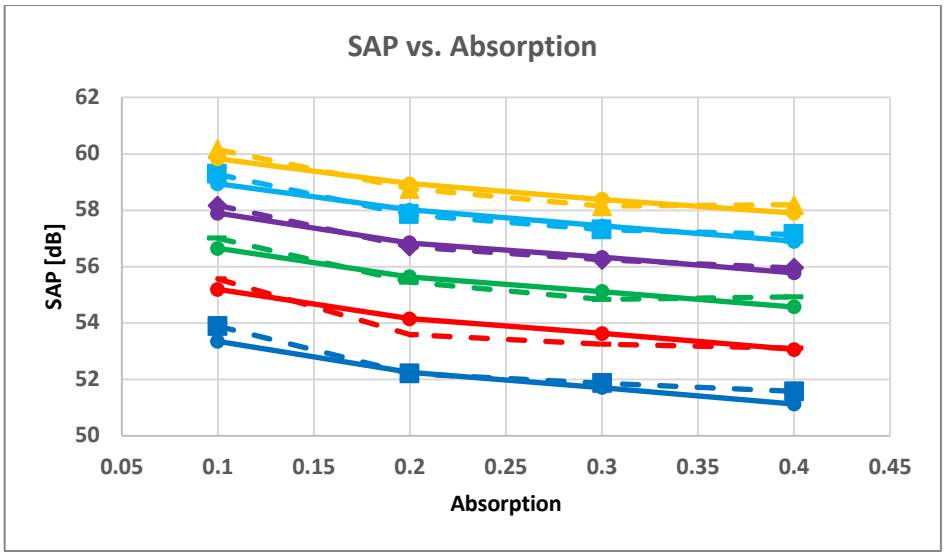

Figure 8.7: *SAPs in the vehicle-like cavity for various target SAPs and absorptions in the cavity. (dashed line: results from prediction, solid line: FEA results), (Target SAPs [Pa], Orange → 0.028, Teal → 0.025, Purple → 0.022, Green → 0.019, Red → 0.016, Blue → 0.013).*

It can be seen from Figure 8.7 that the results obtained by using the empirical result (Equation 80) show good agreement with the FEA calculated results. Thus, the developed equation can be successfully used to estimate the SAPs in the complex geometry case (vehicle-like cavity). However, the drawback of this empirical approach is that the equation is dependent on the SAP target: i.e., F_1, F_2, and F_3 are all different for the target SAPs. Thus, all the coefficients in the correlation functions (F_1, F_2, and F_3) were numerically averaged to give a single correlation function for all the SAP cases. The SAPs that were calculated by using Equation (80) for various averaged absorptions and target SAPs are listed in Table 8.9, and the error between the predicted results and the results obtained by using FEA are listed in Table 8.10. Here, F_1, F_2, and $F_3$are the averaged functions presented in Tables 8.3 to 8.5.

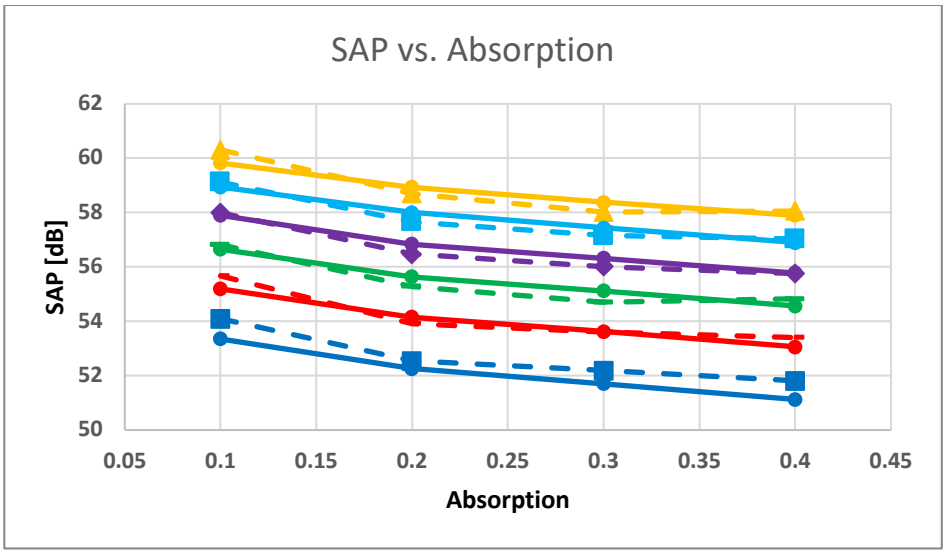

Figure 8.8: *SAPs in the complex geometry (vehicle-like cavity) for various target SAPs and absorptions in the cavity.(dashed line: results from prediction, solid line: FEA results), (Target SAPs [Pa], Orange → 0.028, Teal → 0.025, Purple → 0.022, Green → 0.019, Red → 0.016, Blue → 0.013).*

It can be seen that there are some discrepancies between the FEA results and the predictions, but they are generally small, generally less than 1 dB. This difference results from the averaging of the coefficients in F_1, F_2, and F_3. However, the trends remain the same.

Table 8.9: SAP in Vehicle-Like Cavity (FEA Results vs. Predicted Results)

SAP in Vehicle-Like Cavity (FEA Results)				
Target SAP (Pa)/(dB)	**Absorption in the Cavity**			
	0.1	**0.2**	**0.3**	**0.4**
0.013/56.26	0.009/53.35	0.008/52.26	0.008/51.71	0.007/51.13
0.016/58.06	0.012/55.19	0.010/54.15	0.010/53.62	0.009/53.06
0.019/59.55	0.014/56.65	0.012/55.64	0.011/55.12	0.011/54.57
0.022/60.83	0.016/57.90	0.014/56.84	0.013/56.32	0.012/55.78
0.025/61.94	0.018/58.94	0.016/58.01	0.015/57.44	0.014/56.90
0.028/62.92	0.020/59.82	0.018/58.94	0.017/58.38	0.016/57.90
0.013/56.26	0.010/54.10	0.008/52.54	0.008/52.18	0.008/51.81
0.016/58.06	0.012/55.67	0.010/53.92	0.010/53.60	0.009/53.40
0.019/59.55	0.014/56.82	0.012/55.28	0.011/54.70	0.011/54.82
0.022/60.83	0.016/57.99	0.013/56.48	0.013/56.01	0.012/55.76
0.025/61.94	0.018/59.12	0.015/57.66	0.014/57.15	0.014/57.03
0.028/62.92	0.021/60.31	0.017/58.70	0.016/58.02	0.016/58.06

Table 8.10: Error % (FEA Results vs. Predicted Results)

SAP in Vehicle-Like Cavity (FEA Results)				
Target SAP (dB)	**Absorption in the Cavity**			
	0.1	**0.2**	**0.3**	**0.4**
56.26	1.40	0.54	0.92	1.34
58.06	0.87	0.44	0.04	0.64
59.55	0.30	0.63	0.75	0.46
60.83	0.16	0.64	0.56	0.04
61.94	0.31	0.59	0.51	0.23
62.92	0.81	0.41	0.62	0.29

Note, finally, that Equation (80) can predict the space-averaged pressure in the complex geometry (vehicle-like cavity) case with a maximum error of 1.4 percent. Thus, it can be concluded that the equation that was developed to predict the space-averaged pressures by using the SAP results obtained from the TMM-based optimization is reasonably accurate.

Once the SAP prediction equation for certain averaged absorptions in the downstream section has been developed, then it is possible to create an acoustic map that can be used to estimate the SAP in the complex geometry case, as shown in Figure 8.9. In order to generate the acoustic map, the relation between the $\bar{P}_{\mathrm{in,Duct}}$ and $\bar{P}_{\mathrm{Duct}}$ was obtained for various absorptions and target SAPs: i.e., the ratio of $\bar{P}_{\mathrm{in,Duct}}/\bar{P}_{\mathrm{Duct}}$ was curve-fitted for various conditions (termination absorptions and the target SAPs). Once the equation that can describe the behavior of the $\bar{P}_{\mathrm{in,Duct}}/\bar{P}_{\mathrm{Duct}}$ ratio for various conditions was obtained, the ratio was then used in Equation (80) to calculate the SAP_{VLC} for various conditions. In Figure 8.9, the *y*-axis indicates the target SAPs for a rectangular-shaped duct, and the *x*-axis indicates the termination absorptions for a rectangular-shaped duct.

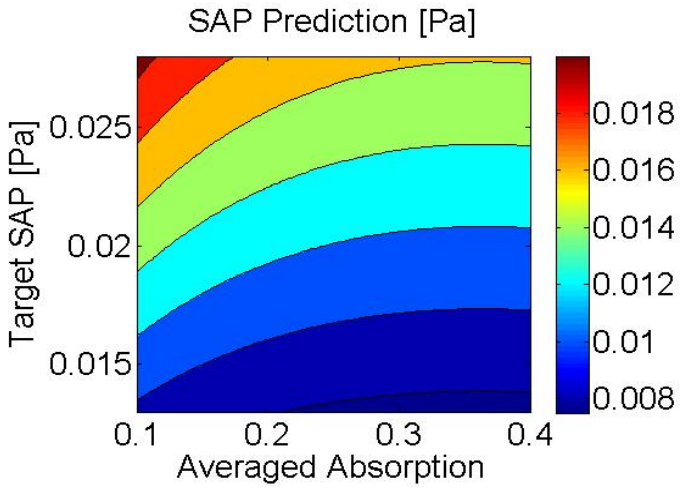

(a)

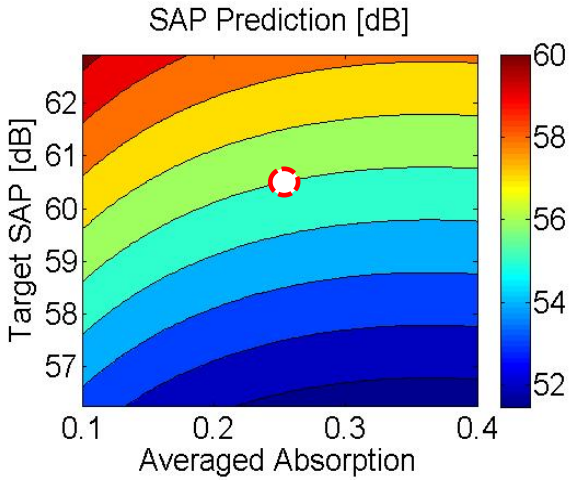

(b)

Figure 8.9: *SAP predictions for the vehicle-like cavity case (a) [Pa], (b) [dB] case.*

It can be seen that the SAP in the complex geometry case can be graphically estimated so long as the target SAP and the absorption in the duct are known. Likewise, by knowing the desired SAP in the complex geometry case, the target SAP and the absorption in the duct case that needs to be used for the optimization to obtain that specific SAP in the complex geometry case can be identified. For example, the dotted red circle indicates that a SAP of about 56 dB in the complex geometry case, with an averaged absorption of 0.25 in the downstream region, can be achieved by using the minimized sound package that was obtained from setting a target SAP of 60 dB with averaged absorption of 0.25 in the straight duct case.

8.3 Generalization

The equation that was developed here was only validated for the particular geometrical shape that was introduced in Figure 7.2. Therefore in order to generalize that equation for different sets of boundary conditions, that is, for various averaged absorption arrangements and geometries in the downstream section, the characteristics of the correlation functions (F_1, F_2, and F_3) for various boundary conditions must be studied.

8.3.1 Averaged Absorption

There are many different ways to create an averaged absorption of 0.3 in the downstream section. Figure 8.10 shows two different surface impedance arrangements that give the same averaged absorption, 0.3, in the downstream section.

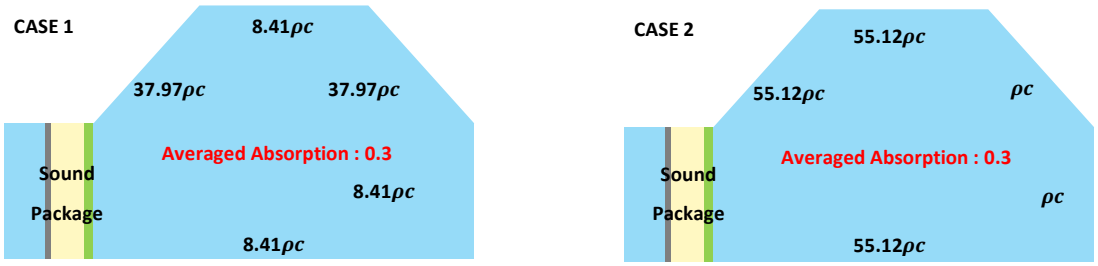

Figure 8.10: *Same averaged absorption for two different surface impedance combinations.*

In order to see the effect of the surface impedance arrangement on the SAP prediction, correlation functions for both cases are plotted and compared in the Figure 8.11. Note that the correlation functions plotted here are different from the correlation functions described previously, i.e., F_1, F_2, and F_3, since they were functions of the averaged absorption in the downstream region; here, the correlation is based on a single averaged absorption of 0.3 in the downstream region.

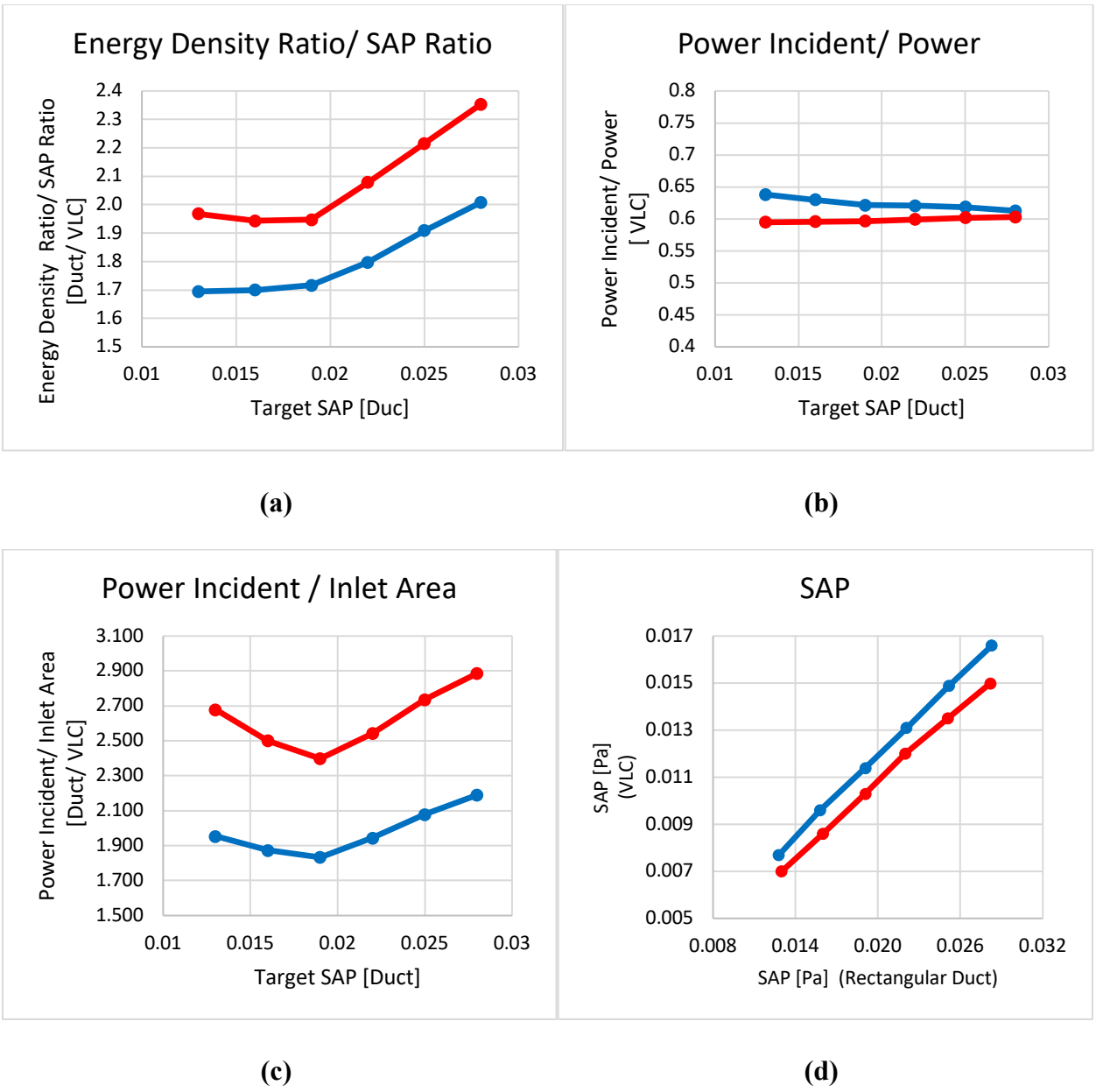

Figure 8.11*: Ratios of (a) Energy density and SAP, (b)Power Incident and power in the cavity, (c) Power Incident and inlet area and (d) SAP for two different surface impedance combinations. (Blue: Case 1, Red: Case 2)*

It can be seen that the values for the two cases are different for each of the target SAPs in the duct, but that they both follow the same trend. Thus, it can be concluded that Equation (80) can be extended to other boundary conditions by appropriately adjusting the coefficients of the correlation functions.

8.3.2 Geometry Shapes

In order to see that the equation can be applicable to other geometry cases as well, different downstream shapes were considered. Figure 8.12 shows two different geometrical shapes that have the same averaged absorptions and areas.

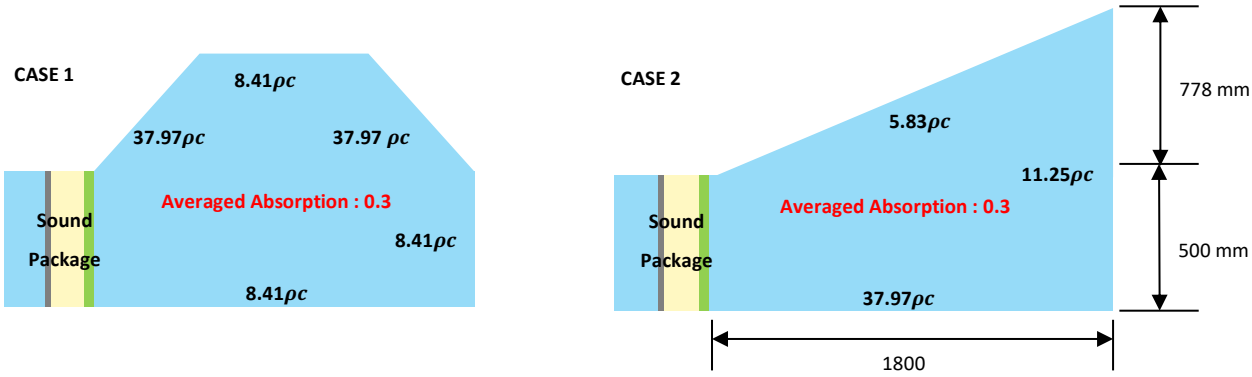

Figure 8.12: *Same averaged absorption for two different surface impedance combinations.*

To analyze the effect of the geometrical shape in the downstream section on the SAP prediction in the complex chamber, the correlation functions for both cases are plotted and compared in Figure 8.13.

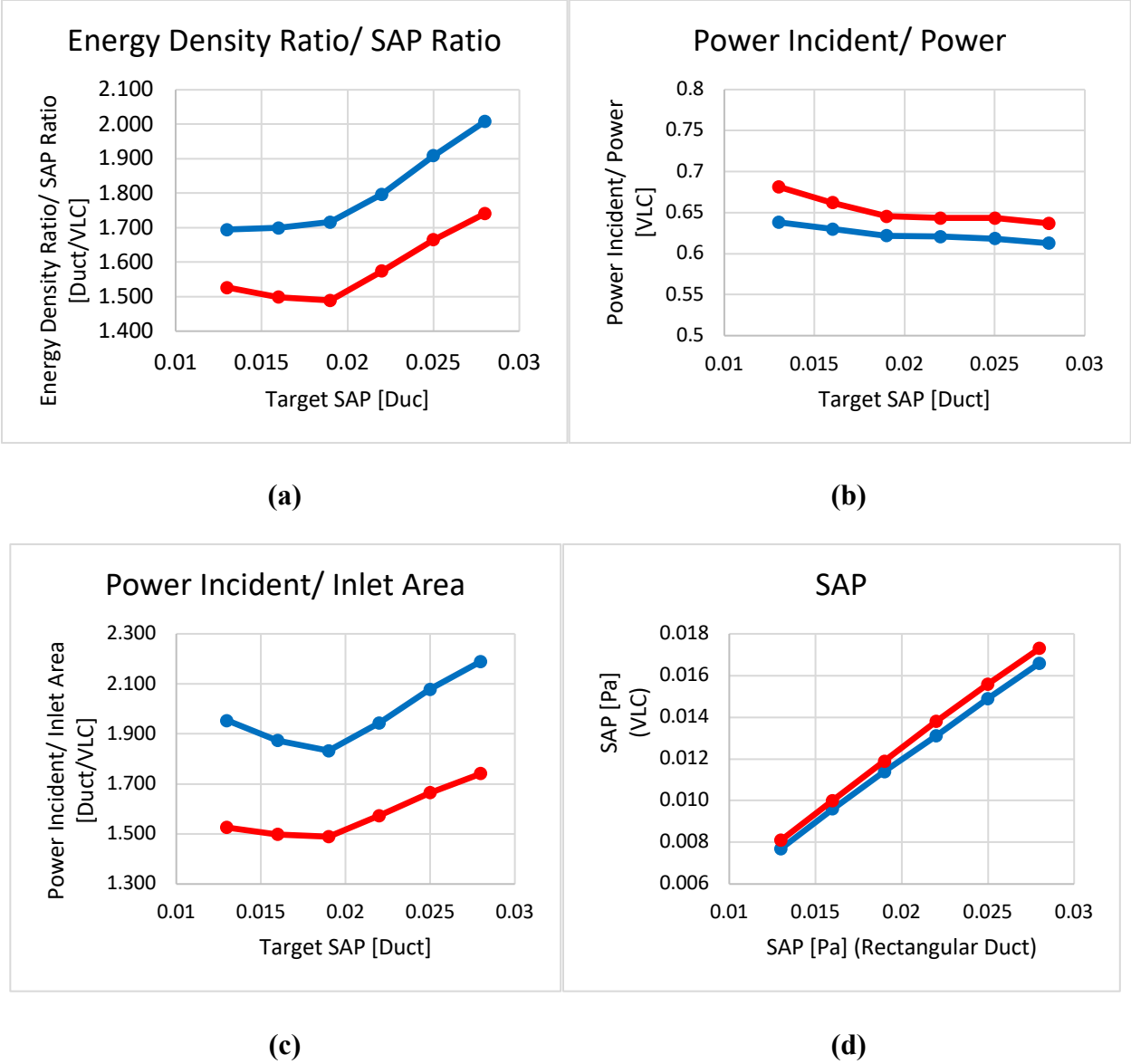

Figure 8.13: *Ratios of (a) Energy density and SAP, (b)Power incident and power in the cavity, (c) Power incident and inlet area and (d) SAP for two different surface impedance combinations. (Blue: Case 1, Red: Case 2).*

For different geometrical shapes in the downstream region, the correlation functions tend to show the same behavior. Therefore, SAP predictions in the complex geometry case can be achieved by using the Equation (80) with adjusted correlation functions.

8.4 Vehicle-Like Cavity + Car Seats + Parcel Shelf (Driver's Right Ear Surface)

Here, a vehicle-like cavity with some additional interior features is considered when predicting the acoustic performance of the sound package by using the results of the straight duct case. Here, not all the vehicle interior features are modeled but a few selected ones such as the car seats (front and rear), carpets (front and rear), and parcel shelf are modeled, since their contribution to the overall acoustic performance in the vehicle cavity is the most significant. The vehicle interior cavity was designed as a two-dimensional surface, and Figure 8.14 represents the driver right ear (i.e., inner) side of the virtual surface in the vehicle cavity.

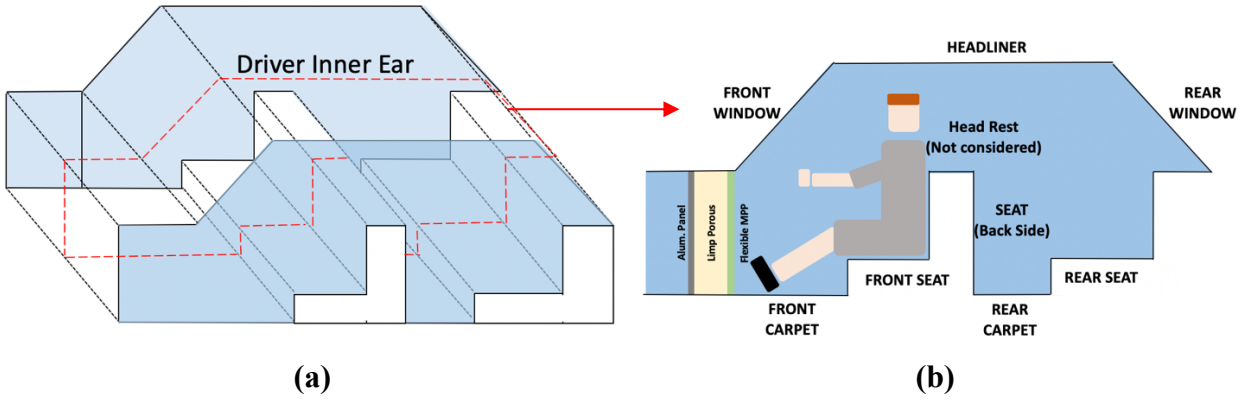

Figure 8.14: *(a) 3D Vehicle interior cavity (b) 2D vehicle cavity representation.*

The cavity dimensions are shown in Figure 8.15. The dimensions were approximations based on various passenger cars. Here, headrests for the front and rear seats were not considered.

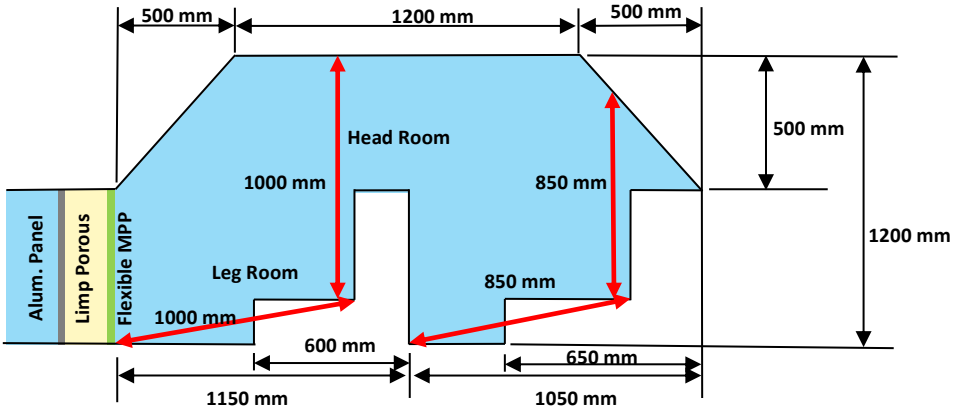

Figure 8.15: *Interior Cavity Dimensions.*

The averaged absorption in the downstream cavity was again set to be 0.3. To create an averaged absorption of 0.3, the surface impedances for each surface segment were arranged as shown in Figure 8.16.

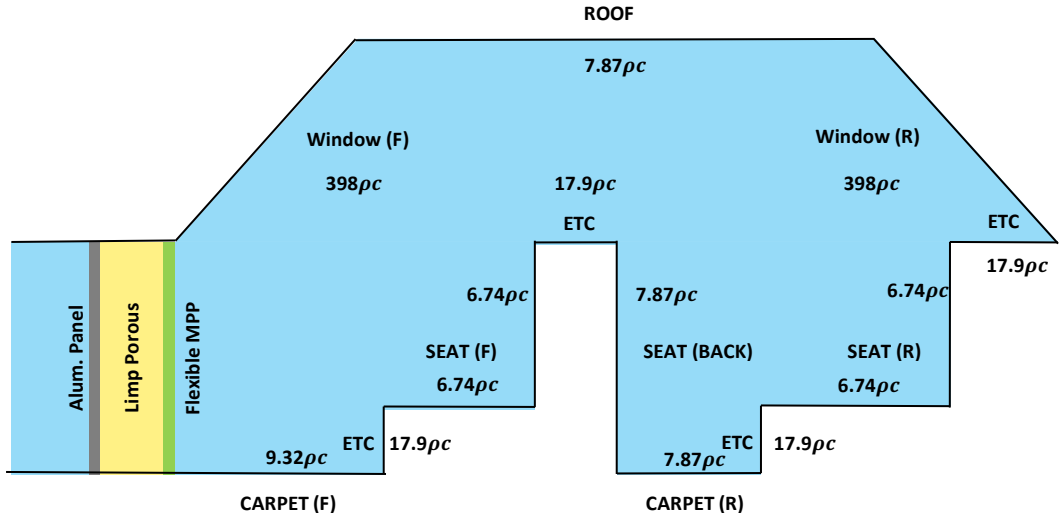

Figure 8.16: *Interior Surface Impedance of the cavity.*

Table 8.11: Surface impedance of each surface in the cavity

	Area [m^2]	Absorption	Impedance	Averaged Absorption
Front Window	0.707	0.01	398 ρc	0.30
Rear Window	0.707	0.01	398 ρc	
Roof	1.2	0.4	7.87 ρc	
Front Seat (Hip)	0.4	0.45	6.74 ρc	
Front Seat (Face)	0.5	0.45	6.74 ρc	
Front Seat (Back)	0.7	0.4	7.87 ρc	
Rear Seat (Hip)	0.4	0.45	6.74 ρc	
Rear Seat (Face)	0.5	0.45	6.74 ρc	
Front Carpet	0.55	0.35	9.32 ρc	
Rear Carpet	0.4	0.35	7.87 ρc	
ETC	0.8	0.2	17.9 ρc	
Total	6.864			

The correlation functions for the original complex geometry and the new complex geometry with several additional features are plotted in Figure 8.17. The functions were compared to demonstrate

the similarity between the two cases and in order to demonstrate that the SAP prediction method can also be used for a more realistic cavity models.

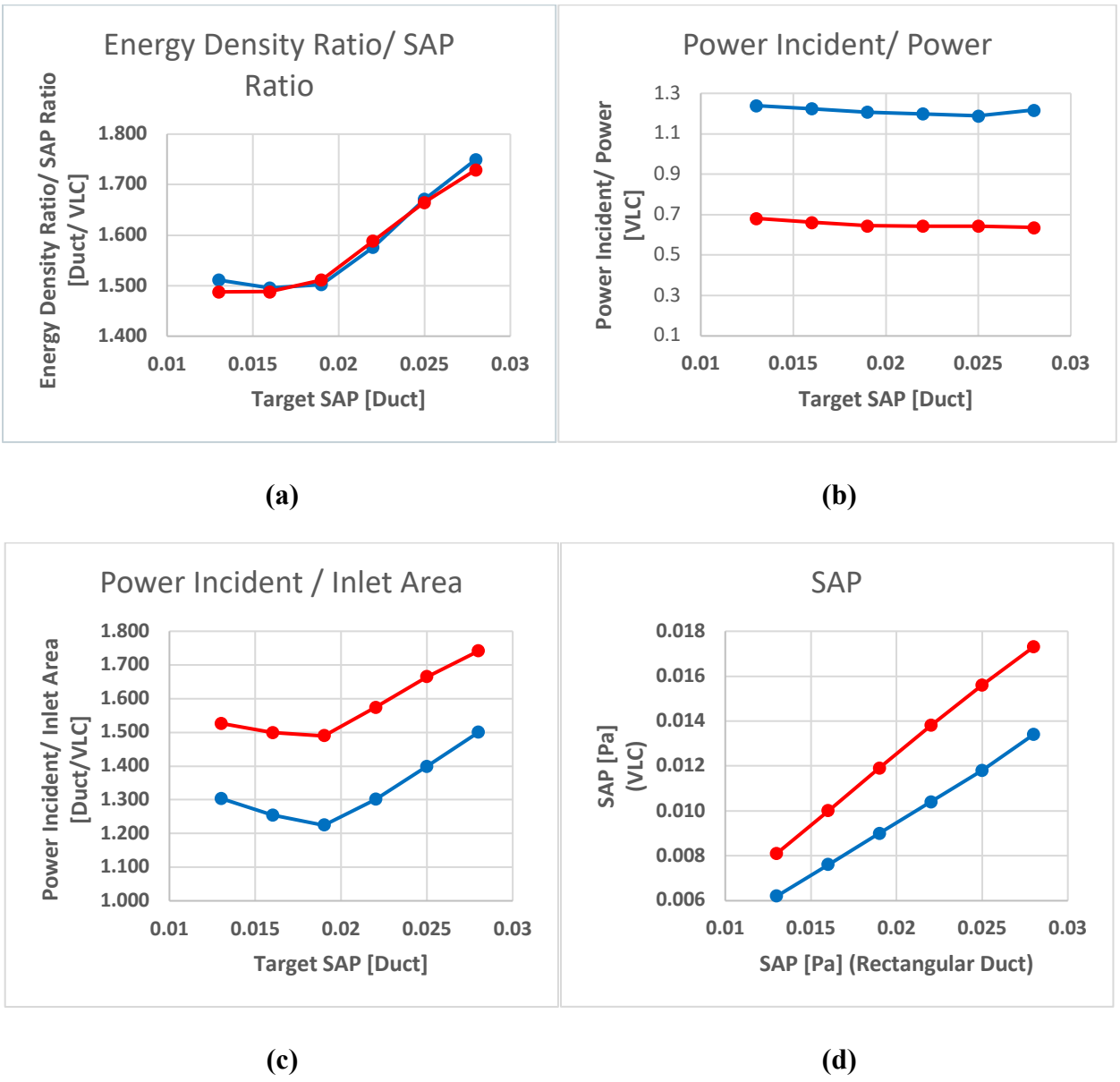

Figure 8.17: *Ratios of (a) Energy density and SAP, (b) Power incident and power in the cavity, (c) Power incident and inlet arear (d) SAP.(Red: Complex Geometry, Blue: Complex geometry w/ car seats + parcel shelf)).*

Based on the results shown in Figure 8.17, the trends of the correlation functions appear to be similar for the two cases. Thus, once the correlation functions for several different boundary conditions in the downstream region are found, the SAP prediction map (Figure 8.9) can be

developed for that particular case. The use of the SAP prediction map can significantly reduce the calculation time required to predict the SAP in a complex geometry case. In conclusion, by comparing the various correlations between the two cases it can be seen that the SAP in the complex geometry case with extra features can be predicted by using the same process as described earlier in the section.

8.5 SAP Near Driver's Right Ear

Automobile manufacturers often use the area near the driver's (or passengers) right (i.e., inner) or left (i.e., outer) ear locations to evaluate the acoustical performance in the vehicle. To address this point, SAPs in the domain near the driver's right ear were calculated and compared to that of total vehicle area to study the acoustical performance of the weight optimized sound packages. In Figure 8.18, The red box indicates the vicinity of the driver's inner, or right ear, and in Figure 8.19, the SAP difference between the total cavity area and the driver's inner ear area is plotted.

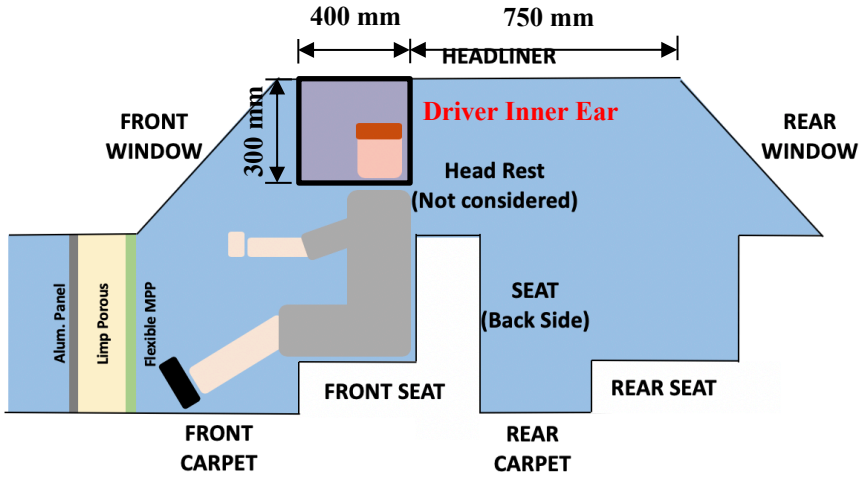

Figure 8.18: *Interior Surface and Driver Inner Ear Side Domain.*

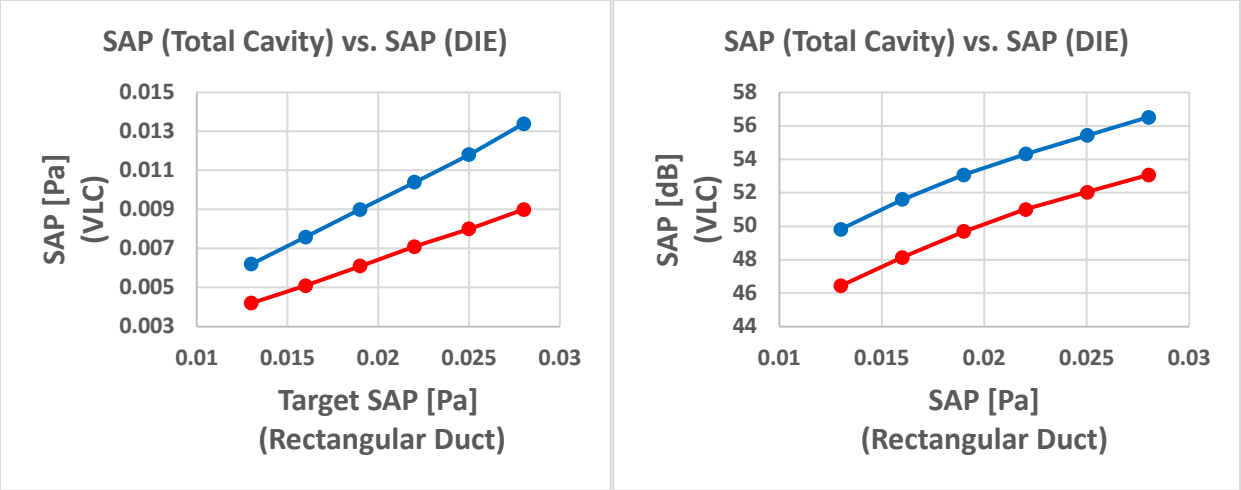

Figure 8.19: *Interior Surface and Driver Inner Ear Domain (a) SAP [Pa], (b) SAP [dB] (Blue Line: Total Cavity, Red Line: Driver's Right Ear Region)*

It can be seen that there is an almost constant level difference in decibel between the two cases (Figure 8.19 (b)). The SAP of the driver's right ear region is about 3.5 dB lower than the SAP of the entire cavity because the acoustic performance of the headliner contributes significantly to the SAP in this region. It can be concluded that the SAP of the driver's ear region follows the same trend as the SAP of the total cavity and is simply offset by a nearly constant amount. Thus, the SAP of the total cavity of the vehicle interior can still be used as a metric to evaluate the acoustic performance of the sound packages, but with an adjustment to account for the spatial variation within the interior space.

8.6 Step-by-Step Guide to Developing the Empirical Equation

In this Section, the steps required to develop an empirical for different interior geometries equation is demonstrated. The process begins with a modeling of the sound package by using the appropriate equivalent fluid model (JCA), based on the stiffness of the material: i.e., whether it is limp or rigid. This sound package model is then expressed as a transfer matrix that is used in the straight duct-shape acoustic model with a termination impedance that matches the average interior absorption of the complex geometry of interest. The Transfer Matrix method is then used to calculate the pressures in the downstream region, which makes possible the space-averaged pressure calculation. Once these preliminary steps are completed, the GA optimizer is used to vary the material properties of the sound packages: i.e., the flow resistances and surface densities of both the porous

layer and the microperforated panel. To start the optimization, select the space-averaged pressure target that is to be achieved in the downstream region, then run the optimization as many times as needed until the expected sound package having specific material properties is obtained. Those material properties are then used to construct the transfer matrix of the sound package which is used to calculate the sound energy density, SAP, and incident power for the rectangular-shaped duct case.

Next, these material properties obtained from the optimization are used as inputs to the equivalent fluid model in the finite element analysis tool. In this particular research, COMSOL was used since this tool has a JCA model as one of the porous media options. The complex geometry used to calculate the various acoustic properties is modeled as a two-dimensional air cavity and the surface impedances are given to make the average absorption the same as in the rectangular duct case. Once the boundary conditions are given appropriately, the energy density, SAP, and power incident for the complex geometry were calculated based on the plane wave radiation as an input to the system.

Once the acoustic properties such as the sound energy density, SAP, and power incident for both the rectangular-shape duct and complex geometry cases are obtained, the correlation between the two cases is established by following the process explained in Section 8.2. Those correlations are then used to link the SAP of the rectangular duct to the complex geometry. Here, the inputs needed to predict the SAP in the complex geometry are the power incident, sound power, SAP for the rectangular-shape duct and geometrical dimensions for both the rectangular-shape duct and the complex geometry.

Finally, the process is repeated for various averaged absorptions and target space-averaged pressures to obtain the points that are interpolated to generate the acoustic map. Once this acoustic map is determined, the SAP estimation for the corresponding setups is obtainable graphically.

8.7 Summary

In this chapter, an equation that predicts the SAPs in the complex geometry case, based on inputs consisting of the results of the optimization in the straight duct case, was developed. Note that the equation showed a good agreement with the FEA data. Furthermore, to generalize the applications of the equation, two different case studies were performed. Based on these results, it can be

concluded that the equation can be used for various surface impedance arrangements and geometrical shapes.

CHAPTER 9.CONCLUSIONS

9.1 Conclusions

The purpose of this research was to develop a process which can be used to identify the minimum weight sound package that meets a certain target sound pressure level in a vehicle interior. In order to develop that process, an optimizer was used to find various sound package material property combinations, and the results from that optimization were used as inputs to an empirical equation that then gives the space-averaged pressure in a different cavity having a certain averaged absorption and shape.

For the weight optimization process, a straight duct air cavity with a certain impedance at the termination was introduced so that the transfer matrix method could be used to calculate the acoustic pressures. The sound package was modeled as an equivalent fluid by using the JCA model for both the limp porous layer and the flexible MPP. The space-averaged pressure was introduced to evaluate the acoustic performance of the sound package.

It was found that the optimization process gave many different flow resistivity and surface density combinations that yielded the same space-averaged pressures. From these optimization results, the possible weight reduction range was identified. It was also concluded, for example, that a combination of a relatively heavy, high flow resistance MPP with a relatively light fibrous layer gave the lowest weight solutions at a given SAP for this particular sound package configuration. The tradeoff between absorption and transmission of the acoustical material was also demonstrated, and it was shown that in the lightest sound packages, barrier performance was favored over absorption performance.

Then, a Finite Element tool was used to evaluate the acoustic performance of the sound packages for a more complex vehicle interior geometry. By using the FE tool, the energy density, SAPs, and incident power were calculated to identify the correlation between the straight duct and the complex geometry cases.

Based on that correlation, an empirical equation was developed that made it possible to estimate the SAPs in the complex geometry case by using the results from the TMM-based optimization in the straight duct case. Moreover, the generality of the equation was validated by considering the impact of different surface impedance arrangements and geometrical shapes. The

empirical equation introduced in this research provides a simple and powerful alternative approach to evaluating the weight-minimized sound packages, obtained by using the GA optimizer, that are intended to be used as a dashpanel for the conventional vehicles. The significance of this approach is that it is time effective, and the steps required to achieve the desired outputs are easy to follow. The only challenge existing in this approach is the need to pre-evaluate the boundary conditions of the vehicle under consideration, since that information is necessary to find the relation between the rectangular duct and the complex geometry cases.

The aspects of this research that differentiating from work done by others is that the GA optimizer was not solely intended to obtain the globally weight-optimized sound package (solution), but rather to find various possible weights of the sound packages (multiple local solutions) that all give same acoustical performance. The intention of this particular strategy is to break the link between the acoustical performance of the sound package and its weight. When sound packages with different weights can serve the same acoustical performance, the function of the sound package can be versatile: i.e., the weight of the sound package can be adjusted to meet a certain weight distribution requirement in the vehicle. Another advantage of this strategy is that it can also possibly reduce the manufacturing cost of the sound package. For instance, manufactures can choose multiple possible solutions among many others based on the cost-specified feasibility: i.e., material properties that are already cost effective to produce.

Now, a few suggestions for future work based on this research. First, for the vehicle-like cavity, the surface impedances were averaged over the frequency considered in order to minimize the complexity of the calculation. However, the analysis needs to be extended to frequency-dependent impedances so that the accuracy of the SAP calculations can be further improved. Secondly, it is suggested that the empirical equation needs to be improved by implementing more exact correlation functions rather than the linearized functions used here to estimate the SAPs in the complex geometry. In this particular research, the averaged coefficients were used for the correlation functions in order simply to demonstrate the procedures. Finally, it would be useful, given adequate computational resources, to extend the current procedure to three dimensions.

REFERENCES

1. X. Olny, R. Panneton, and J. Tran Van, “Experimental Determination of the Acoustical Parameters of Rigid and Limp Materials using Direct Measurements and Analytical Solutions,” *Proc. Forum Acusticum 2002*, Sevilla, Spain (2002).
2. Raymond Panneton, “Comments on the limp frame equivalent fluid model for porous media,” *Journal of the Acoustical Society of America*. 122, EL217 (2007).
3. T.Y. Yoo and J. Stuart Bolton, “The modeling of sound absorption by flexible micro-perforated panels,” *Doctoral Dissertation, Purdue University* (2008).
4. T. Herdtle and J. Stuart Bolton, “Effect of Thermal Losses and Fluid-Structure Interaction on the Transfer Impedance of Microperforated Films,” *Proc. Noise-Con 2014,* Fort Lauderdale, Florida, US (2014).
5. Arnaud Duval, Jean-Francois Rondeau, Guillaume Deshayes and Benoit Teyssandier, “Generalized Light-Weight Concept: A Comprehensive Acoustic Package Weight Reduction Strategy,” *Proc. Automobile Comfort Conference,* Le Mans, France (2006).
6. Arnaud Duval, Jean-Francois Rondeau, Lars Bischoff, Guillaume Deshayes and Ludovic Dejaeger, “Generalized Light-Weight Concept: Improving the Acoustic Performance of Less than 2500g/m^2 insulators,” *SAE Technical Paper,*2136 (2009).
7. Arnaud Duval, Jean-Francois Rondeau, Ludovic Dejaeger, Francis Lhuillier and Julien Monet-Descombey, “Generalized Light-Weight Concepts: A New Insulator 3D Optimization Procedure,” *SAE Technical Paper,* 1947 (2013).
8. A. Parrett, C.Wang, X. Zeng, D. Nieulubowciz, M. Snowden, J.H. Alexander, R.W. Gerdes, B. Leeder and C. Zupan, “Application of Micro-Perforated Composite Acoustic Material to a Vehicle Dash Mat,” *SAE Technical Paper,*1623 (2011).
9. Jun Zhang, Guanni Zhu, Xiaoxuan Zhang, Hogyu Liu, Congguang Liu, “The Vehicle NVH Development and Engineering Application of the Lightweight Sound Package,” V. *Proc. SAE-China Congress: Selected Papers,* pp. 291-300 (2014).
10. Kevin Verdiere, Raymond Panneton, Said Elkoun, Thmas Dupont and Philippe Leclaire, “Transfer matrix method applied to the parallel assembly of sound absorbing materials,” *Journal of the Acoustical Society of America*. 134, pp. 4648-4658 (2013).

11. Nicholas Nakjoo Kim and J. Stuart Bolton, “Optimal design of sound absorbing systems with microperforated panels,” *Doctoral Dissertation, Purdue University* (2016).
12. Xialong Xie and Gaofeng Tang and Yahong Chen and Wei Ye. “Lightweight Design for Fibrous Floor Carpet Based on Acoustic Optimization,” *Proc. Inter-Noise 2017,* Hong Kong, China (2017).
13. Xin Zhe Zhang and Guo Jie Zhang, “Numerical Optimization of Sound Pressure Response for the Dahs Panel Based on Automatically Matched Layer and Genetic Algorithm,” *Journal of Vibroengineering.*19, pp. 3040-3055 (2017).
14. Xian Wu, Xiaokang Tang, Jianwang Shao, “Optimization of acoustic performance of a vehicle dash sound package,” *Proc. Inter-Noise 2016*, Hamburg, Germany (2016)
15. Yuksel Gur, Jian Pan, Wanlu Li, David A. Wagner, “Development of Vehicle Dash and Floor Subsystem Sound Package for Lightweight Vehicle,” *Proc. Noise-Con 2016,* Providence, Rhode Island, US (2016).
16. Noureddine Atalla and Franck Sgard, “Modeling of Perforated Plates and Screens using Rigid Frame Porous Models,” *Journal of Sound and Vibration.* 303, pp.195-208 (2007).
17. Hyunjun Shin and J. Stuart Bolton, “Barrier Mass and Flow Resistance Optimization for Interior Noise Reduction,” *Proc. Noise-Con 2016,* Providence, Rhode Island, US (2016).
18. Yvan Champoux and Jean-F. Allard, “Dynamic Tortuosity and Bulk Modulus in Air-Saturated Porous Media,” *Journal of Applied Physics*. 70(4), pp.1975-1979 (1991).
19. Johnson D. L., Koplik J. and Dashen R., “Theory of dynamic permeability and tortuosity in fluid-saturated porous media,” *Journal of Fluid Mechanics*. 176, pp. 379-402. (1987).
20. J. Stuart Bolton, Oliviero Olivieri, and Taewook Yoo, “Measurement of Normal Incidence Transmission Loss and Other Acoustical Properties of Materials Placed in a Standing Wave Tube,” *Technical Review, Bruel & Kjaer*, No1, pp.12. (2007)
21. Yeon June Kang and J. Stuart Bolton, “Studies of sound absorption by and transmission through layers of elastic noise control foams: Finite element modeling and effects of anisotropy,” *Doctoral Dissertation, Purdue University* (1994).
22. Chadwyck T.Musser, Jerome E. Manning, and George Chaoying Peng,”Predicting Vehicle Interior Sound with Statistical Energy Analysis,” *Sound & Vibration.* 46(12), pp. 8-14 (2012).
23. Jacob Morkholt, Jorgen Hald and Svend Gade, “Sound Intensity Measurements in Vehicle Interiors,” *Journal of the Acoustical Society of America*. 132, pp. 1984-1986 (2012).

24. S.K. Jain, M.P. Joshi, P.G. Shravage, P.S. Yadav and N.V. Karanth, "Evaluation of Acoustic Performance of Automotive Seats by Experimental and Simulation Techniques," *SAE Technical Paper,* 0105 (2013).
25. How the genetic algorithm works. https://www.mathworks.com/help/gads/how-the-genetic-algorithm-works.html.
26. Bruel & Kjaer, "Noise control," 2nd edition, pp. 10. (1986).
27. Hyunjun Shin and J. Stuart Bolton, "Weight minimization of automotive sound packages in the presence of air leaks," *Proc. of Inter-Noise 2018*, Chicago, US (2018).
28. Hyunjun Shin and J. Stuart Bolton, "Weight Minimization of Noise Treatments by Balancing Absorption and Transmission Performance," *Proc. Noise-Con 2017,* Grand Rapids, Michigan, US (2017).
29. Hyunjun Shin and J. Stuart Bolton, "The Identification of Minimum-weight Sound Packages," *Noise Control Engineering Journal*, 66(6), pp. 523-540, (2018).
30. COMSOL Multiphysics, Absorptive muffler, https://www.comsol.com/model/absorptive-muffler-1367.
31. Bryan H. Song and J. Stuart Bolton, "Effect of circumferential edge constraint on the acoustical properties of glass fiber materials," *Journal of the Acoustical Society of America.* 110, pp. 2902-2916 (2001).
32. J. Stuart Bolton, Taewook Yoo, and Jonathan H. Alexander., "The Use of Four-Microphone Standing Wave Tube to Estimate the Anisotropic Properties of Fibrous Noise Control Materials," *Proc. Inter-Noise 2006,* Honolulu, Hawaii, US (2006).
33. Oliviero Olivieri, J. Stuart Bolton, and Taewook Yoo., "Measurement of Transmission Loss of Materials Using Standing Wave Tube," *Proc. Inter-Noise 2006,* Honolulu, Hawaii, US (2006).
34. Jean-Francois Allard, Bruno Brouard, Denis Lafarge, and Walter Lauriks, "Reciprocity and ant reciprocity in sound transmission through layered materials including elastic porous media," *Wave Motion*, vol. 17, pp. 329-335, (1993).
35. Mads Herring Jensen, "Modeling Acoustic Damping Processes," https://www.comsol.com/blogs/modeling-acoustic-damping-processes/ (2013).
36. "Devices For Use In Defining And Measuring Vehicle Seating Accommodation," SAE Standard J826, Revised February 1970 (1970).

37. Bettina Schieche, “Overview of integration methods in space and time,” https://www.comsol.com/blogs/overview-integration-methods-space-time/ (2014).

VITA

Hyunjun Shin was born in the Republic of Korea. He graduated from St. Mary's High School in Medford, Oregon in 2004. He attended Purdue University from 2004 to 2008 and received a Bachelor of Science degree in Mechanical Engineering. He then entered graduate school at Purdue University, in the School of Mechanical Engineering in the fall of 2008. He worked as a Research Assistant with Dr. J. Stuart Bolton from 2008 until he completed his M.S.M.E, at which point he departed from the University to work for LG electronics in Seoul, Korea. He started his Ph.D. program in Mechanical Engineering at Purdue University in 2014 and again worked as a Research Assistant for Dr. J. Stuart Bolton. During his Ph.D. program, he performed two internships at Tesla, Inc., Palo Alto, California, USA. He received his Ph.D. degree from Purdue University in May 2019.